



*Bilim, Teknoloji ve Mühendislik Araştırmaları Dergisi*

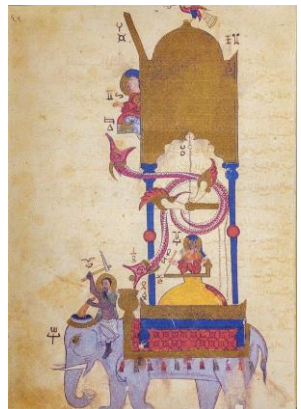
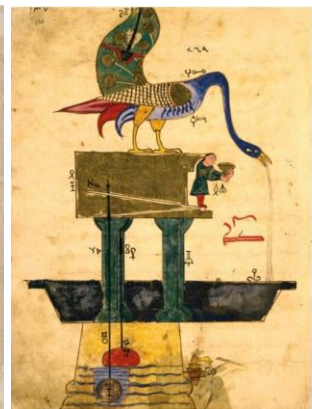
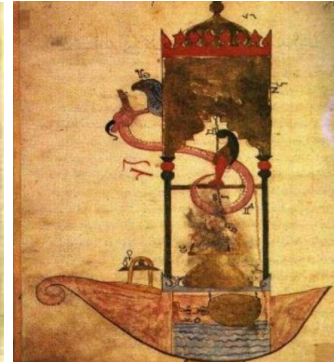
**ISSN: 2717-8404**

**Cilt/Volume: 5 Sayı/Issue: 1-2 Yıl/Year: 2024**

# JOURNAL

**SCIENCE | TECHNOLOGY | ENGINEERING**

**Bilim ⊕ Teknoloji ⊕ Mühendislik**



*Every science that is not converted into practice remains somewhere between right and wrong.*

*El Cezeri*



## CONTENTS / İÇİNDEKİLER

### **Research Article / Araştırma Makalesi**

2. Solution for Integration of Renewable Energy Power Plants into Smart Grids with Active Power Control  
Mehmet Necat Tur Ömer Faruk Ertuğrul Mehmet Rıda Tür , Page: 11-23

3. Investigation of The Effect of Asphalt Layer and Sub-Base Layer Thicknesses on Pavement Surface Deformation by The Finite Element Method  
Mehmet Bayazıt Ferhat Şahinkaya , Page: 24-33

4. Identifying Traveler Groups Lacking in Seatbelt Usage and Suggesting Policy Measures  
Uneb Gazder Ashar Ahmed ,Page: 34-40

5. Enhancing Electrical Distribution System Efficiency: A Software Tool Design for Conductor Cross-Section Optimization With TLBO Algorithm  
Cemil Altın Page: 41-53

6. Impedance Controller Design and Dynamic Solution of The Manipulandum  
Yaşar Yıldırım Babek Naseri Amir Nobahar Reşat Özgür Doruk, Page: 54-67

7. 2D Millimeter-Wave SAR Imaging with Automotive Radar  
Bengisu Yalçınkaya Gökdoğan Remziye Büşra Çoruk Elif Aydın Ali Kara  
Page: 68-77

8. A Supervised Learning Approach With Residual Attention Connections  
Alı Hamza Muhammad Ismail , Page: 78-85

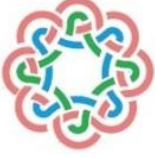
10. Fourier-Based Image Classification Using CNN  
Göktaş Erdem Dağı Erhan Gökçay Hakan Tora, Page: 92-101

### **Review Article / İnceleme Makalesi**

1. Ampute Hastaların Rehabilitasyonunda Kullanılan Yapay Zeka Tabanlı Giyilebilir Robotik Dış İskeletler: Meta Analiz  
Merve Çörekçi Turker Erguzel, Page: 1-10

9. A Complementary Overview and Challenges in Radar Cross Section Modeling of Phased Array Antennas  
Ömer Burak Güngördü Ali Kara Sinan Akşimşek, Page: 86-91





## REVIEW ARTICLE

# Artificial Intelligence Based Wearable Robotic Exoskeletons For Rehabilitation Of Amputee Patients: Meta Analysis

\*<sup>id</sup> Merve Çörekçi, <sup>1</sup><sup>id</sup> Türker Tekin Ergüzel

\*Uskudar University, Institute of Health Sciences, Department of Neuroscience, Istanbul, Türkiye

[merve.corekci@st.uskudar.edu.tr](mailto:merve.corekci@st.uskudar.edu.tr), [Orcid.0000-0002-1098-4651](https://orcid.org/0000-0002-1098-4651).

<sup>1</sup> Uskudar University, Faculty of Engineering, Software Engineering, Istanbul, Türkiye

[turker.erguzel@uskudar.edu.tr](mailto:turker.erguzel@uskudar.edu.tr), [Orcid.0000-0001-8438-6542](https://orcid.org/0000-0001-8438-6542).

**Citation:**

Çörekçi, M. Ergüzel, T. (2024). *Artificial Intelligence Based Wearable Robotic Exoskeletons For Rehabilitation Of Amputee Patients: Meta Analysis*, Journal of Science, Technology and Engineering Research, 4(1): 1-10. DOI: 10.53525/jster.1430072

**HIGHLIGHTS**

- The effect of artificial intelligence technologies used in single-source amputee patient rehabilitation
- Comparison of the most used artificial intelligence technologies in amputee patient rehabilitation
- BCI technology is more preferred in amputee patient rehabilitation
- Researchers can find artificial intelligence technologies used in amputee patients from a single source

**Article Info**

Received : 1 February 2024

Accepted : 3 March 2024

**DOI:**

10.53525/jster.1430072

**\*Corresponding Author:**

Merve Çörekçi

[merve.corekci@st.uskudar.edu.tr](mailto:merve.corekci@st.uskudar.edu.tr)

**ABSTRACT**

Amputation is the loss of all or part of an extremity due to accidents, diabetes, cancer, tumours, osteomyelitis, dysvascular diseases. Amputation affects the motor functions and quality of life of millions of people worldwide. In addition, people with this disability are psychologically affected as well as reduced mobility. This research aims to examine the effect of artificial intelligence-based exoskeletons, which are the source of hope for amputees, on amputee rehabilitation and to compare the artificial intelligence technologies used. For this purpose, the literature was reviewed and a qualitative meta-analysis of the researches of the last 10 years on the effects of artificial intelligence technologies such as brain-computer interface, machine learning, deep learning, artificial neural networks on amputee patient rehabilitation was performed. As a result of the qualitative meta-analysis, it was seen that the most commonly used artificial intelligence technology in amputee patient rehabilitation is the brain-computer interface and all of the artificial intelligence-based exoskeletons used have a positive effect on rehabilitation, and thanks to these artificial intelligence technologies, the mobility limitations of patients with amputation are reduced.

**Keywords:** Amputee rehabilitation, Artificial intelligence, Brain-computer interface, Deep learning, Exoskeletons.



## İNCELEME MAKALESİ

# Ampute Hastaların Rehabilitasyonunda Kullanılan Yapay Zeka Tabanlı Giyilebilir Robotik Dış İskeletler: Meta Analiz

\* Merve Çörekçi, <sup>1</sup> Türker Tekin Ergüzel

\*Üsküdar Üniversitesi, Sağlık Bilimleri Enstitüsü, Nöroloji Bölümü, İstanbul, Türkiye  
[merve.corekci@st.uskudar.edu.tr](mailto:merve.corekci@st.uskudar.edu.tr), [Orcid.0000-0002-1098-4651](https://orcid.org/0000-0002-1098-4651).

<sup>1</sup> Üsküdar Üniversitesi, Mühendislik Fakültesi, Yazılım Mühendisliği Bölümü, İstanbul, Türkiye  
[turker.erguzel@uskudar.edu.tr](mailto:turker.erguzel@uskudar.edu.tr), [Orcid.0000-0001-8438-6542](https://orcid.org/0000-0001-8438-6542).

## Alıntı / Citation :

Çörekçi, M. Ergüzel, T. (2024). *Artificial Intelligence Based Wearable Robotic Exoskeletons For Rehabilitation Of Amputee Patients: Meta Analysis*, Journal of Science Technology and Engineering Research, 4(1): 12-34. DOI: 10.53525/jster.9886xx

## ÖNE ÇIKANLAR / HIGHLIGHTS

- Tek kaynakta ampute hasta rehabilitasyonunda kullanılan yapay zeka teknolojilerinin etkisi
- Ampute hasta rehabilitasyonunda en çok kullanılan yapay zeka teknolojilerinin karşılaştırılması
- Ampute hasta rehabilitasyonunda BCI teknolojisinin daha çok tercih edilmesi
- Araştırmacılar tek kaynakta ampute hastalarda kullanılan yapay zeka teknolojilerini bulabilmeleri

## Makale Bilgileri / Article Info

Geliş Tarihi : 1 Şubat 2024

Kabul Tarihi: 3 Mart 2024

DOI: 10.53525/jster.1430072

\* Sorumlu Yazar:

Merve Çörekçi  
[merve.corekci@st.uskudar.edu.tr](mailto:merve.corekci@st.uskudar.edu.tr)

## ÖZET / ABSTRACT

Amputasyon; kazalar, diyabet, kanser, tümör, osteomyelit, disvasküler hastalıklar gibi nedenlerden dolayı herhangi bir ekstremitenin tamamının ya da bir kısmının yokluğudur. Amputasyon dünya çapında milyonlarca insanın motor fonksiyonlarını ve yaşam kalitelerini etkilemektedir. Bu araştırma, ampute hastaların umut kaynağı olan yapay zeka tabanlı dış iskeletlerin ampute rehabilitasyonuna etkisini inceleyip kullanılan yapay zeka teknolojilerini karşılaştırmayı amaçladı. Bu amaç doğrultusunda literatür taranarak yapay zeka teknolojilerinden beyin-bilgisayar arayüzü, makine öğrenimi, derin öğrenme, yapay sinir ağlarının ampute hasta rehabilitasyonuna etkisi ile ilgili son 10 yılın araştırmaların nitel meta analizi yapıldı. Nitel meta analiz sonucunda ampute hasta rehabilitasyonunda en çok kullanılan yapay zeka teknolojisinin beyin-bilgisayar arayüzü olduğu ve kullanılan yapay zeka tabanlı dış iskeletlerin hepsinin rehabilitasyona olumlu etkisinin olduğu ayrıca bu yapay zeka teknolojileri sayesinde amputasyonlu hastaların hareket sınırlılıklarının azaldığı araştırmalarda görüldü.

**Anahtar Kelimeler:** Ampute hasta rehabilitasyonu, yapay zeka, beyin-bilgisayar arayüzü, dış iskeletler, derin öğrenme.



## I. GİRİŞ [INTRODUCTION]

Amputasyon, günlük yaşam aktiviteleri ve yaşam kalitesi üzerinde ani ve belirgin etkisi olan (Persine ve ark., 2022), vücuttaki uzuv veya ekstremitenin bir kısmının çıkarıldığı cerrahi bir prosedürdür (Kanchana. D ve ark., 2021). Vücudun bir bölümünün kaybı yaşam kalitesini önemli ölçüde etkilemekte, dolayısıyla fiziksel ve psikolojik sonuçlara neden olmaktadır (Egle ve ark., 2023). Dünya Sağlık Örgütü'ne (WHO) göre amputeler dünya nüfusunun yaklaşık %0,25'ini ve % 1,25'ini temsil etmektedir (Rodas ve Pérez, 2023). Raporlardan birine göre, her yıl 0,2 milyon ampute artış yaşanıyor ancak birçok ülke amputasyon istatistiklerini takip etmediğinden dünya çapında toplam uzuv ampute sayısını kesin olarak tespit etmek mümkün değildir (Kadir ve ark., 2021).

Bilgisayar tabanlı sistemlerin ve derin öğrenmeye dayalı algoritmaların hızlı gelişimi sayesinde, yapay zeka uzun süredir sağlık hizmetleri alanına entegre edilmiştir (Li ve ark, 2022). Ampute hastalarının rehabilitasyonunda da yapay zeka teknolojilerin kullanımı oldukça yaygındır ve giderek daha çok yaygınlaşmaktadır. Yapay zeka teknolojileri sayesinde çeşitli hastalık, doğuştan gelen hastalıklar ve kazalar sonucunda bir veya birkaç uzvunu kaybeden hastalar, kaybettikleri uzuvlarının motor fonksiyon işlevlerinin birçoğunu yerine getirmektedirler. Myoelektrik kontrol, beyin-bilgisayar arayüzleri, yapay sinir ağları, makine öğrenimi ve derin öğrenme gibi birçok yapay zeka tekonojisi ampute hasta rehabilitasyonunda kullanılmaktadır.

Bu çalışmada üst ekstremitte, alt ekstremitte ya da her ikisini birden kaybeden hastaları araştırarak bu hastaların günlük yaşamda karşılaştıkları zorlukları en aza indiren teknolojilerin kullanıldığı son 10 yılın araştırmaların meta analizini yapmıştır. Bu araştırma sayesinde başta fizyoterapistler olmak üzere bu alanda çalışan terapistlerin ve doktorların bu hastaların rehabilitasyonun da kullanılan teknolojileri ve etkilerini bir kaynaktan bularak bu hastalarının rehabilitasyonunu planlayabileceklerdir.

Bu çalışmada IEEE (Institute of Electrical and Electronics Engineers), Scencedirect, PudMed, Scopus veritabanları kullanarak 2013-2023 yılları arasında yayımlanan araştırmaların meta analizini yapmıştır. Ortaya çıkan sonuçlar tablolar ve grafikler şeklinde sunulmuştur.

## II. TEORİ VE YÖNTEM [THEORY AND METHODOLOGY]

### 1. Araştırma Yöntemi

Bu araştırma da literatür taraması metotlarından olan nitel meta-analiz yöntemi yani meta sentez kullanılmıştır. Nitel meta analiz, bir konu ile ilgili tüm çalışmaların kapsamlı şekilde toplanıp değerlendirme ve analizden sonra çıkan verilerden genel sonuca varmak için kullanılan yöntemdir. Yani meta-sentez, benzer bir konudaki farklı nitel çalışmaların bulgularını karşılaştırıp bütünleştirerek teorik bir model keşfetmek veya geliştirmek amacıyla kullanılan, nispeten yeni bir nitel yöntemdir (Güneş ve Erdem, 2022). İlk etapta sağlık bilimlerinde kullanılan meta-analiz yöntemi, bir ilacın etkisini incelenen, bir etkiye karşı bölgelerdeki ölüm oranlarını inceleme gibi amaçlarla kullanılmış, giderek yaygınlaşarak diğer bilim dallarında da kullanılmaya başlanmıştır (Dinçer, 2014). Bu araştırmada ise yapay zeka teknolojilerinden beyin bilgisayar arayüzü, makine öğrenimi, derin öğrenme ve yapay sinir ağlarının ampute hasta rehabilitasyonunda etkisinin nitel meta analizini yapmıştır.

### 2. Verilerin toplanması

Çalışma konusu belirlendikten sonra konu ile ilgili anahtar kelimeler belirlenmiştir. Belirlenen anahtar kelimeler 'ampute hasta', 'ampute hasta rehabilitasyonu', 'yapay zeka', 'beyin bilgisayar arayüzü', 'makine öğrenimi', 'derin öğrenme' ve 'yapay sinir ağı' kelimeleri kullanılmıştır. Bu anahtar kelimeler kullanılarak literatür taraması yapılmıştır.

Literatür taraması IEEE, Scencedirect, PudMed, Scopus veri tabanların da yapılmıştır. Ayrıca bu araştırma da 2013-2023 yılları arasındaki makaleler incelenmiştir. Literatür taraması sonucu dahil edilme kriterlerini taşıyan 20 makaleye ulaşılmıştır. Dahil edilme kriterleri Tablo 1'de gösterilmiştir.

**Tablo I.**

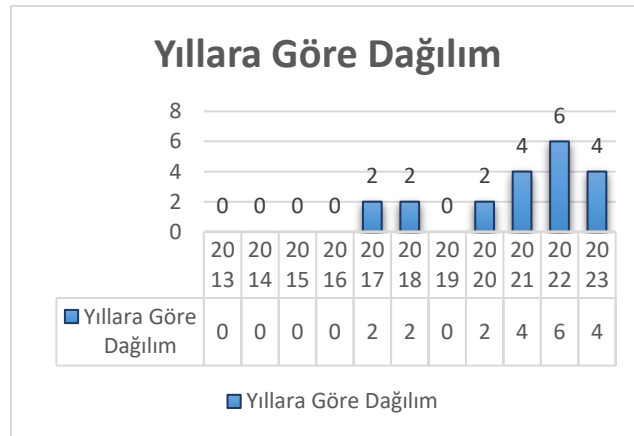
Araştırmaya dahil edilme kriterleri.

Dahil Edilme Kriterleri	
<b>Kriter 1</b>	2013- 2023 yılları arasında yayınlanmış olması
<b>Kriter 2</b>	IEEE, Sciencedirect, PudMed, Scopus veri tabanlarından birinde yayınlanmış olması
<b>Kriter 3</b>	Araştırmada hareket açığa çıkaracak dış iskelet olması
<b>Kriter 4</b>	Yapılan araştırmanın denek üzerinde denenmiş olması
<b>Kriter 5</b>	Araştırmada yapay zeka teknolojilerinden beyin bilgisayar arayüzü, beyin makine arayüzü, makine öğrenimi, derin öğrenme, yapay sinir ağı kullanılmış olması

Meta-sentez çalışmalarında anlamlı ve geçerli meta-sentezlere ulaşmak amacıyla çalışma amacına uygun en az 10-12 araştırmanın çalışmaya dâhil edilmesi önerilmektedir (Poggenpoel ve Myburgh, 2008: 66). Araştırma için de dahil edilme ölçütlerini sağlayan 20 makalenin orijinal metinleri araştırmacı tarafından okunarak araştırmalar hakkında detaylı bilgiler elde edilmiştir. Elde edilen bu bilgilerin meta analizi için içerik analizi tekniği ve betimsel analiz tekniği kullanılmıştır. Bu analiz şekli ampute hasta rehabilitasyonun da kullanılan yapay zeka teknolojilerinden BCI, derin öğrenme, makine öğrenimi, yapay sinir ağları kullanılarak yapılmış nitel ve nicel araştırmaların sonuçları tanınmış ve değerlendirilmiştir. Belirlenen çalışmalar yayımlandıkları yıllara, vücut segmentine, DoF sayısına, kullanılan denek ve cihazın uygulamasına göre sonuçlar incelenmiş ve analiz edilmiştir. Ve bu analizden elde edilen bulgular tablolar ile sunulmuştur.

### III. BULGULAR [RESULT]

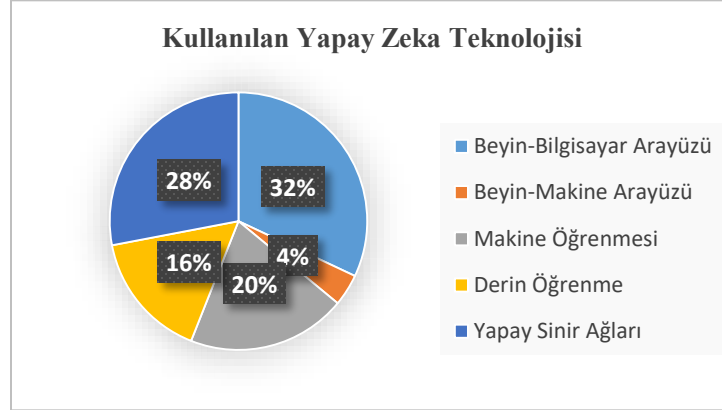
Araştırmanın bu bölümünde araştırmaya dahil olma kriterlerini taşıyan gerekli alt kategorilere ayrılmış, kodlamaları yapılmış, karşılaştırmaları yapılarak nitel meta analizi yapılmıştır. Ve sonuçlar tablolar halinde bu bölümde sunulmuştur. Karşılaştırma, belirlenen çalışmaların yayımlandıkları yıllara, kullanılan yapay zeka teknolojisine, vücut segmentine, DoF sayısına, kullanılan deneğe göre yapılmıştır. Şekil 1’de incelenen makalelerin yayımlandıkları yıllara göre dağılımını göstermektedir.



**Şekil 1:** Araştırmada kullanılan makalelerin yıllara göre dağılımı.

Şekil 1 incelendiğinde 2022’de 6 makale ile en fazla çalışmanın olduğu görülmektedir. 2013, 2014, 2015, 2016 ve 2019 yıllarında ise nitel meta analize dahil olma kriterlerini sağlayan çalışmalara ulaşılamadığı görülmektedir.

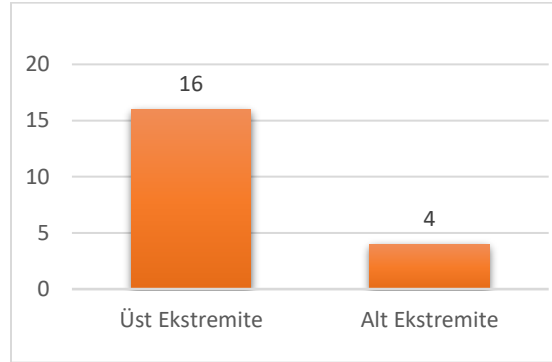
Şekil 2’de araştırmaya dahil edilen makalelerin kullandıkları yapay zeka teknolojisine göre dağılımı göstermektedir.



**Şekil 1:** Araştırmada kullanılan makalelerde kullanılan yapay zeka teknolojisinin dağılımı.

Şekil 2 incelendiğinde %32 oranla beyin-bilgisayar arayüzü ampute hasta rehabilitasyonunda en çok kullanılan yapay zeka teknolojisi olarak karşımıza çıkmaktadır. Daha sonra sırasıyla %28 oranla yapay sinir ağları, %20 oranla makine öğrenmesi, %16 oranla derin öğrenme ve en son olarak %4 oranla beyin-makine öğrenmesi gelmektedir.

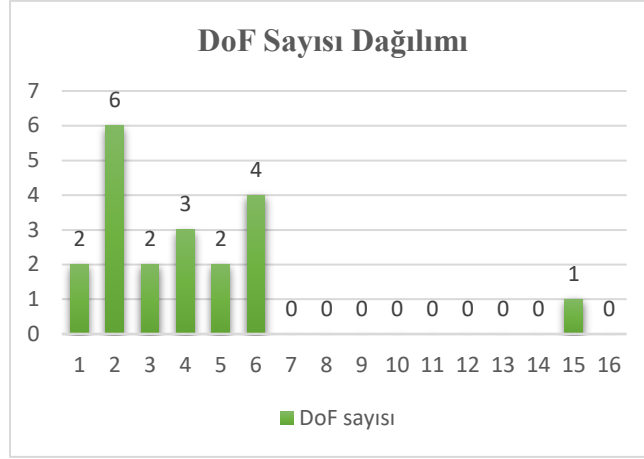
Şekil 3’te nitel meta analize dahil edilen araştırmaların hangi vücut segmentinde yapıldığını göstermektedir.



**Şekil 3:** Nitel meta analize dahil edilen araştırmaların araştırılan vücut segmentine göre dağılımı.

Şekil 3’te görüldüğü gibi bu araştırmada kullanılan makalelerde üst ekstremité alt ekstremitéye göre 4 kat daha fazla araştırmalarda tercih edilmektedir. Bunun nedeni merkezi sinir sisteminin bazı alanları EGG sinyallerini almak için daha elverişlidir. Örneğin beyindeki primer motor kortekste eli kontrol eden alanın yeri kabaca başın yan tarafıdır ama alt ekstremitenin herhangi bir yerinin kontrolü beyin kabuğunda spesifik olarak bulması daha zordur. Bu yüzden araştırmalarda daha çok üst ekstremité tercih edilmektedir.

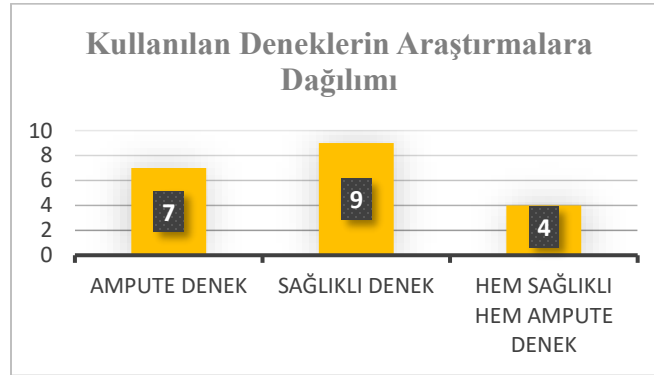
Şekil 4’te bu araştırmada tercih edilen makalelerde dış iskeletlerin DoF sayılarının dağılımı gösterilmektedir.



**Şekil 4:** Araştırmaya dahil edilen makalelerdeki dış iskeletlerin DoF sayılarının dağılımı.

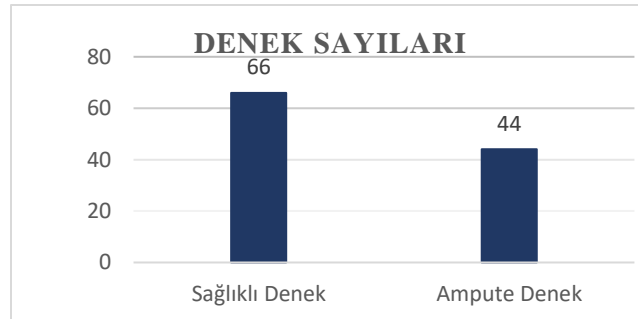
Şekil 4'te incelendiğinde araştırmaya dahil edilen araştırmalarda kullanılan dış iskeletlerin DoF sayılarının çoğunlukla 6 olduğu ve en fazla DoF derecesinin 15 olduğu görülmektedir. DoF sayıları arasındaki farkların olması kullanılan protezin üst ya da alt ekstremité olmasıyla değişebilir. Bunun nedeni üst ekstremité de ve alt ekstremité de bulunan eklemlerin görevleri ve hareketlerinin farklı olmasından kaynaklanmaktadır. Bu yüzden bir protez yapacağı göreve göre tek bir DoF derecesine de sahip olabilir 15 DoF derecesine de sahip olabilir.

Şekil 5'te kullanılan deneklerin araştırmalara dağılımı gösterilmektedir.



**Şekil 5:** Kullanılan deneklerin araştırmalara dağılımı.

Şekil 5 incelendiğinde sağlıklı denekler araştırmalarda daha çok kullanıldığı görülmektedir. Araştırmaların bu şekilde karşılaştırma yaparak yapay zeka teknolojilerini karşılaştırması araştırmanın daha sağlıklı sonuç vermesini sağlamaktadır.



**Şekil 6:** Araştırmalarda kullanılan deneklerin sayıları



Şekil 6 incelendiğinde araştırmalarda toplam 100 denek kullanıldığı görülmektedir. 66 sağlıklı denek, 44 tane ise ampute denek üzerinde yapay zeka teknolojisi test edilmiştir. Kullanılan bu teknolojilerin ampute hasta rehabilitasyonu üzerinde etkisini tam olarak anlamak için ampute hasta üzerinde daha çok araştırma yapılmalıdır.

#### IV. TARTIŞMA [ARGUMENT]

Bir uzvun amputasyonu, travmatik yaralanma, yanık, periferik damar hastalığı, enfeksiyon vb. gibi çeşitli nedenlerle bir bacağın, kolun veya bu uzuvların bir kısmının kaybedilmesidir (Saini ve ark., 2023). Bu yüzden travmatik ekstremitte amputasyonu hastaların fonksiyonel ve psikolojik sağlığı açısından yıkıcı olabilir (Schultz ve ark., 2023). Ampute hastaların bu sorunlarını azaltmak için birçok tedavi ve rehabilitasyon yöntemi geliştirilmiştir. Son yıllarda bu alanda yapılan araştırmalar teknolojinin gelişmesiyle artmış ve amputasyonlu hastaların sosyal hayata katılımlarını artırmak için umut kaynağı olmuştur. Çünkü zihin kontrollü bir robotik protez; amputasyon, travma geçiren veya uzuv olmadan doğan hastaların tam ve eksiksiz hareket kabiliyetine sahip olmalarına olanak tanıyacaktır (Anisha ve ark., 2021).

Ampute hastalar için kullanılan yapay zeka tabanlı dış iskeletleri ve bu iskeletlerin rehabilitasyona etkisini araştırmayı amaçlayan bu araştırma bu alanda yapılan araştırmaların meta analizini yapmıştır. Bu araştırma için 2013-2023 yılları arasındaki makaleler incelenmiştir. Ayrıca bu meta analizi gerçekleştirebilmek için 4 veri tabanında literatür taraması yapılmıştır. Bunlar IEEE, Sciencedirect, PudMed, Scopus veri tabanlarıdır. Bu veri tabanlarından toplam da dahil edilme kriterlerini taşıyan 20 araştırmaya ulaşılmıştır. Bu araştırmaların anahtar kelimeleri ise ‘ampute hasta’, ‘ampute hasta rehabilitasyonu’, ‘yapay zeka’, ‘beyin bilgisayar arayüzü’, ‘makine öğrenimi’, ‘derin öğrenme’ ve ‘yapay sinir ağı’ şeklindedir.

Araştırmanın bulguları arasında ampute rehabilitasyonunda kullanılan yapay zeka tabanlı dış iskeletlerin son yıllarda kullanımı gittikçe arttığı görülmektedir. Bunun nedeni beyin bilgisayar arayüzü, derin öğrenme, yapay sinir ağları gibi yapay zeka teknolojilerinin son yıllarda popüler olması ve buna bağlı geliştiği düşünülmektedir. Beyin araştırmalarındaki ilerlemeler, engelli hastalarla yapılan çalışmalar da dahil olmak üzere, beyin-bilgisayar arayüzleri aracılığıyla motor eksiklikleri aşmak için bir dizi umut verici fırsat ortaya çıkardı (Cohen ve ark., 2017). Yapılan bu meta analizde de ampute rehabilitasyonunda en fazla beyin-bilgisayar arayüzü kullanıldığı görülmüştür. Beyin- bilgisayar arayüzü hem bozulmuş motor fonksiyonun güçlendirilmesinde hem de felç iyileşmesi gibi rehabilitasyonda umut verici bir avantaj sunmaktadır (Yao ve ark., 2013). Ancak bu alanın hızla genişlemesine rağmen BCI performansının nihai sınırlarının ne olduğu belirsizdir (Cohen ve ark., 2017).

Bu nitel meta analize dahil edilen araştırmalarda yapay zeka tabanlı dış iskeletlerde en az 1 en fazla 15 DoF kullanıldığı tespit edilmiştir. Kullanılan dış iskeletlerde DoF sayısı arttıkça protezin hareket yeteneği artar. Örneğin insan eli, insan vücudundaki en karmaşık ve olağanüstü araçlardan biridir. 27 kemik ve 33 kasın ortak çalışmasıyla 22 DoF sunar (Rehman ve ark., 2022) ama bu araştırmanın bulgularına göre el için yapılan dış iskeletler genellikle 1-6 DoF derecesi arasında değişmektedir. Bu yüzden protezlere yönelik geleneksel kontrol yaklaşımları, birden fazla DoF aynı anda çalıştırırken başarısız oluyor, dolayısıyla günlük yaşam senaryolarında kullanılabilirliği sınırlanıyor (Egle ve ark., 2023). Sınıflandırıcılar, sinyal özelliklerini, bilinen DOF'ler ayrı bir kümesinden (kategoriler) biriyle eşler , birden fazla DOF üzerinde kontrol sunar, ancak cihaz hareket hızı üzerinde orantılı kontrol veya birden fazla DOF üzerinde eşzamanlı kontrol sağlamaz (Williams ve ark., 2022). Dolayısıyla gelecekteki araştırmalarda ampute hastaların kaybettikleri motor fonksiyonlarının çoğunu yerine getirebilmeleri için sınıflandırıcıların yani makine öğrenimi, derin öğrenme, yapay sinir ağları ve bunların alt dallarının geliştirilmesi ve gelecekte bu alanda daha çok araştırma yapıp DoF derecesi daha yüksek yapay zeka tabanlı protezler üretilmesine ihtiyaç vardır.

Araştırmanın bir diğer bulgusu ise daha çok üst ekstremitte amputasyonu olan hastalar için yapay zeka destekli dış iskeletler kullanılarak araştırma yapılmıştır. Bunun nedenleri arasında üst ekstremitte amputasyonuna sahip hastaların daha fazla olması ve kullanılan teknolojilerin üst ekstremitte amputasyonlu hastalara daha uygun olmasına bağlı olabilir. Ek olarak üst ekstremitenin beyinde kapladığı motor alandan EGG sinyali almak alt ekstremitteye göre daha kolay olabilir. Bu da üst ekstremitte amputelerine EGG sinyali için daha fazla kanal kullanma fırsatı sunar. Bazı

çalışmalar birden fazla kanalın kullanılmasının faydalı olduğunu göstermiş ve kanallar arttıkça ortalama sınıflandırma doğruluğunun da artacağını bulmuştur (Elbreki ve ark., 2022).

Birleşmiş Milletler'e (BM) göre dünya çapında insanların yaklaşık %10'unun (yaklaşık 650 milyon) engelli olduğu kaydedilmiştir; bu durum tam da nüfus artışı, tıptaki ilerlemeler ve yaşlanma süreci nedeniyle artmaktadır (Rodas ve Pérez, 2022). Bu nitel meta analizde kullanılan araştırmaların sonuçlarına baktığımızda ise kullanılan yapay zeka teknolojilerinin rehabilitasyon sürecine hepsinin olumlu sonuçları olduğunu görmekteyiz. Amputasyonlu insan sayısı arttığı için ve bu yapay zeka teknolojisinin de olumlu dönüşleri olduğu için gelecekte bu alanda yapılan araştırmaları çoğaltıp teknolojiyi daha geliştirerek ampute hastaların günlük yaşam da karşılaştıkları zorlukları azaltabilmek mümkündür. Bu yüzden beyin-bilgisayar arayüzü, derin öğrenme, makine öğrenmesi gibi yapay zeka teknolojilerinin daha yaygın kullanılması önemlidir.

## V. SONUÇ VE DEĞERLENDİRME [CONCLUSION]

Son yıllarda herhangi bir nedenle amputasyon cerrahisi geçiren ya da doğuştan uzvu olmayan insanlar için günlük yaşama katılımlarını artıran cihazların gelişmesinde yapay zeka teknolojileri kullanılmaktadır. Amputasyon rehabilitasyonunda da daha çok beyin-bilgisayar arayüzleri, makine öğrenmesi ve alt dalları kullanılmaktadır. Bu yapay zeka teknolojileri niyet kodunun çözülmesi ve istenilen hareketin dış iskelette ortaya çıkarılmasına dayanır. Bu meta analizde kullanılan araştırmalarda bu niyet kodunun çözülmesi, sınıflandırılması gibi çeşitli işlemlerden geçip dış iskelette istenilen hareketi ortaya çıkarma prensibine dayanan araştırmalar kullanılmıştır. Bu araştırmaların ortak sonucu ise amputasyonlu hastalarda kullanılan dış iskeletlerde yapay zeka teknolojisi güvenilir sonuçlar vermektedir. Ortaya çıkan bu sonuçta ise amputasyonlu hastalar için umut kaynağı olmuştur. Ayrıca yapay zeka teknolojilerinin, robotik sistemlerin ve rehabilitasyon yöntemlerinin giderek daha çok yaygınlaşması ve gelişmesiyle bugün tamamen işlevsel protez yani dış iskeletlere sahip olmamızın çok uzakta olmadığı görülmektedir.

Bu çalışmanın sonuçlarına dayanarak ampute hastaların rehabilitasyon sürecinde yapay zeka teknolojilerini, yapay zeka tabanlı dış iskeletlerini aktif olarak kullanmalarını ve yapay zeka teknolojilerinin ampute hasta rehabilitasyonu üzerinde etkilerini daha iyi anlamak için gelecekte bu alanda daha çok araştırma yapılması önerilmektedir. Çünkü son yıllardaki ilerlemeci gelişmelere rağmen hala kaybedilen uzvun tam işlevini görebilecek dış iskelet üretilmemiştir. Ayrıca kontrol paradigmalarını ve rehabilitasyon etkisini kapsamlı bir şekilde değerlendirebilmek için hem ampute denek üzerinde hem de sağlıklı denek üzerinde geniş bir popülasyona sahip daha fazla araştırmaya gerek vardır.

## KATKI ORANI BEYANI [STATEMENT OF CONTRIBUTION RATE]

1. yazar %60 oranında, 2. yazar %40 oranında katkı sağlamıştır.

## ÇIKAR ÇATIŞMASI [CONFLICTS OF INTEREST]

Yazarlar arasında ve ilgili kurumları arasında herhangi çıkar çatışması bulunmamaktadır.

## ETİK KURALLARA UYGUNLUK [COMPLIANCE WITH ETHICAL RULES]

Bu makale etik kurul onayı veya herhangi bir özel izin gerektirmemektedir.

## TEŞEKKÜR [ACKNOWLEDGMENT]

Makale çalışmasına yaptığı destekler için değerli hocam Prof. Dr. Türker Tekin Ergüzel'e teşekkür ederim.

**KAYNAKLAR [REFERENCES]**

- [1] Zhouxiao Li, Konstantin Christoph Koban, Thilo Ludwig Schenck, Riccardo Enzo Giunta, Qingfeng Li, Yangbai Güneşi (2022). Artificial Intelligence in Dermatology Image Analysis: Current Developments and Future Trends. *J. Clin. Med.* 11(22), 6826.
- [2] Persine Anran Wang, Xiaolei Xiu, Shengyu Liu, Qing Qian, Sizhu Wu (2022). Characteristics of Artificial Intelligence Clinical Trials in the Field of Healthcare: A Cross-Sectional Study on ClinicalTrials.gov. *Int. J. Environ. Res. Public Health* 19(20), 13691.
- [3] D, Kanchana, V, Vinothkumar., D, E. Samhithan. (2021). Gesture Controlled Robotic Hand Prosthesis for Upper Limb Amputee Rehabilitation. *2021 IEEE Bombay Section Signature Conference (IBSSC)*, 1-5.
- [4] Fabio Egle, Dario Di Domenico, Andrea Marinelli, Nicolò Boccardo, Michele Canepa, Matteo Laffranchi... Claudio Castellini. Preliminary Assessment of Two Simultaneous and Proportional Myocontrol Methods for 3-DoFs Prostheses Using Incremental Learning. *2023 International Conference on Rehabilitation Robotics (ICORR)* (24-28.09.2023).
- [5] Dana Terrazas-Rodas and Joanna Carrión-Pérez. The Use of Invasive and Non-Invasive Electrodes in Novel Technology of Upper Limb Prostheses: A Current Review. *2023 International Seminar on Intelligent Technology and Its Applications (ISITIA)* (23.08.2023)
- [6] Muhammed Osman Kadir, Muhammed Awais Han, Muzammal Hüseyin, Izhar ul Haq, Nizar Ahtar, Kmaran Şah. Design and Analysis of Knee Joint for Transfemoral Amputees. *2021 International Conference on Artificial Intelligence and Mechatronics Systems (AIMS)* (28-30.04.2021).
- [7] Güneş, D. ve Erdem, R. (2022). Nitel araştırmaların analizi: Meta-sentez. *Anadolu Üniversitesi Sosyal Bilimler Dergisi*, 22(Özel Sayı 2), 81-98.
- [8] Dinçer, S. (2014). *Eğitim Bilimlerinde Uygulamalı Meta Analiz*. Pegem Akademi Yayıncılık, 2-25.
- [9] Poggenpoel, M. ve Myburgh, C. P. H. (2008). A Meta-Synthesis of Completed Qualitative Research on Learners' Experience of Aggression in Secondary Schools in South Africa. *International Journal of Violence and School*, (8), 60-84.
- [10] Uttam Chand Saini, Shubhankar Bu, Himanshu Bhayana, Mandeep Singh Dhillon, Aseem Mehra (2023). Longitudinal Experience and Determinants for Common Mental Health Problems, Phantom Limb and Functional Outcome in Lower Limb Amputees. *Indian Journal of Orthopaedics*, 57, 2040–2049.
- [11] Blake Schultz, Hristiyan Fıstığın, Nirmal Tejawani (2023). Updates on Residual Limb Management in Lower Extremity Amputation From Nerve to Bone. *Bull Hosp Jt Dis* (2013), 81(4): 240-248.
- [12] M. Anisha, M. Sushmitha, S. Surekha, N. Vigneshwari, Ponmozhi Chezhiyan, C. Jim Elliot... SB Pooja. Exploration on Electroencephalogram Controlled Haptic Humanoid Arm for amputees. *2021 Second International Conference on Electronics and Sustainable Communication Systems (ICESC)* (04-06.08.2021).
- [13] Ori Cohen, Dana Doron, Moşe Koppel, Rafael Malach, Doron Friedman. High performance in brain-computer interface control of an avatar using the missing hand representation in long term amputees. *2017 8th International IEEE/EMBS Conference on Neural Engineering (NER)* (25-28.05.2017).
- [14] Lin Yao, Xiaokang Shu, Jianjun Meng, Dingguo Zhang, Xinjun Sheng, Xiangyang Zhu. Enhanced motor imagery based brain-computer interface via unilateral wrist vibrotactile stimulation. *2013 6th International IEEE/EMBS Conference on Neural Engineering (NER)* (06-08.11.2013).
- [15] Mustafa Ür Rehman, Kamran Şah, İzhar Ul Haq, Hasan Hurşid. A Force Myography based HMI for Classification of Upper Extremity Gestures. *2022 2nd International Conference on Artificial Intelligence (ICAI)* (30-31.03.2022).
- [16] Heather E. Williams, Ahmed W. Şehata, Michael R. Dawson, Erik Şeması, Jacqueline S. Hebert, Patrick M. Pilarski (2022). Recurrent Convolutional Neural Networks as an Approach to Position-Aware Myoelectric Prosthesis Control. *IEEE Transactions on Biomedical Engineering*, 69 (7), 2243 – 2255.
- [17] AM Elbreki, Safa Ramazan, Faysal Muhammed, Khadija Alshari, Zakariya Rajab, B. Elhub. Practical Design of an Upper Prosthetic Limb Using Three Dimensional Printer with an Artificial Intelligence Based Controller. *2022 International Conference on Engineering & MIS (ICEMIS)* (04-06.07.2022).
- [18] Dana Terrazas-Rodas and Joanna Carrión-Pérez. Artificial Intelligence Techniques for Biosignal Pattern Recognition and Classification in Upper-Limb Prostheses: A Review. *2022 IEEE International Conference on Internet of Things and Intelligence Systems (IoTaIS)* (24-26.11.2022).
- [19] Morten B. Kristoffersen, Andreas W. Franzke, Raoul M. Bongers, Michael Wand, Alessio Murgia, Corry K. van der Sluis (2021). User training for machine learning controlled upper limb prostheses: a serious game approach. *Journal of NeuroEngineering and Rehabilitation*, 18, 32.
- [20] Anh Tuan Nguyen, Jian Xu, Ming Jiang, Diu Khue Luu, Tong Wu, Wing-kin Tam... Qi Zhao (2020). A bioelectric neural interface towards intuitive prosthetic control for amputees. *Journal of Neural Engineering*, 17,6.
- [21] Zheng You Lim and Neo Yong Quan. Convolutional Neural Network Based Electroencephalogram Controlled Robotic Arm. *2021 IEEE International Conference on Automatic Control & Intelligent Systems (I2CACIS)* (26.06.2021).
- [22] Bin Fang, Chengyin Wang, Fuchun Güneş, Ziming Chen, Jianhua Shan, Huaping Liu... Wenyuan Liang (2022). Simultaneous sEMG Recognition of Gestures and Force Levels for Interaction With Prosthetic Hand. *IEEE Transactions on Neural Systems and Rehabilitation Engineering*, 30 (2426 – 2436).

- 
- [23] Minjae Kim, Ann M. Simon, Levi J. Hargrove (2022). Seamless and intuitive control of a powered prosthetic leg using deep neural network for transfemoral amputees. *Wearable Technologies*, 3.
- [24] Elaine M. Bochniewicz, Geoff Emmer, Alexander W. Dromerick, Jessica Barth, Peter S. Lum (2023). Measurement of Functional Use in Upper Extremity Prosthetic Devices Using Wearable Sensors and Machine Learning. *Sensors*, 23(6).
- [25] Markus Nowak, Raoul M. Bongers, Corry K. van der Sluis, Alin Albu-Schäffer, Claudio Castellini (2023). Simultaneous assessment and training of an upper-limb amputee using incremental machine-learning-based myocontrol: a single-case experimental design. *Journal of NeuroEngineering and Rehabilitation*, 20.
- [26] Author links open overlay panel Baao Xie, James Meng, Baihua Li, Andy Harland (2022). Biosignal-based transferable attention Bi-ConvGRU deep network for hand-gesture recognition towards online upper-limb prosthesis control. *Computer Methods and Programs in Biomedicine*, 224.
- [27] Sachin Kansal, Dhruv Garg, Aditya Upadhyay, Snehil Mittal, Guneet Singh Talwar (2023). DL-AMPUT-EEG: Design and development of the low-cost prosthesis for rehabilitation of upper limb amputees using deep-learning-based techniques. *Engineering Applications of Artificial Intelligence*, 126.
- [28] Anh Tuan Nguyen, Jian Xu, Ming Jiang, Diu Khue Luu, Tong Wu, Wing-kin Tam... Qi Zhao (2020). A bioelectric neural interface towards intuitive prosthetic control for amputees. *Journal of Neural Engineering*, 17,6.
- [29] DSV Bandara, Jumpei Arata, Kazuo Kiguchi (2018). Towards Control of a Transhumeral Prosthesis with EEG Signals. *Bioengineering*, 5(2), 26.
- [30] Arnau Dillen, Elke Lathouwers, Aleksandar Miladinović, Uros Marusić, Fakhreddine Ghaffari, Olivier Romain... Kevin De Pauw (2022). A data-driven machine learning approach for brain-computer interfaces targeting lower limb neuroprosthetics. *Front. Hum. Neurosci.*, 16.
- [31] An Tuan Nguyen, Markus W Drealan, Diu Khue Luu, Ming Jiang, Jian Xu, Jonathan Cheng... Zhi Yang (2021). A Portable, Self-Contained Neuroprosthetic Hand with Deep Learning-Based Finger Control. *J Neural Eng.*, 11;18(5).
- [32] Douglas P. Murphy, Ou Bai, Ashraf S. Gorgey, John Fox, William T. Lovegreen, Brian W. Burkhardt... Ding-Yu Fei (2017). Electroencephalogram-Based Brain-Computer Interface and Lower-Limb Prosthesis Control: A Case Study. *Front. Neurol.*, 8.
- [33] G Gayathri, Ganesha Udupa, G. J. Nair. Control of bionic arm using ICA-EEG. *2017 International Conference on Intelligent Computing, Instrumentation and Control Technologies (ICICT)* (06-07.07.2017).
- [34] Mojisola Grace Asogbon, Oluwarotimi Williams Samuel, Xiangxin Li, Naifu Jiang, Naifu Jiang, Oluwagbenga Paul Idowu, Yanbing Jiang... Guanglin Li. A Low-rank Spatiotemporal based EEG Multi-Artifacts Cancellation Method for Enhanced ConvNet-DL's Motor Imagery Characterization. *2021 43rd Annual International Conference of the IEEE Engineering in Medicine & Biology Society (EMBC)* (01-05.11.2021).
- [35] Mojisola Grace Asogbon, Oluwarotimi Williams Samuel, Xiangxin Li, Naifu Jiang, Naifu Jiang, Oluwagbenga Paul Idowu, Yanbing Jiang... Guanglin Li. A Robust Multi-Channel EEG Signals Preprocessing Method for Enhanced Upper Extremity Motor Imagery Decoding. *2020 IEEE International Conference on Mechatronics and Automation (ICMA)* (13-16.10.2020).
- [36] Diego Ronaldo Cutipa-Puma, Cristian Giovanni Coaguila-Quispe, Pablo Raul Yanyachi (2023). A low-cost robotic hand prosthesis with apparent haptic sense controlled by electroencephalographic signals. *HardwareX*, 14.
- [37] Muhammad Yasin, Achmad Arifin, Muhammad Hilman Fatoni. Ankle Prosthesis With Brain Computer Interface Commands Based on Electroencephalograph for Transtibial Amputees. *2022 International Seminar on Intelligent Technology and Its Applications (ISITIA)* (20-21.07.2022).
- [38] Kaushalya Kumarasinghe, Mahonri Owen, Denise Taylor, Nikola Kasabov, Chi Kit. FaNeuRobot: A Framework for Robot and Prosthetics Control Using the NeuCube Spiking Neural Network Architecture and Finite Automata Theory. *2018 IEEE International Conference on Robotics and Automation (ICRA)* (21-25.05.2018).





## RESEARCH ARTICLE

# Solution for Integration of Renewable Energy Power Plants into Smart Grids with Active Power Control

\* Mehmet Necat TUR,<sup>1</sup> Omer Faruk ERTUGRUL<sup>2</sup> Mehmet Rida TUR<sup>2</sup>

\* Dicle Electricity Corporation, Ankara, Turkey  
necattur@gmail.com, Orcid. 0009-0006-0212-7234,

\* Batman University, Faculty of Engineering and Architecture, Electrical Engineering Department, Batman, Turkey  
omerfaruk.ertugrul@batman.edu.tr, Orcid. 0000-0003-0710-0867,

\* Batman University, Faculty of Engineering and Architecture, Electrical Engineering Department, Batman, Turkey  
mrida.tur@batman.edu.tr, Orcid. 0000-0001-5688-4624,

**Citation:**

Tur, M.N., Ertugrul, Ö.F., Tur, M.R. (2024). *Solution for Integration of Renewable Energy Power Plants into Smart Grids with Active Power Control*, Journal of Science Technology and Engineering Research, 5(1): 11-23. DOI: 10.53525/jster.1409505

**HIGHLIGHTS**

- Effect and important of this article in literature
- Exchange between sources in related subjects of this article
- Contribution and strongest impact on the related subject of this article
- Examined study and obtained results why is important

**Article Info**

Received : 25 December 2023

Accepted : 14 April 2024

**DOI:**

10.53525/jster.1409505

**\*Corresponding Author:**

Mehmet Necat Tur  
necattur@gmail.com

**ABSTRACT**

*This article addresses the integration of renewable energy power plants into smart grids and active power control. Renewable energy sources contribute to environmentally friendly and sustainable energy production, but the fluctuations inherent in these sources pose a challenge for energy grids. The article examines various technologies that can be used to overcome this challenge and make energy grids more reliable. Smart grids aim to improve energy grids by optimizing energy production, transmission, and distribution using data analytics, automation, and communication technologies. The integration of renewable energy power plants into these smart grids offers significant advantages, including the ability to predict energy production, integrate with energy storage systems, and manage energy demand. The article also emphasizes the importance of active power control. Active power control is used to manage energy production steadily, thereby maintaining grid stability. Balancing energy fluctuations from renewable energy sources and storing excess energy when needed enhances grid stability. In conclusion, this article discusses the crucial role of integrating renewable energy power plants into smart grids and implementing active power control in the energy sector. These integration and control methods are important steps in making energy grids more sustainable, efficient, and reliable.*

**Keywords:** Renewable Energy, Smart Grids, Active Power Control

## I. INTRODUCTION

Energy strategies are underpinned by the expanding utilization of natural gas and renewable energy sources (RES), coupled with an increased focus on enhancing energy efficiency. Nonetheless, recent government initiatives have shifted towards the promotion of innovative and sustainable energy resources. The national "Renewable Energy 3020 Implementation Plan" is geared towards augmenting the share of renewable energy generation to approximately 20% by 2030. Presently, the proportion of renewable energy generation lags behind that of major nations; hence, the government aspires to achieve this objective by providing clean energy, such as solar and wind power, to over 95% of new installations [1]. Furthermore, there is a growing trend in the adoption of Distributed Energy Resources (DERs) connected to small-scale distribution systems due to their rapid deployment and cost advantages [2, 3]. Nevertheless, variations in active power output resulting from wind and photovoltaic (PV) generation can introduce instability due to fluctuations in solar radiation and temperature shifts. Additionally, voltage-related issues like under-voltage and overvoltage complications can manifest in the power distribution network.

Creating a sustainable energy system and meeting the increasing demand for electrical load requires the integration of Renewable Energy Sources (RES) models into the grid [4]. However, this poses several challenges in providing active power control, and this generational transformation of the power system requires a more extensive communication network to maintain grid integrity [5, 6]. Many existing RES technologies are highly dependent on geographical and environmental factors, making them unpredictable and uncontrollable, thus limiting their large-scale integration into power grids. This also necessitates innovative strategies in renewable integration along with demand-side management [7-9]. Most of the current solutions in the literature, such as renewable forecasting, peak shaving, load filling, power electronic converters, smart meters, and smart inverters, rely on state-of-the-art communication networks for their effectiveness. Therefore, establishing an effective smart grid enables load management, significantly reduces system losses and energy wastage, provides accurate data monitoring, and ensures flexibility in expansion and integration within the power system network. Similarly, the electricity grid, with limited sensing devices, manual control, and maintenance, offers customers limited participation options [10-13]. In this context, the smart grid focuses on maintaining intergenerational diversity with updated processes, enhanced efficiency, and active power control. Through intensive observation-based automation, utilizing smart and digitalized energy solutions, it ensures flexibility, self-healing, resilience, reliability, customer involvement, and security in the power system network [14]. Globally, there is a systematic transition towards smart grid development, observed concurrently with intense innovation in each smart grid framework domain, considering their respective challenges [15, 16]. However, this multidisciplinary theory and application of multi-faced research and industrial development need to consider the technical, economic, and social requirements of participants. From the perspective of the power grid, technical challenges include diversity and distributed transformation while maintaining power quality, stability, and flow appropriately [17]. Power system operators and planners ensure the technical and economic viability of the smart grid; thus, research efforts towards better interoperability will lead to the development and formulation of standards and protocols enabling the integration of existing and emerging smart grid technologies of energy, communication, and information into grid operation concurrently and expeditiously, potentially reducing overall costs through technological diversification. Socially, government incentives encourage customers to transition to prosumers and participate in the electricity market [18-20]. The progress of smart grid realization and expansion depends on social aspects related to transparency, including security, justice, and trust among smart grid participants. In this regard, numerous conceptual, terminological, and componential analyses of smart grids have been extensively presented to outline their foundational understanding and technological operation [21, 24]. Additionally, to accelerate smart grid visualization and creation, analytical, strategic, and business models such as Strengths, Weaknesses, Opportunities, and Threats (SWOT), Political, Economic, Sociological, Technological, Legal, and Environmental (PESTLE), etc., have been presented to promote smart grid feasibility [25-28]. These models have helped identify relevant factors hindering successful smart grid implementation [29-31]. Based on available literature models, this review article focuses on the perspective of power system planners and customers regarding the required technological innovations and considerations needed for accelerated smart grid development and implementation

[32]. Compared to some recent works, this study makes a substantial contribution by effectively amalgamating current knowledge in the fields of smart grids, renewable energy sources, energy storage, and communication systems comprehensively. Specifically, it precisely delineates areas of inquiry that have not been well-addressed, providing direction for future research and serving as a helpful reference for academic researchers [33, 34]. The paper's value is enhanced by its practical focus on difficulties and solutions, as well as its distinctive bottom-up methodology [35]. The review focuses on current developments and addresses contemporary concerns in the power sector, maintaining its relevance to ongoing conversations [36]. Furthermore, the aim is to bridge the gap between strategic reviews and quantifying their technological equivalents in terms of smart grid technologies by highlighting identified smart grid analytical models and translating them into technological research advancements and focus areas needed for smart grid realization.

Numerous methodologies have been proposed to address voltage problems triggered by DERs within a power distribution system. One technique employed to mitigate overvoltage issues is the on-load tap changer and step voltage regulator. These voltage control components are effectively deployed in conventional general distribution networks. However, the effectiveness of voltage control has become increasingly variable and unpredictable due to the recent elevation in voltage levels at the terminus of the distribution network, stemming from the upsurge in solar energy production. In conformity with the traditional distribution network's voltage profile, the measured voltage tends to be low owing to the distance of the voltage measurement point from the voltage source. Currently, voltage rise is observed at the end of the distribution line, and as a result, DER connections engender overvoltage predicaments, including reverse power flow (RPF) within the distribution network.

In summary, it is imperative to take voltage issues into account in bi-directional power flow scenarios and enhance the stability of the distribution network under multifaceted circumstances. The concept of a smart inverter pertains to a category of inverters capable of independently regulating DER output. These intelligent inverters operate to ensure the stability of the distribution network and encompass functionalities such as fixed power factor control, voltage-reactive power control, voltage-power control, frequency-power control, voltage ride-through, frequency ride-through, as well as manual active and reactive power control, among others. The autonomous functions needed for system stabilization are defined in the IEEE 1547-2018 standards. The application of test procedures and the definition of control criteria are structured to facilitate the utilization of an IEC 61850-7-520-based communication interface, which includes pivotal input parameters like voltage-reactive power control (VVC) and voltage-power control (VWC) [37, 37]. The VVC control method fine-tunes the voltage at the point of common coupling (PCC) for the PV inverter. In accordance with a predefined VVC curve, the inverter is adjusted to either absorb or inject reactive power. Current grid infrastructure requires updates to preserve grid flexibility, encompassing various operational facets associated with the integration of renewable energy sources [38]. These facets include generation, transmission, distribution, operational management, and power system planning [39, 40]. Efforts are underway to address short and long-term uncertainties, facilitating grid transformation and diversification [41-43].

Energy Storage Systems (ESSs) are predominantly intricate and nonlinear systems, hence their efficiencies cannot be succinctly quantified by a single numerical value (e.g., an average efficiency of 90%) [43-46]. This complexity arises due to a myriad of factors that necessitate consideration: the specific application (operational cycle), the efficiency of each module and subsystem within the ESS facility (comprising the aggregate of individual module efficiencies), operational conditions of the device, and the instantaneous power profile delivered by the ESS facility, among others. Consequently, it is imprudent to treat ESS efficiency as a static, singular value. Rather, a comprehensive evaluation of efficiency, contingent upon a multitude of parameters (including power requirements, consumption or generation, system configurations, and state of charge), is imperative. Furthermore, this efficiency evaluation should be customized to a specific application and operational cycle [44, 45]. Thus, a nuanced analysis is crucial to enhancing the sizing process of ESS facilities.

## II. POWER BALANCE WITH STORAGE METHOD

Smart grids, along with distributed energy systems like energy communities and energy hubs, are emerging as a viable alternative to traditional grids. They offer solutions to grid expansion challenges, reducing transmission losses, and addressing environmental concerns by facilitating the integration of a higher share of renewable energy technologies. Recent years have witnessed growing public acceptance of distributed renewable energy systems, with some countries achieving as much as 10% of their electricity production from these sources [46, 47]. While distributed energy systems offer numerous advantages such as proximity to energy demand centers, emissions reduction, and decreased renewable energy technology costs, they also present considerable hurdles in ensuring a stable and dependable energy supply due to the variable nature of renewable energy sources (RES). ESS have emerged as a promising means to mitigate the fluctuations in RES and enhance the reliability of distributed energy systems. They play a pivotal role in the global transition towards sustainable energy systems, offering a wide array of services to facilitate this shift, including active and reactive power regulation, frequency management, reserve capacity, and various grid services [48-50]. Additionally, ESS can enhance the energy self-sufficiency and self-consumption metrics of energy communities [51-53], leading to improved grid flexibility and lower energy expenses. These systems can absorb surplus energy when electricity demand is low and feed it back into the grid during peak demand, contributing to grid stability. The cost of energy storage has seen a remarkable reduction over the last decade, particularly in the case of lithium-ion (Li-ion) batteries, which have experienced an 85% cost decrease thanks to widespread deployment.

Determining the appropriate size of ESS is a critical area of research for professionals involved in the design and implementation of DERs, typically in the context of independent PV systems. Sizing methodologies aim to strike a balance between PV and ESS capacities, ensuring that they can deliver energy at a desired level of reliability and meet user demands. The reliability of an independent system is commonly assessed using the Loss of Load Probability (LOLP) metric [54, 55], which represents the ratio of the expected energy deficit to the total energy demanded during the entire operational period. An optimization-based sizing methodology has been developed for independent PV systems, incorporating reliability considerations and leveraging long-term data. The methodology explores different combinations of battery capacity and PV array size to meet specific LOLP targets, ultimately identifying the PV-battery configuration that minimizes the total system cost.

The importance of determining suitable sizes for ESS is highlighted for experts in the DERs sector. Sizing methodologies aim to achieve the provision of energy at the desired reliability level and meet user demands by establishing a balance between PV and ESS capacities. Additionally, it indicates the increasing prevalence of energy storage systems in grid systems alongside the growing utilization of renewable energy. However, it underscores the variation of ESS technologies based on various applications, emphasizing the significance of identifying appropriate applications. The text underscores the flexibility of sizing methodologies, enabling the reassessment of ESS sizes in existing systems. Finally, it emphasizes the importance of incorporating energy storage efficiency into the sizing process, thereby facilitating more accurate determination of ESS capacity and reduction of energy losses.

The current trend suggests that storage devices will become increasingly prevalent in grid systems as renewable energy becomes a more prominent component of the energy supply mix [56, 57]. The infrastructure of power systems utilizes ESSs at various stages. However, ESS technologies vary depending on their applications [57-59]. Despite the multidimensional application of ESS, it is essential to identify their applications and scopes in accordance with their technical specifications (such as power density, rating, energy density, lifetime, self-discharge rate, etc.) [60]. This sizing methodology relies on evaluating the energy balance between generation and demand over a defined sizing period to determine the optimal ESS capacity. The choice of the sizing period is flexible and can be tailored to meet user-specific requirements, ranging from a few days to several years. This sizing approach is versatile, catering to both independent and grid-connected energy systems. Moreover, it can be applied to resize ESS in existing systems when measured data is available, and it is adaptable for scenarios like peak shaving and grid-connected services. In the contemporary landscape of distributed energy resources, encompassing smart grids, microgrids,



energy communities, and leveraging advancements in information and communication technologies (ICT), this proposed methodology proves to be highly effective and user-friendly. Additionally, it incorporates the efficiency of energy storage in the sizing process, accounting for losses during the storage and release of energy, making the estimated ESS size more accurate, as illustrated in Figure 1.

In conclusion, this approach offers adaptability when choosing charge and discharge efficiency parameters, given that these parameters are contingent on the technology of the Energy Storage System (ESS). In practice, the charge and discharge efficiency values (represented as  $\eta_{in}$  and  $\eta_{out}$ ) are typically less than one and are subject to variation based on the specific ESS technology and the environmental conditions under which it operates. Reduced charge efficiency values are associated with an increase in the required ESS capacity.

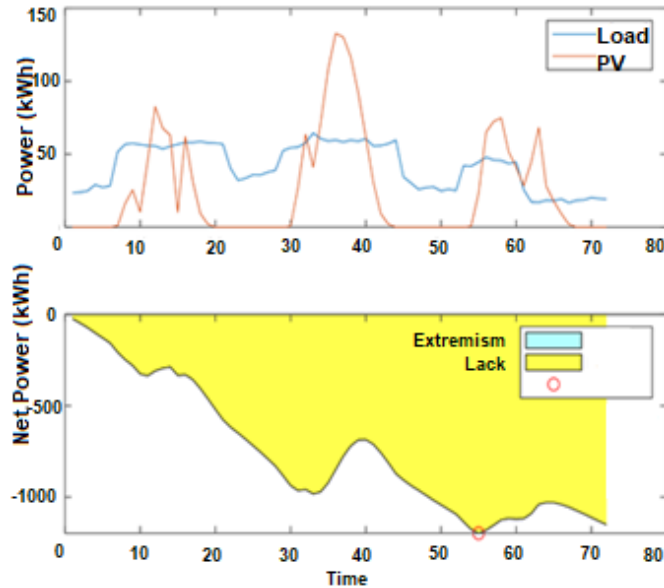


**Figure 1.** Sizing of an Independent PV System's EES

#### A. Smart Grids Power Balance with Voltage Control

In smart grid systems, inverters play a crucial role in maintaining voltage stability through various control functions. The volt-var control function allows inverters to respond to variations in Point of Common Coupling (PCC) voltage, either by supplying or absorbing reactive power. When an overvoltage condition occurs, the power control mechanism continuously monitors the voltage. It incrementally increases power generation to raise the voltage to an appropriate level. Conversely, if the PCC voltage exceeds the desired range, the inverter releases capacitive reactive power to lower the voltage.

Another essential control function, known as volt-watt control (VWC), focuses on managing active power output concerning voltage fluctuations. VWC utilizes measurements of the PCC voltage to make real-time adjustments. When the voltage surpasses the stable range, VWC intervenes to reduce the active power output, effectively lowering the voltage. VWC typically works in conjunction with volt-var control (VVC) to address overvoltage situations.

It's important to note that the primary method for stabilizing the distribution network's voltage is by controlling reactive power, particularly when employing VVC. The inverter autonomously adjusts the reactive power output based on the PCC voltage, following a predefined Q-V droop control curve. This method includes continuous measurement of the inverter's PCC voltage and reactive power control. Consequently, the DER's voltage stability relies on the generation of reactive power by the inverter. This iterative process leads to a stable operating point, ensuring a stable and reliable system operation.

*B. Flow Chart of the Recommended Algorithm in Scanned Optimization*

Reactive power control, guided by the VVC curve, is characterized by tracking the stable reactive power output. The final convergent voltage value is determined based on various system-specific parameters at the smart inverter's connection point. These parameters include Thevenin equivalent impedance, active power values, reactive power values, and other relevant factors. The proposed real-time active power control method within a smart grid is illustrated in Figure 2.

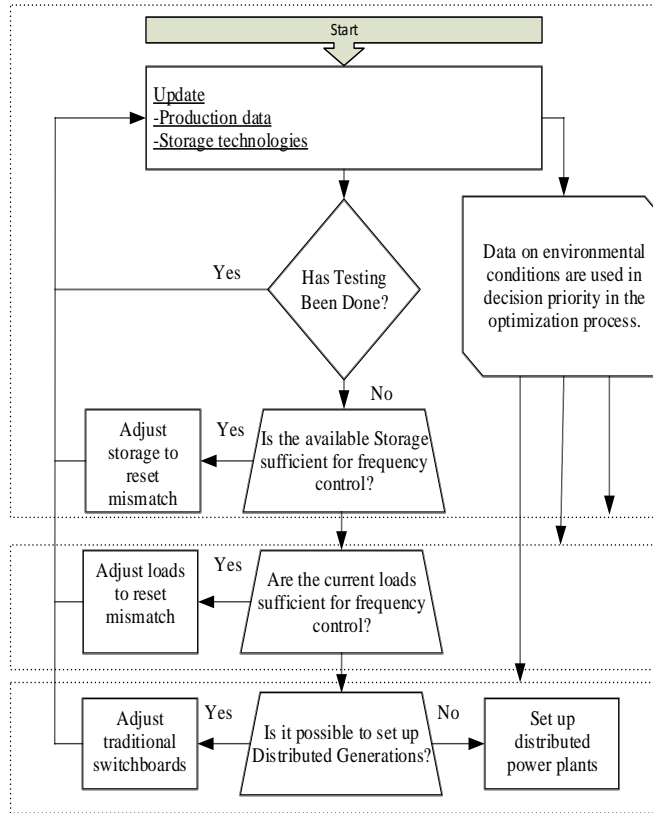


**Figure 2.** Flowchart of the Proposed Algorithm

A fundamental aspect of a smart grid is its robust communication and information infrastructure, enabling seamless data and information exchange among the grid components. Additionally, integrated sensors and data collection devices enhance the grid's situational awareness. Leveraging the smart grid's advantages, as outlined above, allows for effective real-time management of the active power generation-consumption mismatch, a capability not present in traditional power systems. [59].

In the proposed method, load data will be collected from the system through Advanced Metering Infrastructure (AMI). AMI enables two-way communication between consumers and suppliers. Real-time load data will be retrieved from the load data server. These real-time data may include the sizing of controllable loads such as electric vehicles, water heaters, dryers, etc., which can be used to adjust the system in case of discrepancies between supply and demand. It is assumed that consumers will release a portion of their loads for system regulation in response to incentives through demand response.

A secure and reliable communication system will be employed for data and command exchange between the operating system and AMI. One of the fundamental features of a smart grid is the presence of suitable communication and information infrastructure that facilitates data and information flow among the components of the smart grid. Additionally, sensors and data collection devices integrated into the system will make it more aware of various

conditions. As a result, leveraging the advantages of a smart grid mentioned above, it will be possible to manage the real-time mismatch between active power generation and consumption, which is not feasible in a traditional power system (Equations 1, 2, and 3)

$$P_{RTTP}(t) = \sum_{i=1}^n P_{RTTP}(t) + \sum_{j=1}^m P_{RTStorage}(t) + \sum_{k=1}^g P_{RTTP}(t) \quad (1)$$

$$P_{RTLload}(t) = \sum_{l=1}^f P_{RTCLoad}(t) + \sum_{r=1}^s P_{nonRTCLoad}(t) \quad (2)$$

$$\Delta P(t) = P_{RTTP}(t) - P_{RTLload}(t) - P_{lost} \quad (3)$$

$$DGP(t) = \Delta P(t) - DP(t) \quad (4)$$

$$DYP L(t) = \Delta P(t) - DP(t) - P_{DKY}(t) \quad (5)$$

$$DBSP(t) = \Delta P(t) - DSP(t) - P_{CLB}(t) - P_{SGB}(t) \quad (6)$$

In the proposed method, real-time total production (MW) is represented by  $P_{RTTP}(t)$ , real-time distributed production (MW) by  $P_{RTDP}(t)$ , real-time supplied power from storage to the grid (MW) by  $P_{RTStorage}$ , real-time total load (MW) by  $P_{RTLload}(t)$ , real-time controllable total load (MW) by  $P_{RTCLoad}(t)$ , real-time uncontrollable total load (MW) by  $P_{nonRTCLoad}(t)$ , total system loss in power (MW) by  $P_{lost}(t)$ , balancing share distributed by storage (MW) by  $DBSP(t)$ , stored power for balancing (MW) by  $DP(t)$ , controllable load set for balancing (MW) by  $P_{CLB}(t)$ , and smart grid production set for balancing (MW) by  $P_{SGB}(t)$ . In addition, the expressions  $n, m, k, f$  and  $s$  in the formulas are variables that indicate the unit types.

The utilization of distributed production resources, in addition to traditional production sources, can correct the imbalance of generated energy. The appropriateness of using distributed production sources alongside smart production sources can be examined (see the flowchart in Figure 2). The use of distributed production for regulation can be considered when the penetration level of distributed production resources is very high, and smart production resources are insufficient for system regulation. However, in such cases, distributed production sources are limited in their power capacity so that they can be used like traditional production sources. This, however, comes with the disadvantage of reducing the power generated from distributed production sources. After the real-time total production and load matching condition, the power value is calculated as shown in Equation (1). If the mismatch between supply and demand is within the allowed range, meaning that it doesn't affect the system's frequency and stability, the controller updates the data after the specified delay time (e.g., regular intervals for data updates are performed to prevent system ramping). If the mismatch between supply and demand is outside the allowed range, the controller must take action to correct the mismatch. Depending on the system, all available resources may be used to correct the mismatch, or only some resources may be used based on the magnitude of the mismatch. For example, following the sequence shown in the flowchart, existing storage systems are first used to absorb the mismatch power, followed by controllable loads, and finally, smart productions. If the load increases or production decreases, the balancing process is carried out as shown in Equations (4 to 6). If the existing storage resource is large enough to absorb the mismatch, the controller continues to update the data for the next step within the specified interval. Otherwise, storage transfers the remaining mismatch to controllable load or an appropriate resource, which has the ability to correct the mismatch.

This study demonstrates the critical importance of active power control strategies in integrating renewable energy sources into smart grids. These strategies play a pivotal role in managing the variability and intermittency inherent in renewable energy sources. By dynamically adjusting power generation and distribution, grid operators can ensure system stability and reliability, facilitating a smooth transition to a cleaner and more sustainable energy future. One

advantage of this approach is its ability to enhance the efficiency and stability of the grid. Additionally, it enables the mitigation of imbalances in the integration of renewable energy sources, contributing to the resilience and reliability of energy systems.

This paper study importance of smart grids and distributed energy systems, particularly in integrating renewable energy technologies. It highlights the benefits and challenges associated with distributed energy systems, emphasizing the role of ESS in mitigating the variability of renewable sources. The text also discusses methodologies for sizing ESS in independent PV systems, focusing on reliability metrics like Loss of Load Probability (LOLP). It underscores the increasing prevalence of energy storage in grid systems and the importance of efficient sizing methodologies. Furthermore, it delves into the role of inverters in maintaining voltage stability in smart grid systems through functions like volt-var control and volt-watt control. The proposed real-time active power control method within a smart grid is detailed, showcasing its ability to manage mismatches between supply and demand, thereby enhancing system stability and reliability. Overall, the text emphasizes the crucial role of active power control strategies in integrating renewable energy into smart grids for a sustainable energy future.

### III. ANALYSIS FINDINGS AND DISCUSSION

This thesis demonstrates that when smart grids, especially inherently intermittent renewable energy systems, are integrated into the power system, it makes the power system more efficient and stable. In a smart grid, it is possible to integrate renewable energy systems and control the system in real-time to overcome the imbalance between supply and demand. This requires access to data such as generators, loads, storage systems, energy markets, etc. In smart grids, this is possible due to the communication, information, and sensor infrastructure deployed throughout the electrical grid. This study will show that even when the ratio of renewable energy systems in the system is very high, the system's imbalance can be corrected. This method is crucial, especially when there are fewer synchronous machines in the network and the system's inertia is low. The order of choice for the controller in deciding whether to use storage, controllable loads, smart productions, or load shedding depends on factors such as available capacity, environmental data, market data, resource locations, etc.

#### B. Storage System Model Designed for Power Balance

The network seen in Figure 3 represents a part of the Electric Power Grid. In this model, an islanded (standalone) operation mode was adopted, and the testing of the proposed algorithm was conducted. Furthermore, energy storage systems and controllable loads were added to the system.

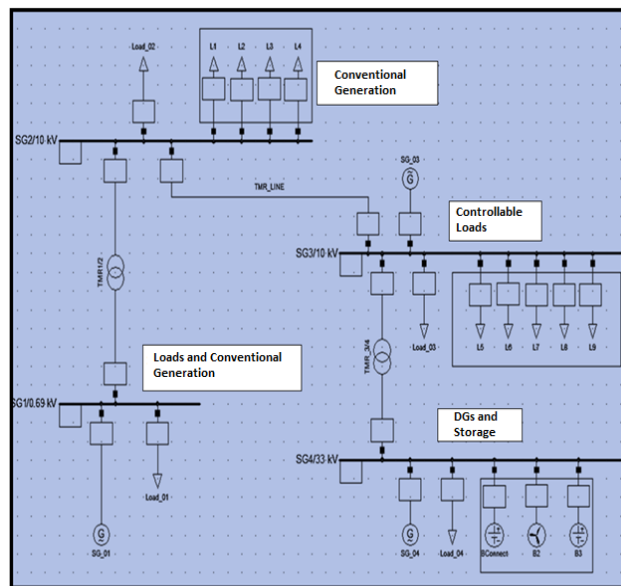
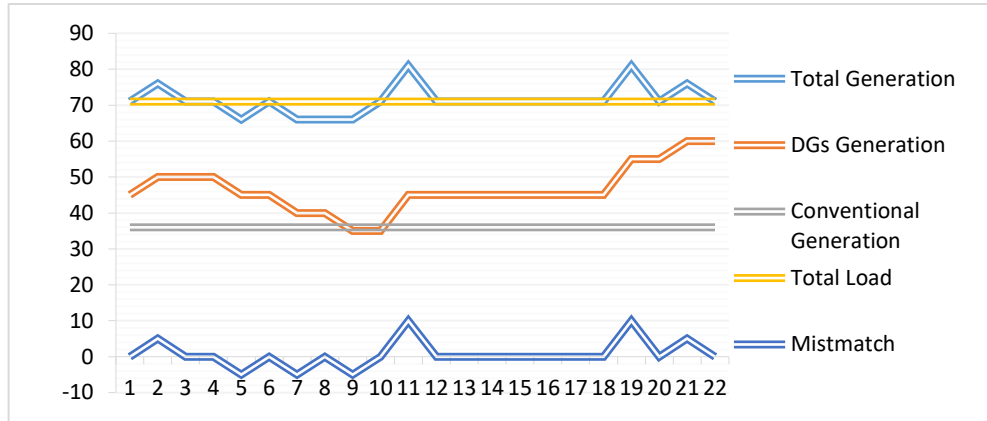


Figure 3. Model for Testing the Proposed Algorithm



The integration of these components was done to better understand the dynamics and imbalances of the network, as the original system did not have storage systems. This simulation addresses fluctuations caused by renewable energy sources (RE), but it is possible to consider load variability or a combination of both. The fluctuations from distributed energy resources (DER) are addressed, as shown in Figure 4.



**Figure 4.** Production from RES, Production from Conventional Power Plants, Total Production

Production from DERs (wind energy) ranges from 25 MW to 50 MW, while the load remains constant at 60 MW, and the power system's energy storage system capacity is set at 35 MW. Energy imbalances result from fluctuations in DERs and are illustrated in Figure 5.

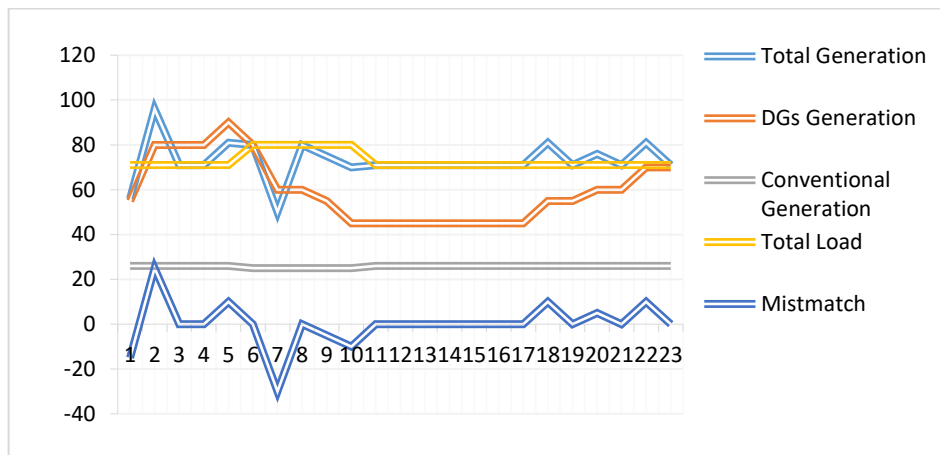


**Figure 5.** The storage system monitors fluctuations from RES and balances the mismatch.

Certainly, the system's controller functions automatically by constantly retrieving data from a network of strategically placed sensors distributed throughout the infrastructure. These sensors serve as the vital data sources that enable the controller to make informed real-time decisions. To make these decisions, the controller relies on a meticulously designed algorithm, which is visually represented in Figure 6. This algorithm plays a pivotal role in determining the most suitable and effective resource for addressing any prevailing imbalances within the system.

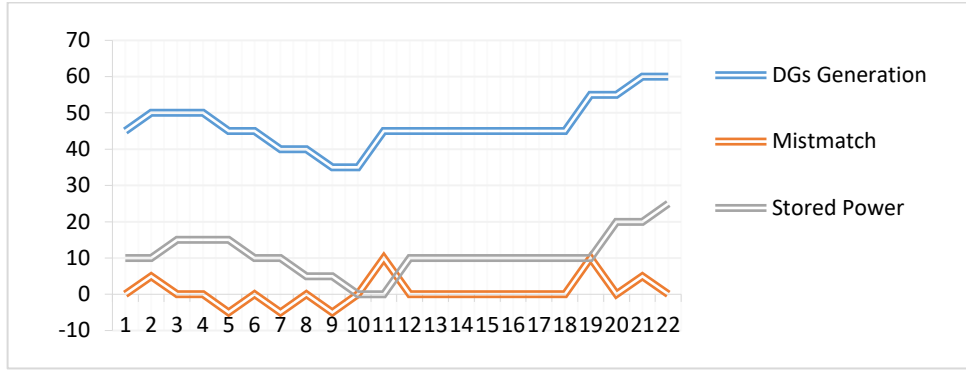


Figure 6. Production from DGs Generator, Mismatch and Stored Power

For instance, when the system boasts an ample capacity for energy storage, the algorithm swiftly triggers the activation of the storage system to counteract and rectify the detected imbalances. This mechanism ensures that the system remains stable and optimized to meet its energy demands. The controller automatically collects data through sensors placed at different points in the system and makes real-time decisions based on this data. An algorithm is used by the controller to select the most appropriate resource to address the imbalance. For instance, if suitable storage capacity is available, the algorithm defined in Figure 7. activates the storage system to address the imbalance.

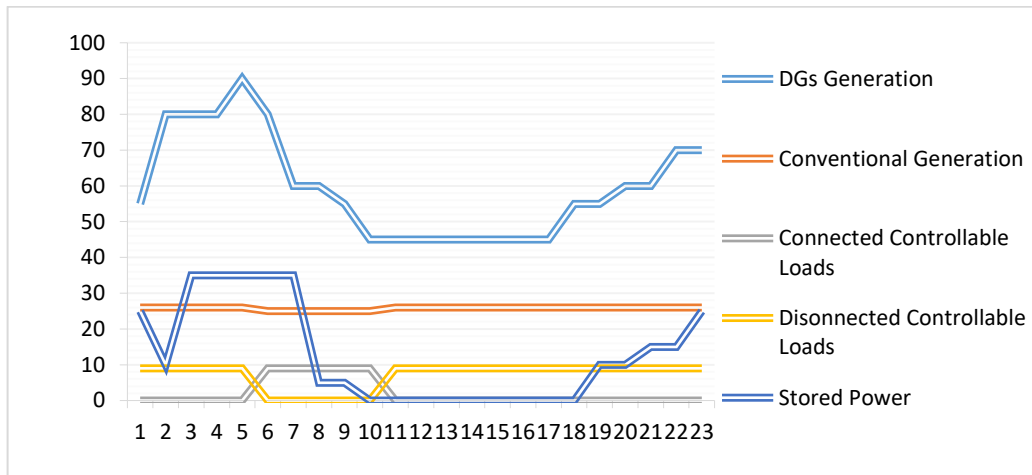


Figure 7. Storage, Controllable Load, and Smart Generation involved in adjusting the imbalance.

As seen in Figure 5, the energy storage system balances fluctuations by storing energy when there is excess production from RES and supplying energy to the grid when RES production decreases. Similarly, as shown in Figure 6, RES production varies between 25 MW and 60 MW, while the energy storage capacity remains at 15 MW, and the total capacity allocated to controllable loads to address the mismatch is 6 MW. In this scenario, the imbalance is addressed solely by the energy storage system. If the energy storage source is either full or empty, the controller searches for loads in the load data server that are allocated for use by the controller (these loads could be related to demand response or loads that customers allocate based on their intensity, such as electric vehicle charging or discharging). In this situation, neither energy storage nor controllable loads can address the imbalance, and as a result, the controller activates smart generation systems to further stabilize the system. Figure 7 illustrates the use of controllable loads and smart generation resources in addition to the energy storage source to address the imbalance.

#### IV. RESULTS AND RECOMMENDATIONS

In conclusion, the successful integration of renewable energy power plants into smart grids hinges on the implementation of active power control strategies. These strategies play a pivotal role in enabling grid operators to effectively manage the inherent variability and intermittency of renewable energy sources. By actively adjusting

power generation and distribution in real-time, grid operators can maintain grid stability and reliability, ensuring a seamless transition to a cleaner and more sustainable energy future.

In conclusion, this research demonstrates that a smart grid, especially when integrated with intermittent renewable energy systems, can make the power system more efficient and stable. In a smart grid, it is possible to integrate renewable energy systems and control the imbalance between supply and demand in real-time. This requires access to data obtained from generation, loads, storage systems, energy markets, and more. This data access is made possible through the communication, information, and sensor infrastructure embedded within the smart grid. This study shows that the imbalance in the system can be addressed, even when the proportion of Renewable Energy Sources in the system is very high. This method is particularly important when there are fewer synchronous machines in the network, and the system has low inertia. The selection order of the controller methods, such as energy storage systems, controllable loads, smart generators, or load shedding, depends on factors like available capacity, environmental data, market data, the location of resources, and more. Achieving an efficient and effective solution requires optimization. Ongoing research in this direction aims to further refine these methods and explore the optimal strategies for managing imbalances within the grid.

In conclusion, this research demonstrates that in smart grids, especially when integrating intermittent renewable energy systems, the power system can become more efficient and stable. In smart grids, it is possible to integrate renewable energy systems and control the imbalance between supply and demand in real-time. This requires access to data obtained from productions, loads, storage systems, energy markets, and more. This data access can be achieved through the communication, information, and sensor infrastructure embedded in the smart grid. This study shows that the system's imbalance can be addressed even when the ratio of RES within the system is very high. The proposed method is particularly important in cases where there are fewer synchronous machines in the network and low system inertia. The method can also be applied to balance supply and demand in cases of load variation or other contingencies. The selection order of controller methods, such as storage systems, controllable loads, smart generation systems, or load shedding, depends on factors like available capacity, environmental data, market data, resource locations, and more. Optimization is required to achieve a suitable and efficient solution. Ongoing research is focusing on further exploring this area. Future research in the field of "Integration of Renewable Energy Power Plants into Smart Grids, Active Power Control" should explore advanced control algorithms and technologies that enhance the accuracy and responsiveness of active power control systems.

#### CONFLICTS OF INTEREST

They reported that there was no conflict of interest between the authors and their respective institutions.

#### RESEARCH AND PUBLICATION ETHICS

In the studies carried out within the scope of this article, the rules of research and publication ethics were followed.

#### REFERENCES

- [1] G. 9th Basic Plan for Electricity Supply and Demand,(BPLE), 2020, Biennial Repor Republic of Korea Ministry of Trade, Industry, and Energy. t; Republic of Korea Ministry of Trade, Industry, and Energy: Sejong-si, Korea
- [2] Holguin, J.P.,2020, Rodriguez, D.C.; Ramos, G. Reverse Power Flow (RPF) Detection and Impact on Protection Coordination of Distribution Systems. *IEEE Trans. Ind. Appl.* 56, 2393–2401
- [3] Hossain, E., Tür, M. R., Padmanaban, S., Ay, S., & Khan, I. ,2018, Analysis and mitigation of power quality issues in distributed generation systems using custom power devices. *Ieee Access*, 6, 16816-16833.
- [4] K. Moslehi, R. Kumar, A reliability perspective of the smart grid, *IEEE Trans. Smart Grid* 1 (1) (2010) 57–64.
- [5] N. Phuangpornpitak, S. Tia, Opportunities and challenges of integrating renewable energy in smart grid system, *Energy Procedia* 34 (2013) 282–290.
- [6] P. Capros, N. Tassios, A. De Vita, L. Mantzos, L. Paroussos, Transformations of the energy system in the context of the decarbonisation of the EU economy in the time horizon to 2050, *Energy Strategy Rev.* 1 (2) (2012) 85–96.
- [7] M. Ali, K. Prakash, M.A. Hossain, H.R. Pota, Intelligent energy management: Evolving developments, current challenges, and research directions for sustainable future, *J. Clean. Prod.* 314 (2021) 127904.
- [8] K. Khan, A. Rauf, M. Khalid, Economic dispatch for conventional generationreplacement with solar PV and battery storage using robust stochastic optimization, in: 2023 International Conference on Control, Automation and Diagnosis, ICCAD, IEEE, 2023, pp. 1–6.

- [9] T. Han, K. Muhammad, T. Hussain, J. Lloret, S.W. Baik, An efficient deep learning framework for intelligent energy management in IoT networks, *IEEE Internet Things J.* 8 (5) (2020) 3170–3179.
- [10] M.A. Abdulgalil, M. Ali, M. Khalid, Capacity optimization of battery energy storage system for large-scale grid integration of renewables, in: 2023 International Conference on Control, Automation and Diagnosis, ICCAD, IEEE, 2023, pp. 1–6.
- [11] Alvi, W. Ahmed, M. Rehan, S. Ahmed, R. Ahmad, I. Ahmed, A novel incremental cost consensus approach for distributed economic dispatch over directed communication topologies in a smart grid, *Soft Comput.* 26 (14) (2022) 6685–6700.
- [12] M. Faheem, S.B.H. Shah, R.A. Butt, B. Raza, M. Anwar, M.W. Ashraf, M.A. Ngadi, V.C. Gungor, Smart grid communication and information technologies in the perspective of Industry 4.0: Opportunities and challenges, *Comp. Sci. Rev.* 30 (2018) 1–30.
- [13] W. Ketter, J. Collins, M. Saar-Tsechansky, O. Marom, Information systems for a smart electricity grid: Emerging challenges and opportunities, *ACM Trans. Manag. Inf. Syst. (TMIS)* 9 (3) (2018) 1–22.
- [14] K.A. Khan, M.M. Quamar, F.H. Al-Qahtani, M. Asif, M. Alqahtani, M. Khalid, Smart grid infrastructure and renewable energy deployment: A conceptual review of Saudi Arabia, *Energy Strategy Rev.* 50 (2023) 101247.
- [15] S. Aziz, I. Ahmed, K. Khan, M. Khalid, Emerging trends and approaches for designing net-zero low-carbon integrated energy networks: A review of current practices, *Arab. J. Sci. Eng.* (2023) 1–23.
- [16] C. Milchram, G. Van de Kaa, N. Doorn, R. Künneke, Moral values as factors for social acceptance of smart grid technologies, *Sustainability* 10 (8) (2018) 2703.
- [17] M.A. Raza, M.M. Aman, A.G. Abro, M.A. Tunio, K.L. Khatri, M. Shahid, Challenges and potentials of implementing a smart grid for Pakistan’s electric network, *Energy Strategy Rev.* 43 (2022) 100941.
- [18] I. Ahmed, M. Rehan, A. Basit, K.-S. Hong, Greenhouse gases emission reduction for electric power generation sector by efficient dispatching of thermal plants integrated with renewable systems, *Sci. Rep.* 12 (1) (2022) 12380.
- [19] M.L. Tuballa, M.L. Abundo, A review of the development of smart grid technologies, *Renew. Sustain. Energy Rev.* 59 (2016) 710–725.
- [20] M. Ali, A. Iqbal, M. Khalid, A review on recent advances in matrix converter technology: Topologies, control, applications, and future prospects, *Int. J. Energy Res.* 2023 (2023).
- [21] M.A. Brown, S. Zhou, Smart-grid policies: An international review, *Adv. Energy Syst. Large-scale Renew. Energy Integr. Chall.* (2019) 127–147.
- [22] C. Tu, X. He, Z. Shuai, F. Jiang, Big data issues in smart grid—A review, *Renew. Sustain. Energy Rev.* 79 (2017) 1099–1107.
- [23] O. Babayomi, Z. Zhang, T. Dragicevic, J. Hu, J. Rodriguez, Smart grid evolution: Predictive control of distributed energy resources—A review, *Int. J. Electr. Power Energy Syst.* 147 (2023) 108812.
- [24] K.H. Kabir, S.Y. Aurko, M.S. Rahman, Smart power management in OIC countries: A critical overview using SWOT-AHP and hybrid MCDM analysis, *Energies* 14 (20) (2021) 6480.
- [25] Z. Abdmouleh, A. Gastli, L. Ben-Brahim, Survey about public perception regarding smart grid, energy efficiency & renewable energies applications in Qatar, *Renew. Sustain. Energy Rev.* 82 (2018) 168–175.
- [26] I. Ahmed, A. Basit, F. e Mustafa, M. Alqahtani, M. Khalid, The nexus of energy in microgrids: A review on communication barriers in distributed networks auxiliary controls, *IET Gener. Transm. Distr.* (2023).
- [27] A.Q. Khan, A. Samee, I. Ahmed, M. Abid, M. Alqahtani, M. Khalid, et al., Advanced statistical and meta-heuristic based optimization fault diagnosis techniques in complex industrial processes: a comparative analysis, *IEEE Access* (2023).
- [28] Muhammad K, Smart grids and renewable energy systems: Perspectives and grid integration challenges, *Energy Strategy Reviews*, vol 51, 2024, 101299, ISSN 2211-467X
- [29] IEA, 2017, Plan for Implementation of Renewable Energy 3020, South Korea Ministry of Trade, Industry and Energy
- [30] V. Vita, L. Ekonomou, C.A. Christodoulou, The impact of distributed generation to the lightning protection of modern distribution lines, *Energy Syst.* 7 (2016) 357–364.
- [31] O.B. Adewumi, G. Fotis, V. Vita, D. Nankoo, L. Ekonomou, The impact of distributed energy storage on distribution and transmission networks’ power quality, *Appl. Sci.* 12 (13) (2022) 6466.
- [32] E. Zafropoulos, C. Christodoulou, V. Vita, C. Dikaiakos, I. Gonos, E. Zubieta, G. Santamaria, N. Lai, N. Baltas, P. Rodriguez, Smart grid flexibility solutions for transmission networks with increased RES penetration, in: Proceedings of the CIGRE Paris Session, 2022, p. 10711.
- [33] I. Ahmed, M. Rehan, N. Iqbal, C.K. Ahn, A novel event-triggered consensus approach for generic linear multi-agents under heterogeneous sector-restricted input nonlinearities, *IEEE Trans. Netw. Sci. Eng.* (2023).
- [34] I. Ahmed, M. Rehan, K.-S. Hong, A. Basit, A consensus-based approach for economic dispatch considering multiple fueling strategy of electricity production sector over a smart grid, in: 2022 13th Asian Control Conference, ASCC, IEEE, 2022, pp. 1196–1201.
- [35] U. Salman, K. Khan, F. Alismail, M. Khalid, Techno-economic assessment and operational planning of wind-battery distributed renewable generation system, *Sustainability* 13 (12) (2021) 6776.

- [36] IEEE, "IEEE Standard for Interconnecting Distributed Resources with Electric Power Systems", (2001).
- [37] Zhao, C.; Yin, H.; Ma, C. Quantitative efficiency and temperature analysis of battery-ultracapacitor hybrid energy storage systems. *IEEE Trans. Sustain. Energy* 2016, 7, 1791–1802.
- [38] Gatta, F.M.; Geri, A.; Lauria, S.; Maccioni, M.; Palone, F. Battery energy storage efficiency calculation including auxiliary losses: Technology comparison and operating strategies. In *Proceedings of the 2015 IEEE Eindhoven PowerTech*, Eindhoven, The Netherlands, 29 June–2 July 2015.
- [39] Patil, V.C.; Ro, P.I.; Kishore Ranganath, R. End-to-end efficiency of liquid piston based ocean compressed air energy storage. In *Proceedings of the OCEANS 2016 MTS/IEEE Monterey*, Monterey, CA, USA, 19–23 September 2016.
- [40] Funaki, T. Evaluating energy storage efficiency by modeling the voltage and temperature dependency in EDLC electrical characteristics. *IEEE Trans. Power Electron.* 2010, 25, 1231–1239.
- [41] Torres, J.; Moreno-Torres, P.; Navarro, G.; Blanco, M.; Lafoz, M. Fast energy storage systems comparison in terms of energy efficiency for a specific application. *IEEE Access* 2018, 6, 40656–40672.
- [42] Tan, Z., Liu, B., & Wu, A., 2022, Artificial Intelligence and Feature Identification Based Global Perception of Power Consumer: Definition, Structure, and Applications. *Frontiers in Energy Research*.
- [43] Tur M.R., Wadi M, A. Shobole and S. Ay, 2018, Load Frequency Control of Two Area Interconnected Power System Using Fuzzy Logic Control and PID Controller, 2018 7th International Conference on Renewable Energy Research and Applications (ICRERA), Paris, France, 2018, pp. 1253-1258
- [44] Mitra J, 2010, Reliability-based sizing of backup storage, in: *IEEE Transactions on Power Systems* 25, pp. 1198–1199
- [45] Shobole, A., Wadi, M., Tür, M. R., & Baysal, M. ,2017, Real time active power control in smart grid, In 2017 IEEE 6th International Conference on Renewable Energy Research and Applications (ICRERA) (pp. 585-590). IEEE
- [46] Tur, M. R., Mohammed, W., SHOBOLE, A. A., & Gündüz, H. ,2021, Integration problems of photovoltaic systems-wind power, solutions and effects on power quality. *European Journal of Technique (EJT)*, 10(2), 340-353
- [47] Moghaddam Z., I. Ahmad, D. Habibi, M.A.S. Masoum, 2019, A coordinated dynamic pricing model for electric vehicle charging stations, in: *IEEE Transactions on Transportation Electrification* 5, March , pp. 226–238
- [48] Das C.K., O. Bass, G. Kothapalli, T.S. Mahmoud, D. Habibi, 2018, Overview of energy storage systems in distribution networks–Placement, sizing, operation, and power quality, *Renew. Sustain. Energy Rev.* 91, 1205–1230.
- [49] Kichou S., Skandalos N, Wolf P., 2020, Evaluation of photovoltaic and battery storage effects on the load matching indicators based on real monitored data, *Energies* 13, 2727
- [50] M. Aneke, M. Wang, Energy storage technologies and real life applications–A state of the art review, *Appl. Energy* 179 (2016) 350–377.
- [51] K. Moslehi, R. Kumar, A reliability perspective of the smart grid, *IEEE Trans. Smart Grid* 1 (1) (2010) 57–64.
- [52] H.M. Ghazal, K.A. Khan, F. Alismail, M. Khalid, Maximizing capacity credit in generation expansion planning for wind power generation and compressed air energy storage system, in: 2021 IEEE PES Innovative Smart Grid Technologies Europe, ISGT Europe, IEEE, 2021, pp. 1–5.
- [53] Y. Alhumaid, K. Khan, F. Alismail, M. Khalid, Multi-input nonlinear programming based deterministic optimization framework for evaluating microgrids with optimal renewable-storage energy mix, *Sustainability* 13 (11) (2021) 5878.
- [54] R. Tiskatine, A. Aharoune, L. Bouirden, A. Ihlal, Identification of suitable storage materials for solar thermal power plant using selection methodology, *Appl. Therm. Eng.* 117 (2017) 591–608.
- [55] F. Mohamad, J. Teh, Impacts of energy storage system on power system reliability: A systematic review, *Energies* 11 (7) (2018) 1749.
- [56] M. Khalid, A review on the selected applications of battery-supercapacitor hybrid energy storage systems for microgrids, *Energies* 12 (23) (2019) 4559.
- [57] Y.M. Al-Humaid, K.A. Khan, M.A. Abdulgalil, M. Khalid, Two-stage stochastic optimization of sodium-sulfur energy storage technology in hybrid renewable power systems, *IEEE Access* 9 (2021) 162962–162972
- [58] M. N. Tur, ö. F. Ertuğrul and M. R. Tur, "Comparison of Energy Storage Technologies in Smart Grids, Implementation Challenges of Vanadium Technique," 2022 Global Energy Conference (GEC), Batman, Turkey, 2022, pp. 395-401, doi: 10.1109/GEC55014.2022.9987133.
- [59] Tur, M. R., & Bayindir, R. (2020, July). Comparison of Power Quality Distortion Types and Methods Used in Classification. In 2020 International Conference on Computational Intelligence for Smart Power System and Sustainable Energy (CISPSSSE) (pp. 1-7). IEEE.Hadj Arab A., B. Ait Driss, R. Amimeur, E. Lorenzo, 1995, Photovoltaic systems sizing for Algeria, *Sol. Energy* 54 (2) , 99–104
- [60] Tur, M. R. ,2020, Reliability assessment of distribution power system when considering energy storage configuration technique. *IEEE Access*, 8, 77962-77971





## RESEARCH ARTICLE

# Investigation of the effect of asphalt and sub-base layer thicknesses on pavement surface deformation by the finite element method

Mehmet Bayazit<sup>1</sup> , Ferhat Şahinkaya\* 

<sup>1</sup>Yozgat Bozok University, Faculty of Engineering-Architecture, Department of Civil Engineering, Yozgat, Turkey  
[mehmet.bayazit@yobu.edu.tr](mailto:mehmet.bayazit@yobu.edu.tr), [Orcid.0000-0003-2459-132X](https://orcid.org/0000-0003-2459-132X)

\*Yozgat Bozok University, Faculty of Engineering-Architecture, Department of Civil Engineering, Yozgat, Turkey  
[ferhat.sahinkaya@yobu.edu.tr](mailto:ferhat.sahinkaya@yobu.edu.tr), [Orcid.0000-0002-5534-7058](https://orcid.org/0000-0002-5534-7058)

## Citation:

Bayazit, M., Şahinkaya, F. (2024). *Investigation of the effect of asphalt layer and sub-base layer thicknesses on pavement surface deformation by the finite element method*, Journal of Science Technology and Engineering Research, 5(1):24-33. DOI:10.53525/jster.1452916

## HIGHLIGHTS

- Effect and importance of size of loading affects surface permanent deformation.
- Sub-base should be added rather than increasing the asphalt concrete layer.
- Finite element analysis can perform analyses that cannot be done experimentally.
- The study results are important for understanding how layer thicknesses impact the deformation.

## Article Info

Received : 15 March 2024

Accepted : 04 May 2024

## DOI:

10.53525/jster.1452916

## \*Corresponding Author:

Ferhat Şahinkaya

[ferhat.sahinkaya@yobu.edu.tr](mailto:ferhat.sahinkaya@yobu.edu.tr)

## ABSTRACT

The layer thickness of flexible pavements is one of the important parameters affecting permanent deformations. In this study, the effect of sub-base thickness and asphalt concrete thickness on the deformations under axial loads was investigated using the Plaxis 2D finite element software. In the study, 100, 200, 300, 400, 500, and 600 kPa pressure were applied to the asphalt pavement surface. In the first case, the base layer of 30 cm thickness was kept constant, and the asphalt layer was changed from 9 to 14 cm. In the second case, the asphalt layer thickness was selected at 30, 40, and 50 cm respectively. As a result of the completed analysis, it was observed that the deformations on the pavement surface decreased with increasing thickness of the layers; furthermore, the use of a sub-base layer in the pavement considerably increases the deformation resistance.

**Keywords:** Finite element analysis, Pavement, Asphalt, Layer thickness, Sub-base

## I. INTRODUCTION

Flexible pavement is the most widely used road paving material in the world. It is a layered structure of different granular materials. It is important that the pavement provide a safe surface for passengers and vehicles without deforming under traffic loads. The permanent deformation resulting from the traffic loads is an important parameter affecting the service life of the pavement. In addition to the stability of the asphalt concrete; the layer thicknesses, the quality of the material, and the application experience affect the durability of the flexible pavement. The properties of the materials used in the flexible pavement can be determined by experimental methods. However, it is not possible experimentally to investigate the deformations that will occur on the pavement surface under the effect of different material properties, layer thicknesses, and loads. One of the analytical and modeling techniques for various types of structures is the finite element method (FEM). This method is suitable for analyzing the deformation of the pavement surface under different boundary conditions, different material properties, different layer thicknesses, and different loads. [1].

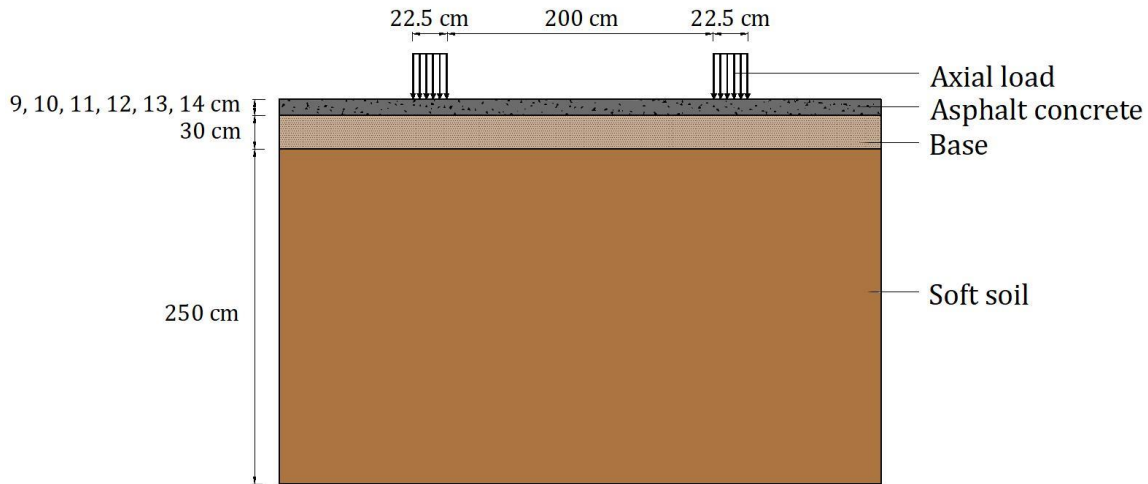
Asphalt concrete has plastic, viscous, and elastic qualities all at once and all of which are significant, particularly when the temperature is high. The use of an elastic model appears inadequate in accurately characterizing the actual behavior of asphalt concrete under high temperatures. Due to this, many researchers employ various rheological models, such as viscoelastic models [2]. In order to estimate the pavement's thermal behavior, ANSYS source code was employed, and the proposed simulation model accurately predicts the pavement temperature at various levels of bituminous layers [3]. Asphalt concrete is also thought to resemble soil because it is composed of air, water, and aggregate. [4, 5]. Thus, asphalt concrete can be modelled as a Mohr-Coulomb material with both cohesive and granular properties at intermediate temperatures [5, 6]. However, linear elastic model is frequently employed for the mechanistic analysis and modelling of asphalt pavement structures. The behavior of asphalt layers at lower temperatures can be accurately determined using this method [2]. Some completed studies used a linear elastic model to represent asphalt concrete [1, 7-9].

In order to evaluate the stresses and deformation on the pavement surface, several numerical studies have been conducted [1]. In the study in which rutting deformation was determined, the axisymmetric two-dimensional finite element approach with varying layer thicknesses and material parameters was used. The results showed that increasing the base layer's thickness and elastic modulus reduced rutting damage but had little effect on fatigue damage. Additionally, the researchers emphasised that the analysis was beneficial for designing a pavement, as it ensures a balance between fatigue and rutting life. [10]. The semi-analytical finite element method (SAFEM program) was utilized to analyze the effects of high traffic loads on stress and strain distribution, surface deformation, and fatigue life. The findings suggested that in order to resist surface deformation, it was necessary to adequately increase the thickness and stiffness of the structural layers of the asphalt pavement when exposed to high levels of traffic. Furthermore, compared to the other pavement layers, the compressive stress on the asphalt binder surface was relatively large and increased more significantly when the axle load was applied. [11]. Wheels and axles of heavy vehicles configurations were modelled in 3D with the finite element (Ls-Dyna) method and dynamic analysis was performed. The study determined that wheels with large contact areas and a single design were the most harmful in terms of causing rutting damage and fatigue cracks. [12]. The Plaxis 3D program was utilized to examine the performance of asphalt concrete pavement without reinforcement and with geogrid reinforcement under different tire pressures. The model was loaded incrementally from 100 to 600 kPa at 50 kPa increments, and critical pavement responses such as total stress and vertical surface deformation were calculated. The study showed that the influence of the geogrid placement at the base of the asphalt concrete surface layer on pavement response was evident during static loading. [8]. The effect of geogrids on the axial stiffness of the pavement in base layers of different thicknesses was investigated using Plaxis 2D software. The base, sub-base, and subgrade layers were modeled with the Mohr-Coulomb model. The study was found that the vertical surface deformations in flexible pavement reinforced with geogrids were less than those in unreinforced flexible pavements. Also, vertical surface deformation was approximately constant when base layer thickness varied from 150 to 200 mm. [1].

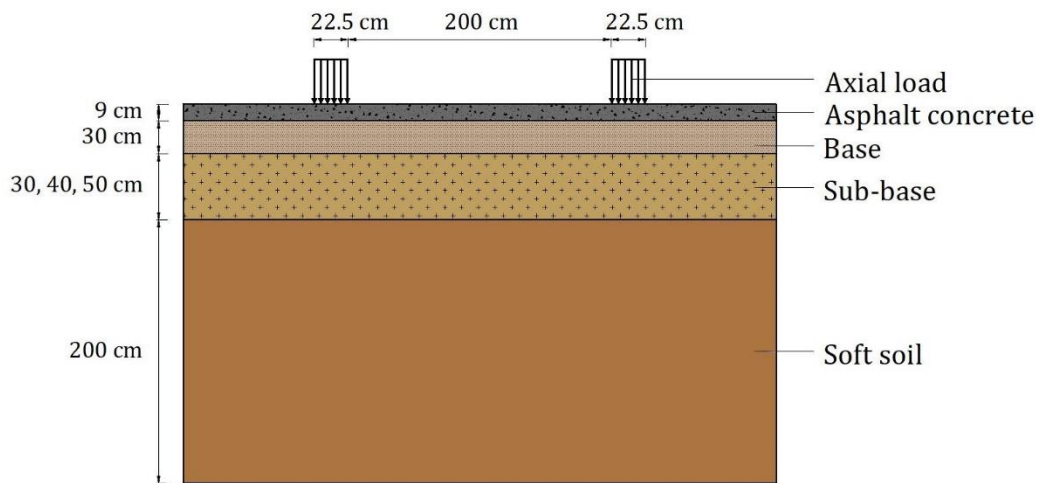
The studies have indicated that improving material properties, increasing layer thicknesses, or using geogrid in the layers decreased surface deformation of asphalt pavement. In this study, PLAXIS 2D software was used to do finite element modeling of pavement layer thickness and the deformation of the pavement surface was trying to be determined. Also, the asphalt layer was modelled as linear elastic and the temperature effect was not investigated in the study since the linear elastic model better modelled the asphalt at low temperatures [2].

## II. METHOD

For flexible pavement design, a three-layer section consisting of asphalt concrete, base layer, and sub-base layer was chosen. The Plaxis 2D software was utilized to analyze the impact of varying asphalt concrete and sub-base thicknesses on the deformation of the pavement surface under varied levels of axial load. The layers forming of the pavement were selected in two different ways. In the first case, as seen in Figure 1, without sub-base layer, while in the second case, as seen in Figure 2, the sub-base layer was used. In the without sub-base model, the asphalt concrete layer thicknesses were modeled in incremental thicknesses ranging from 9 to 14 cm. In the model using sub-base, the asphalt concrete thickness (ACT) was kept constant at 9 cm, and the sub-base thicknesses (SBT) were modeled separately at 30, 40, and 50 cm. The base layer thickness was selected as 30 cm in both models. Throughout the entire model, the ground layer was selected to consist of soft soil. The models were created separately for each layer thickness in the Plaxis 2D software, and the load was applied to the pavement surface. The pressure of the dual-type tires was applied statically on the pavement. A range of 100–600 kPa was used for the applied pressures [9]. An plane strain model was utilized in the analysis using 15-noded structural solid element with fine refinement. The study employed plane strain modelling to accurately simulate the load exerted by vehicle tyres on the pavement surface. Analyses were performed under similar loading conditions using the plain strain model in the literature. [7]



**Figure 1.** Thickness of layers in pavement without sub-base (ACT range 9-14 cm, Base =30 cm)



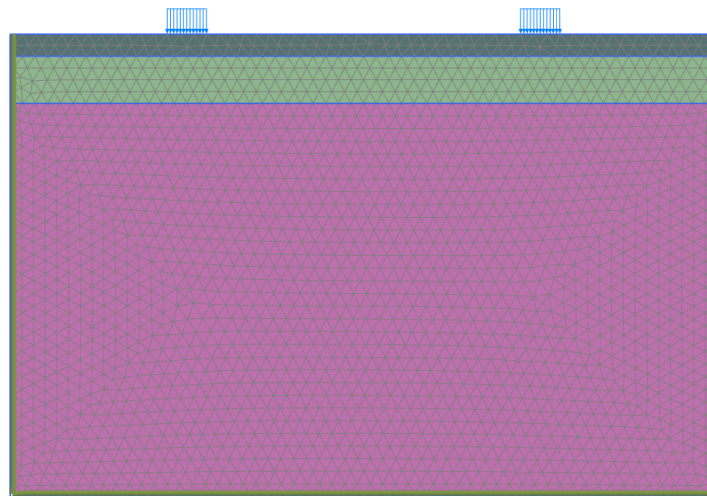
**Figure 2.** Thickness of layers in pavement with sub-base at 30, 40, and 50 cm (ACT=9 cm, Base=30 cm)

Table 1 lists the material properties utilized in the analysis model, which were chosen based on the completed studies [7, 9].

**Table 1. Material properties of pavement layers**

Material	Surface Course (Asphalt concrete)	Base Course (Crushed aggregate)	Sub-base (Clay)	Soft Soil (Clay)
Type of Model	Linear elastic	Mohr-Coulomb	Mohr-Coulomb	Mohr-Coulomb
Mesh type	Fine	Fine	Fine	Fine
Layer Thickness (cm)	Without sub-base (in the first case)  Added sub-base layer (in the second case)	9, 10, 11, 12, 13, 14  30	-  30, 40, 50	250  200
Dry unit weight (kN/m <sup>3</sup> )	24	22.1	14.5	16.0
Saturated unit weight (kN/m <sup>3</sup> )	-	23.6	15.5	17.5
Cohesion (kN/m <sup>2</sup> )	-	1	10	10
Angle of internal friction( $\phi^\circ$ )	-	45	5	1
Elastic Modulus (MPa)	1000	20	10	3
Poisson's ratio ( $\mu$ )	0.35	0.35	0.35	0.20
Drainage Type	Undrained A	Undrained A	Undrained A	Undrained A

The models' material properties were then applied, and the mesh was assembled. The model's mesh definition without a sub-base is shown in Figure 3, while the model's mesh definition with a sub-base is shown in Figure 4.



**Figure 3. Mesh model of pavement without sub-base (ACT = 9 cm, Base=30 cm)**

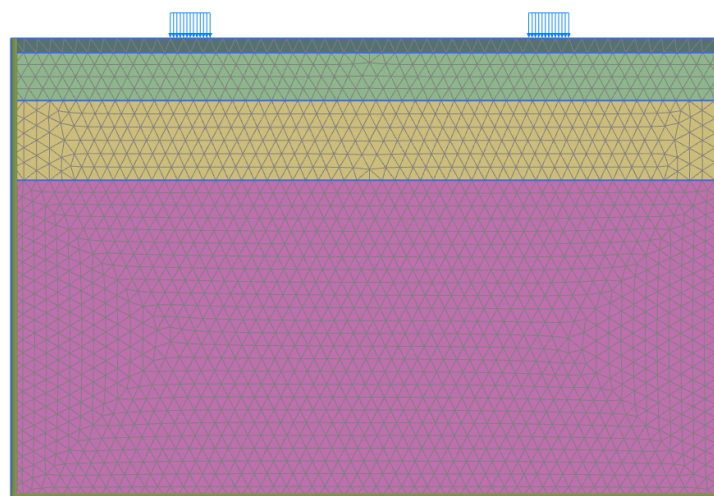
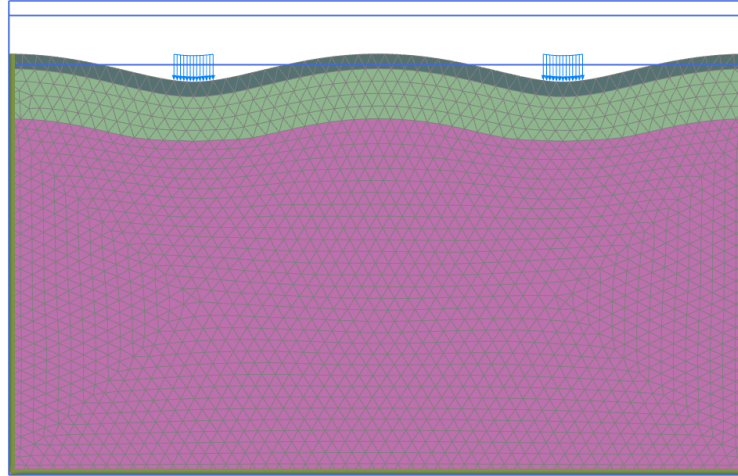


**Figure 4. Mesh model of pavement with sub-base**

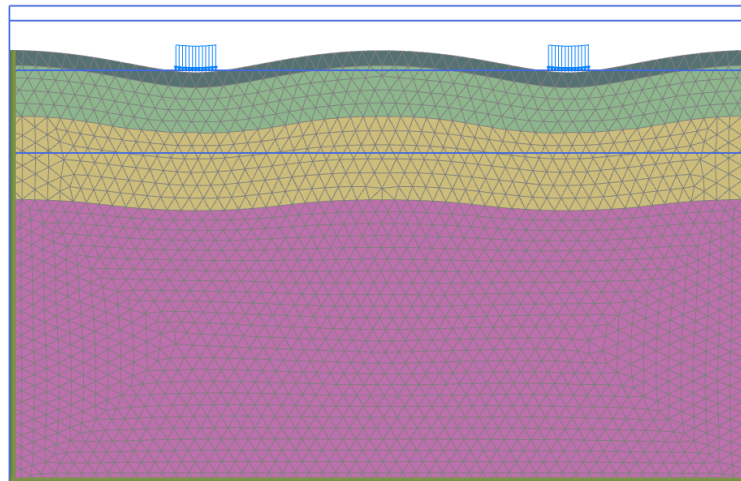


### III. RESULTS

The analysis was conducted on each pavement model and loading condition (ranging from 100 to 600 kPa) separately. The total vertical displacement of pavements with and without sub-base is determined for each static loading value. At the end of the analysis, the deformation of the pavement layers without a sub-base under a load of 600 kPa is shown in Figure 5. Similarly, the deformation of the pavement layers with a sub-base thickness of 30 cm is shown in Figure 6.



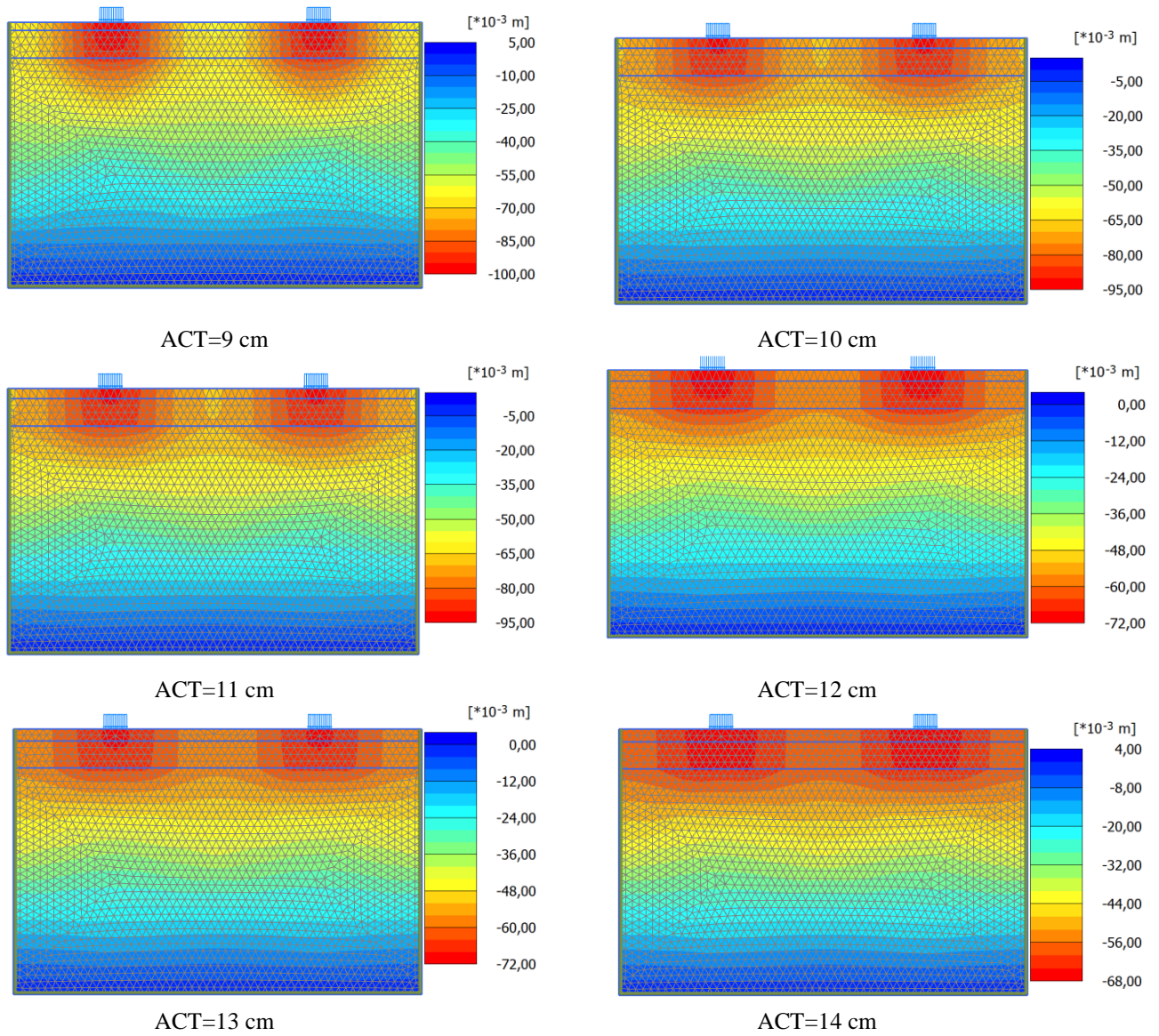
**Figure 5.** Deformation of pavement layers without sub-base layers (ACT=9 cm, Base=30 cm; Pressure=600 kPa)



**Figure 6.** Deformation of pavement layers with sub-base at 30cm layers (ACT=9 cm; Pressure=600 kPa)

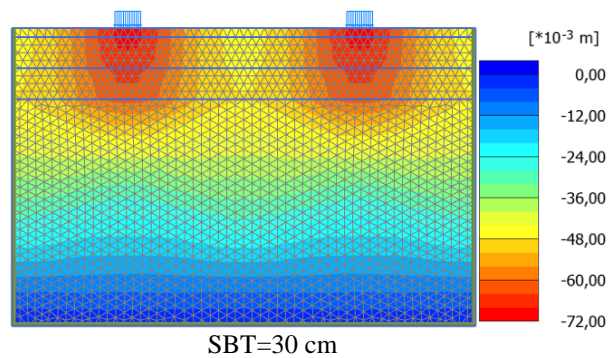
The vertical displacement contour diagrams of pavements modeled without sub-base according to asphalt concrete thicknesses (ACT) ranging from 9 cm to 14 cm applied to a 600 kPa load are given in Figure 7.





**Figure 7.** Vertical displacement contour diagram(y) of pavement without sub-base (Pressure=600 kPa)

The vertical displacement contour diagrams of pavements (ACT=9 cm) modeled with sub-base at 30, 40, and 50 cm SBT applied to a 600 kPa load are given in Figure 8.



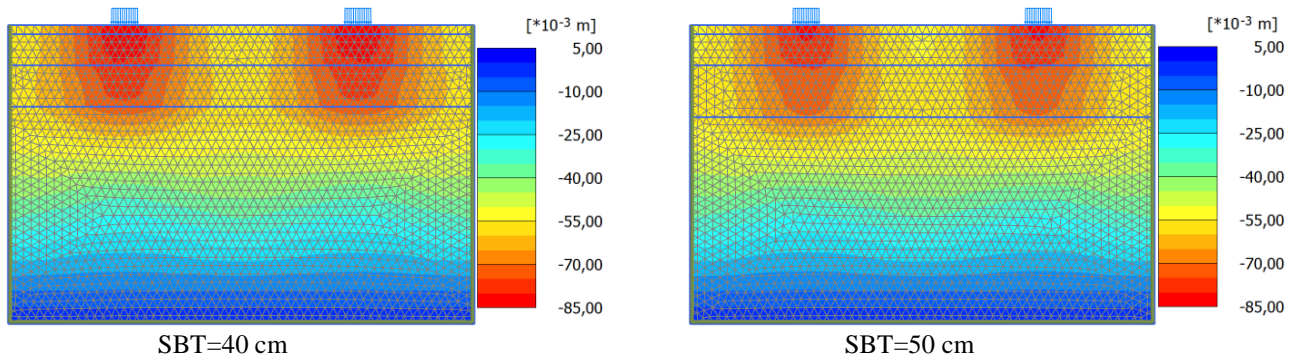


**Figure 8.** Vertical displacement contour diagram( $u_y$ ) of pavement with sub-base at 30, 40, and 50 cm thickness (ACT=9 cm; Pressure=600 kPa)

At the end of the analysis, the deformation values on the pavement surface were determined. Figure 9 shows the surface deformation on the pavement without a sub-base layer caused by an increase in asphalt thickness. The deformations on the pavement surface without the sub-base layer are shown in Figure 10, which shows the influence of the ACT. Figure 11 illustrates that the variations in pavement surface deformation resulting from the addition of a sub-base layer of different thicknesses (30, 40, or 50 cm) under a 9 cm layer of asphalt concrete and a 30 cm base layer. Figure 12 shows the differences in deformations on the surface of the pavement (ACT=9 cm) with and without a subbase layer at depths of 30, 40, and 50 cm.

As seen in Figure 9, the deformations on the pavement surface increased due to the increase in the applied load on the pavement without sub-base. At low pressures, such as 100 kPa, the deformations on the pavement surface were close to each other, while it was observed that the deformations on the surface increased as the applied pressure increased.

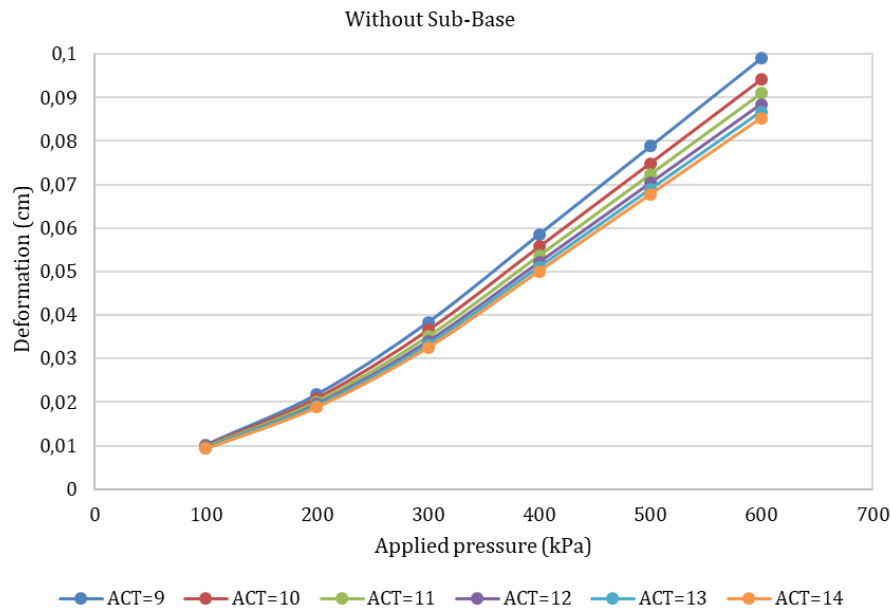


**Figure 9.** Deformations of different asphalt thicknesses on pavement surfaces without sub-base (ACT=9 cm)

Figure 10 shows that an increase in the thickness of the asphalt concrete layer results in a decrease in deformation. The greatest deformation was observed when the asphalt layer thickness was 9 cm, whereas the smallest deformation occurred at an asphalt layer thickness of 14 cm. Furthermore, it was observed that increasing the asphalt thickness at low loads had no effect on deformation significantly, but at loads of 300 kPa and above, it considerably decreased deformation formation. It can be said that it may be more appropriate to increase the pavement thickness under

conditions of large loading on the pavement.

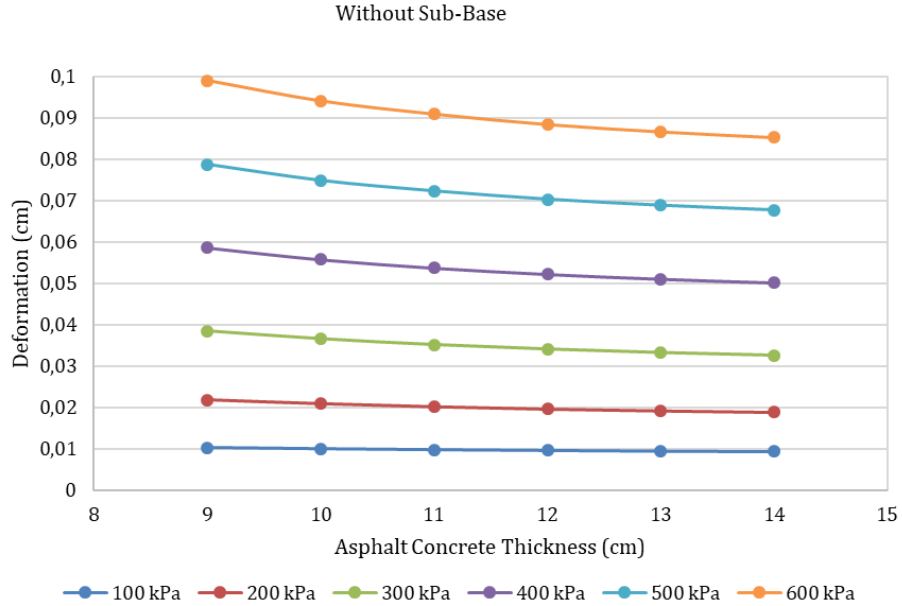


Figure 10. Effect of asphalt layer thicknesses on pavement surface deformation (without sub-base)

As seen in Figure 11, it was observed that the deformation decreased with increasing sub-base thickness. Similar to the without sub-base pavement, the thickness of the subbase has little influence on deformation at low pressures but a greater effect at pressures of 300 kPa and above.

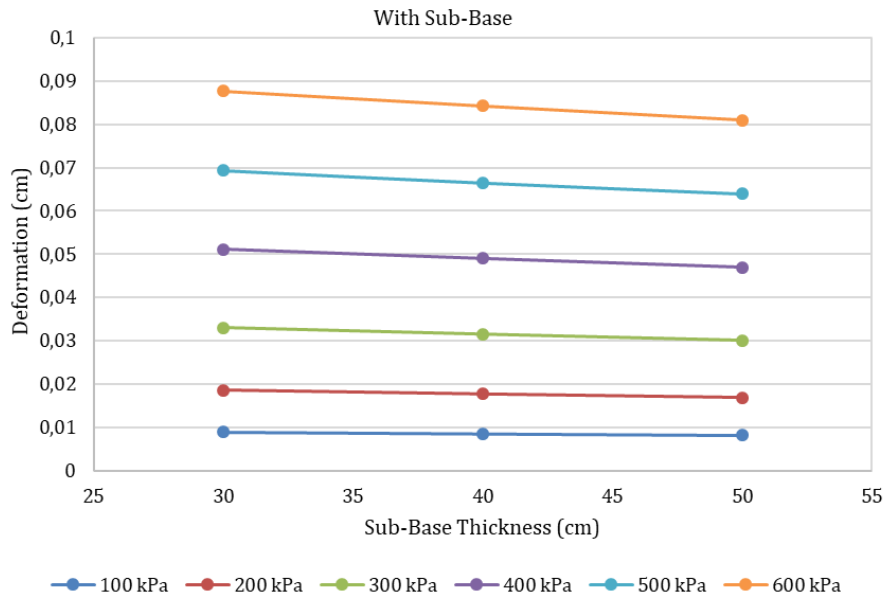
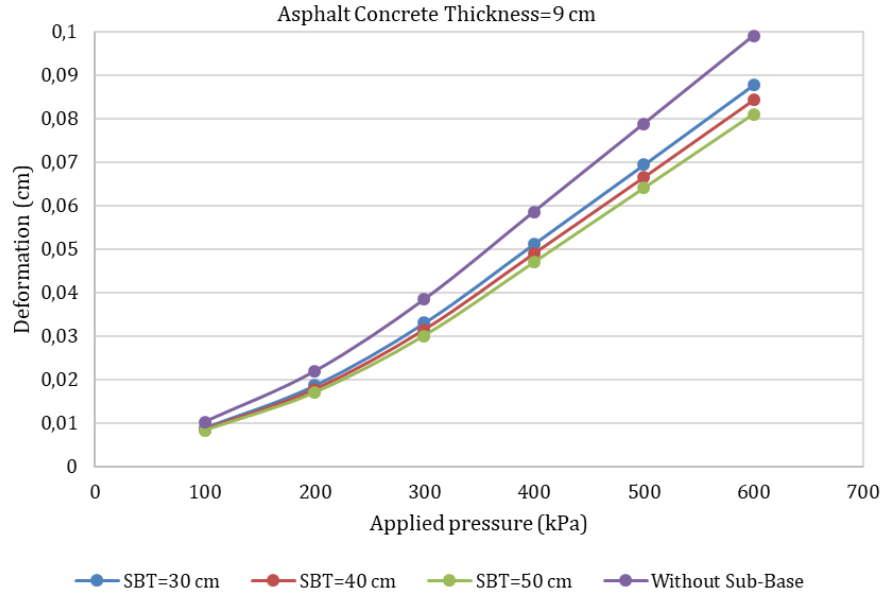


Figure 11. Effect of sub-base layer thicknesses on pavement surface deformation (ACT=9 cm)

The use of a sub-base layer in the pavement considerably increases the deformation resistance, as shown in Figure 12, when the effect of sub-base layer thickness and the absence of sub-base on deformation is examined. It was also observed that adding a 30 cm thick sub-base layer to the pavement improved the deformation resistance more than increasing the asphalt thickness without using sub-base.





**Figure 12.** Effect of with and without sub-base layer on deformation (SBT= 30, 40, 50 cm, ACT=9 cm)

#### IV. CONCLUSION

In this study, the effect of the layer thicknesses used in the pavement deformation was investigated using Plaxis 2D software. The following findings were obtained as a result of the completed study:

1. The analyses were conducted on a pavement model with asphalt thicknesses ranging from 9 cm to 14 cm, specifically on the base layer. It was observed that the deformation of the pavement surface decreased with increasing asphalt thickness.
2. It was noted that increasing the asphalt layer thickness at lower loads did not have a significant impact on deformation. However, at loads of higher than 300 kPa, it notably reduced deformation formation. Under high loading conditions, it might be more suitable to consider increasing asphalt layer thickness.
3. The deformations obtained from 9 cm and 14 cm asphalt layer thickness of the models without subbase were compared in percentage. As a result, it was observed that 8.89%, 13.57%, 15.22%, 14.48%, 14.09% and 13.90% reduction in deformation occurred at 100, 200, 300, 400, 500 and 600 kPa loadings, respectively. According to this result, it is seen that 300 kPa load is the critical load as stated in result number 2.
4. In the without subbase model under 600 kPa loading, depending on the 1 cm increase in the coating thickness, the deformations decreased by 4.96%, 8.17%, 10.71%, 12.49%, and 13.90%, respectively, compared to the 9 cm coating thickness.
5. In the other model, where the sub-base was added at 30, 40, and 50 cm, the asphalt pavement thickness was 9 cm, it was observed that the deformation of the pavement surface decreased with increasing sub-base thickness. However, the results showed that the deformation resistance of the pavement surface increased more with the addition of sub-base compared to the increase in asphalt thickness in the pavement layer.
6. The deformations obtained from 30 cm and 50 cm subbase thickness of the models were compared in percentage. As a result, it was observed that 5.62%, 6.84%, 6.78%, 6.28%, 5.95% and 5.80% reduction in deformation occurred at 100, 200, 300, 400, 500 and 600 kPa loadings, respectively.
7. According to all the analysis results, it is understood that the increase in subbase thickness shows better performance in reducing deformation than the increase in the thickness of the asphalt pavement. Consequently, this type of analysis is beneficial for designing a pavement, as it provides an equilibrium between the fatigue and rutting lifetimes [10]. This study included the modelling of asphalt behavior under low temperature conditions. However, as the temperature increases, the deformations on the asphalt surface also increase. Therefore, it is recommended to investigate the effect of temperature, different loading conditions, different material properties

on the deformation of asphalt pavement in future studies. Investigating the effect of soil properties on the deformations that will occur on the pavement surface will also contribute to future studies.

### CONFLICTS OF INTEREST

They reported that there was no conflict of interest between the authors and their respective institutions.

### RESEARCH AND PUBLICATION ETHICS

In the studies carried out within the scope of this article, the rules of research and publication ethics were followed.

### REFERENCES

- [1] S. Ahirwar, and J. Mandal, "Finite element analysis of flexible pavement with geogrids," *Procedia Engineering*, vol. 189, pp. 411-416, 2017.
- [2] Ł. Mejłun, J. Judycki, and B. Dołżycki, "Comparison of elastic and viscoelastic analysis of asphalt pavement at high temperature," *Procedia Engineering*, vol. 172, pp. 746-753, 2017.
- [3] M. J. Minhoto, J. C. Pais, P. A. Pereira *et al.*, "Predicting asphalt pavement temperature with a three-dimensional finite element method," *Transportation Research Record*, vol. 1919, no. 1, pp. 96-110, 2005.
- [4] H. Wang, and I. L. Al-Qadi, "Near-surface pavement failure under multiaxial stress state in thick asphalt pavement," *Transportation Research Record*, vol. 2154, no. 1, pp. 91-99, 2010.
- [5] H. Karadag, S. Firat, N. S. Isik *et al.*, "Determination of permanent deformation of flexible pavements using finite element model," *Građevinar*, vol. 74, no. 06., pp. 471-480, 2022.
- [6] J. R. Mattos, W. P. Núñez, J. A. Ceratti *et al.*, "Shear strength of hot-mix asphalt and its relation to near-surface pavement failure—A case study in Southern Brazil."
- [7] C. C. Patil, and P. Shivananda, "Effect of axial stiffness of geogrid in the flexible pavement deformation through finite element analysis with Plaxis 2D," *Elastic*, vol. 42, no. 40, pp. 5, 2017.
- [8] M. A. H. Al-Jumaili, "Finite element modelling of asphalt concrete pavement reinforced with geogrid by using 3-D plaxis software," *International Journal of Materials Chemistry and Physics*, vol. 2, no. 2, pp. 62-70, 2016.
- [9] H. Faheem, and A. M. Hassan, "2D PLAXIS finite element modeling of asphalt-concrete pavement reinforced with geogrid," *JES. Journal of Engineering Sciences*, vol. 42, no. 6, pp. 1336-1348, 2014.
- [10] A. B. Tapase, and M. Ranadive, "Performance evaluation of flexible pavement using the finite element method," *Geo-China 2016*, pp. 9-17, 2016.
- [11] P. Liu, D. Wang, and M. Oeser, "Application of semi-analytical finite element method to analyze asphalt pavement response under heavy traffic loads," *Journal of traffic and transportation engineering (English edition)*, vol. 4, no. 2, pp. 206-214, 2017.
- [12] S. Özcanan, and M. V. Akpınar, "Esnek Üstyapılarda Kritik Tekerlek ve Aks Konfigurasyonların Mekanistik Analizlere Göre Tespit Edilmesi," *Teknik Dergi*, vol. 25, no. 121, 2014.





## RESEARCH ARTICLE

# Identifying Traveler Groups Lacking in Seatbelt Usage and Suggesting Policy Measures

\*<sup>1</sup>Uneb Gazder, and <sup>1</sup>Ashar Ahmed

\*University of Bahrain, College of Engineering, Civil Engineering Department, Sakhir, Bahrain  
[email.ugazder@uob.edu.bh](mailto:email.ugazder@uob.edu.bh), [Orcid.0000-0002-9445-9570](https://orcid.org/0000-0002-9445-9570)

<sup>1</sup>NED University of Engineering and Technology, Karachi, Pakistan  
[ahmed@cloud.neduet.edu.pk](mailto:ahmed@cloud.neduet.edu.pk), [Orcid.0009-0009-6432-0242](https://orcid.org/0009-0009-6432-0242)

**Citation:**

Gazder, U., Ashar, A. (2024). *Identifying Traveler Groups Lacking in Seatbelt Usage and Suggesting Policy Measures*, Journal of Science Technology and Engineering Research, 5(1):34-40. DOI: 10.53525/jster.1453840

**HIGHLIGHTS**

- Analysis of seatbelt usage of travelers
- Hybrid data collection technique used
- Identification of important travelers at high-risk due to non-usage
- Policy recommendations to increase safety via seatbelt usage
- Presenting a global perspective with reference to seatbelt usage

**Article Info**

Received : 17 March 2024

Accepted : 07 May 2024

**DOI:**

10.53525/jster.1453840

**\*Corresponding Author:**

Uneb Gazder

[ugazder@uob.edu.bh](mailto:ugazder@uob.edu.bh)

Phone: +973 17 876307

**ABSTRACT**

*This study was aimed to identify the traveler groups who are exposed to potential of severe injury due to lack of seatbelt use. Moreover, policy measures have been suggested to enhance seatbelt use among such groups. A hybrid data collection approach was adopted to gather traveler information. Seatbelt usage questionnaire was used as the survey instrument. The survey was carried out in the parking lots of educational and commercial facilities around Bahrain. Statistical tests, namely, t-tests and Analysis of Variance (ANOVA), were used to compare the attributes of travelers. Literature review was used to verify the findings of this study and identify common traveler groups which are lacking in seatbelt use. The recommendations are also provided on policy measures which could be adopted globally to promote seatbelt use. It was found that occupation, education, gender, nationality and accident occurrence have significant impact on seatbelt wearing. It was also found that accident experience and seatbelt wearing, both are dependent on travelers' social and cultural background rather than each other. The findings of this study matched previous literature. Groups lacking in seatbelt use included male passengers belonging to lower- and middle-income groups which fits the description of expatriate workers in Bahrain. Some policy measures, appropriate to these groups, have also been suggested.*

**Keywords:** *Seatbelt use, Travelers' characteristics, Hybrid data collection, Bahrain, Comparison*

## I. INTRODUCTION

Road traffic accidents have been an issue of concern for many researchers in the past decades, especially with the increase in motorization globally. In this context, seatbelts are among one of the primary safety features for drivers and passengers. Seatbelts prevent ejection of drivers or passengers from the car-seat, in case of accident. Failure in avoiding ejection has 75% and 40% chances of fatality of drivers and passengers, respectively [1]. Seatbelt usage has been related to occurrence of serious injuries and fatalities among Gulf countries with a comparative increase of 52% in death rate with non-compliance [2]. A study done for Bahrain showed that fastening the seatbelt is an important indicator of driver behavior with regards to their tendency to get into accidents with an increase of 75% for those who do not comply with wearing seatbelts among students [3].

There have been several studies to investigate the effects of different factors on seatbelt wearing behavior. The use of seatbelts has been reported to be more among drivers than passengers [4]. Other variables, which have been tested for their significant effect on seatbelt wearing behavior include age, gender, awareness campaigns and previous accident experience. It was found that young males who do not have awareness and priori experience of accidents have higher likelihood of not using seatbelts [5]. The cultural differences in the travelers are also among the factors found to be affecting seatbelt wearing behavior, with a lesser likelihood of wearing seatbelts among non-natives in USA [6]. Education level has also been investigated for its effect on travelers' usage of seatbelts with an increase in use of seatbelt with increase in education level [7]. The same trend has been reported in the context of Gulf countries. Additionally, driver experience was also found to increase the use of seatbelts [8]. A study done in Saudi Arabia shows that compliance to seatbelt is higher in drivers as compared to front seat passengers by more than 30%. Compliance levels also increased with the increase in income level. Awareness campaigns coupled with strict police enforcement have also been found to increase use of seatbelts [9]. Aforementioned studies have primarily employed statistical tests for exploring the factorial impacts of traveler characteristics on seatbelt usage.

In some studies, the data was collected by asking the travelers about their preference to wear seatbelts instead of observing their actual practice [10]. On the other hand, studies employing the observational approach have been found to record a limited number of variables, such as age, gender and seating position [11]. Due to these reasons, some studies have employed data collection in two stages, including a survey and later on simulator/field measurements [12]. But this approach could have inconsistent results as the survey participants and field subjects are not exactly the same. Most of the studies found in this research area have been focused on specific types of travelers or limited to a specific region.

Significant impact of changes in traffic laws and policies on seatbelt wearing behavior has been recorded regularly. The strict enforcement is reported to have approximately 10% increase in seatbelt which was also directly proportional with the increase in amount of fine [13]. Consequently, seatbelt law has been reported as an effective measure for reduction in serious injuries and fatalities in UAE, Bahrain and Saudi Arabia [14]. In Bahrain, it has been reported to reducing the fatalities by 75% and serious injuries by 19% approximately during 1991-2001 [15]. In this context, it is important to know the traveler groups which must be focused on making new policies or adopting different law enforcement measures. Hence, this study focused on identifying types of drivers and passengers, around the world, who have comparatively lower use of seatbelt. A hybrid data collection approach was employed to gather information about travelers and their behavior. Moreover, effort was also made to include travelers from different sections of society in the dataset so that the results are comprehensive and not limited to specific segment(s) of population in Bahrain. The findings of the study were also compared with the global scenario.

## II. METHODS

The primary data for this study was collected in 2016 for Bahrain. Bahrain has been experiencing a consistent increase in vehicle ownership and, consequently, number of accidents as well [16]. The fatalities in road accidents constituted 51% of total fatalities in Bahrain in the previous decade [17].

A. *Questionnaire survey*

A questionnaire was prepared to collect data about the travelers’ characteristics affecting seatbelt usage. The survey was carried out in the parking lots of different types of locations of Bahrain. These locations included parking lots of the following facilities: shopping malls including Bahrain City Center, Juffair Mall and Hayat Mall, Prince Khalifa bin Salman Park and educational institutions; including University of Bahrain (Sakhir Campus) and Bahrain Polytechnic. The minimum sample size for each location type was kept as 100, to avoid any bias.

The number of surveyed travelers reached 800 participants. However, each respondent did not answer all the questions, so, the number of responses for each question was not 800. Table 1 represents the variables which have been used in the analysis from survey data while the number of valid responses achieved for each variable are mentioned in table 2.

**Table I.** Description of Variables

Variable	Description
Seating position	Categorical; driver and front seat passengers
Age	Continuous
Driving experience	Continuous
Education	Categorical; less than high school, high school pass, BS, MS and PhD
Occupation	Categorical; student, housewife, unemployed, self-employed, employed and retired
Gender	Categorical; male and female
Nationality	Categorical; Arab, sub-continent national (India, Pakistan and Bangladesh) and other nationals
Accident	Categorical; having or not having an accident

**Table II.** Statistical Comparison for Overall Data

Variable	Test Type	Result	Sample Size (n)
Seating position	T-Test	NS	317
Age	T-Test	NS	721
Driving experience	T-Test	NS	722
Education	ANOVA	S	261
Occupation	ANOVA	S	258
Gender	T-Test	S	345
Nationality	ANOVA	S	255
Accident	T-Test	S	795

Note: NS = difference is insignificant; S = difference is significant

The hybrid data collection approach, proposed in this study, was carried out in two steps. First, surveyors observed the usage of seatbelt for the randomly chosen traveler and then they approached him/her for the interview in the next step. So, the data was not skewed by the response of the traveler about their seatbelt usage. This hybrid approach study combines observational data with relatively detailed interviews giving the chance to investigate more factors with accurate observations of seatbelt usage.

B. *Analysis methods*

Table 1 presents the description of variables collected in the questionnaire. The questionnaire consisted of twelve questions. Most of the variables collected in this study were found in the previous studies as well, so it was possible to compare these traveler characteristics with other regions. The number of variables (number of parameters about the traveler) collected in this study are more than any other observational study found for seatbelt usage. Each question of the survey was analyzed, using either a t-test or analysis of variance (ANOVA), depending on the type of data. T-test was found to be used in previous studies for comparing means and proportions [18]. Whereas, ANOVA has been recommended to investigate the differences in various groups of a dataset [19]. A confidence level of 95% was used to test the significance of these tests.

### III. RESULTS

The degree of compliance for seatbelt in the collected data was around 70%, which was found to be consistent at all survey locations. Table 3 presents the descriptive statistics of the traveler characteristics and seatbelt wearing behavior data. It can be observed that the compliance ratio is more than 50% for all categories of travelers. Travelers having higher education (above BS) and retired were found to be with highest compliance rates.

**Table III.** Descriptive Statistics of Overall Data

Variable	Value for wearing seatbelt	Value for not wearing seatbelt
Drivers wearing seatbelt	68% (422)	32% (198)
Passengers wearing seatbelt	58% (48)	42% (35)
Average age of travelers	31 years	29 years
Average driving experience of travelers	8 years	8 years
Travelers having less than high school education	67% (24)	33% (12)
Travelers having only high school education	69% (29)	31% (13)
Travelers having more than high school till diploma	83% (34)	17% (7)
Travelers having more than diploma till BS	69% (129)	31% (58)
Travelers having more than BS till MS	94% (30)	6% (2)
Travelers having more than MS till PhD	100% (5)	0% (0)
Students	62% (93)	38% (44)
Housewives	82% (32)	18% (7)
Unemployed travelers	50% (09)	50% (09)
Self-employed travelers	76% (32)	24% (10)
Employed travelers	84% (92)	16% (18)
Retired travelers	88% (7)	12% (1)
Male	72% (131)	28% (59)
Female	83% (121)	17% (34)
Arabs	83% (60)	17% (28)
Sub-continental nationals	68% (65)	32% (13)
Other nationals	57% (51)	43% (38)
Travelers having accident	76% (179)	24% (57)
Travelers not having accident	81% (453)	19% (106)

#### A. Factorial analysis

Table 2 shows the results of statistical tests for each variable in the data. The t-test was performed for the null hypothesis that there is no significant difference between average or proportion of drivers wearing and not wearing the seatbelt. It was found that gender and accident experience have a significant impact on use of seatbelt with higher proportion of use by female travelers and people without accident experience (as shown in Table 3). The later observation could mean that wearing seatbelt is a result of travelers' cautious behavior which also results in avoidance of accidents. While travelers who are less cautious about traffic laws (such as wearing seatbelts) are also more prone to accidents.

The ANOVA test was performed with the null hypothesis that there is no significant effect of education level, occupation and nationality on the proportion of travelers wearing seatbelts. The null hypothesis was rejected in all the cases.

#### B. Comparison with global context

A comparison of the findings of this study with those from previous studies conducted in other parts of the world, including Gulf countries, was conducted. The primary purpose of this effort was to identify groups of travelers who commonly lack seatbelts and should be focused on promoting the use of seatbelt. A selected number of studies are listed in Table 4 for convenience. Studies published before 2000 were not included as their findings may not be applicable to the current scenario. The table shows that most of the findings of this study coincide with those of previous studies.

**Table IV. Overview of Variables in Global Context**

Variable	Studies	Region	Conclusion
Seating position	Kulanthayan et al. [20]	Malaysia	Drivers have significantly higher proportion
	Bendak [9]	Saudi Arabia	
Age	Corona insights [21]	USA	No significant effect of age at 95% confidence
	Yellman [22]	USA	Almost equal proportion of teenagers wearing and not wearing seatbelts (reported from previous studies)
Driving experience	Al-Madani et al. [8]	UAE	Seatbelt usage increases with experience
Education	Al-Madani et al. [8]	Qatar	No significant effect
	Kulanthayan et al. [20]	Malaysia	Travelers with higher education (BS in this case) wearing seatbelts are twice than others
	Harper et al. [23]	USA	
Gender	Al-Madani et al. [8]	GCC countries	Less educated drivers rarely use seatbelt
	Birru et al. [24]	USA	Female travelers wearing seatbelt is 10-11% more than males
Accidents	Siviroj et al. [5]	Thailand	Prior accident experience was found to be a major motivation for seatbelt wearing

#### IV. DISCUSSION

Analysis done in this study, along with the comparison from previous studies, have resulted in the identification of following traveler groups which lack in use of seatbelt.

- Front seat passengers. This can be observed from tables 2 and 3 that the proportion of drivers wearing the seatbelt is significantly higher than that for front seat passengers. The reason could be that drivers receive formal training and, hence, become more cautious about obeying traffic laws, which is not the case for passengers who may not be licensed drivers.
- Male drivers. It has been investigated in the past that women, in general, are less prone to risk taking than men which could be the reason that their use of seatbelt is significantly higher than men [25, 26].
- Travelers from lower-middle income groups. This is a conclusion which is drawn from the fact that nationality, education and occupation has a significant impact on seatbelt usage (see table 2). Moreover, table 3 shows that non-Arab expatriates, unemployed/students and low education travelers have a significantly lower proportion of seatbelt use as compared to their counterparts. Possible reasons could be lack of education and understanding of traffic rules at the primary education level, non-familiarity with local conditions (such as for travelers from other nationalities), not having formal training for license and lack of attention to their own safety. This finding is substantiated by Al-Madani [27] who found a correlation for comprehension of traffic signs and seatbelt wearing.

Based upon the above observations, it is important to develop policies and strategies focusing on these groups in order to improve their safety. It is recommended to go beyond the traditional means of traffic education which is presently done through educational and driving schools. Use of social media and roadside campaigns may have a deeper penetration in the above-mentioned groups. Furthermore, devising campaigns with multilingual and audio-visual aids will help to educate the lower-middle income groups of travelers. These recommendations were also advocated by Bendak [9]. Traffic laws and their implementation, as stated earlier, do have a role in improving travelers' behavior but passengers should be also given same importance, as drivers, when implementing these laws. Front seat passengers, in spite of being exposed to the same risk of injury due to an accident, often get away with not following traffic laws related to their safety. The above recommendations can be applied globally, since the traveler groups lacking in use of seat belt use, seem to be the same across different countries.



An interesting observation was regarding the accident experience which was significantly lower for seatbelt wearing travelers. So, it could be concluded that accident and wearing seatbelt, both are dependent upon socio-cultural background of travelers rather than each other. More cautious drivers tend to avoid accidents and wear seatbelts. Hence, taking measures to increase the use of seatbelts may have an inherent effect on increasing caution by the travelers and reducing their accidents. This trend was also recorded in one of the previous studies [3]. Moreover, Tables 2 and 3 show that the number of participants who are non-compliant with seatbelt and have accident experience are significantly lower than their counterparts. So, there could be a possibility of causal relationship between these parameters. However, it could be only confirmed with more data including the accident severity which was not taken at the time of this study.

## **V. CONCLUSIONS**

This study was aimed at identifying travelers who are less likely to use seatbelts and suggesting policy measures to enhance their seatbelt use. Data collected in this study, from Bahrain, was analyzed and compared with findings of other relevant studies. A hybrid data collection technique, combining observation of behavior and questionnaire, was used in this study. Statistical tests were used to determine the trends among the travelers.

It was found that females, travelers having higher education, housewives and Arabs had significantly higher compliance to seatbelt use than others. The findings of this study mainly coincided with those of previous studies. This was found irrespective of the region in which the studies were done, hence, the results of this study could be considered generic for travelers' seatbelt use.

Based upon these findings, it is recommended to use multilingual audio-visual measures for campaigns, while incorporating social media, to promote the use of seatbelts. A higher focus on implementing traffic safety laws for the passengers is also required. The hybrid data collection approach, applied in this study, seems to be effective in capturing the travelers' behavior accurately with a wider range of variables. For future studies, it is recommended that the effects of different seatbelt use promotion measures could be studied in the context of their effectiveness. These measures could be related to enforcement or driver awareness. Other possible directions could include development of behavioral models and incorporation of accident severity data.

## **STATEMENT OF CONTRIBUTION RATE**

1st author contributed 60%, 2nd author contributed 40%

## **CONFLICT OF INTEREST**

The authors declare no conflict of interest with any person, entity or institution.

## **RESEARCH AND PUBLICATION ETHICS**

In the studies carried out within the scope of this article, the rules of research and publication ethics were followed.

## **ACKNOWLEDGMENT**

The authors acknowledge the technical support provided at the Department of Civil Engineering, University of Bahrain for conducting this research.

## **REFERENCES**


- [1] World Health Organization. (2017). Fact sheet: Road traffic injuries. Retrieved from <http://www.who.int/mediacentre/factsheets/fs358/en/>
- [2] Abbas, A.K., Hefny, A.F., & Abu-Zidan, F.M. (2011). Seatbelt compliance and mortality in the Gulf Cooperation Council countries in comparison with other high-income countries. *Annals of Saudi Medicine* 31(4), 347-350.

- [3] Rasool, F.A.A., Alekri, F.A., Nabi, H.A., Naiser, M.J., Shamlooh, N.M., Alnashaba, S.A., ... Al Sayyad, A.S. (2015). Prevalence and behavioral risk factors associated with road traffic accidents among medical students of Arabian Gulf University in Bahrain. *International Journal of Medical Science and Public Health* 4(7), 933-939.
- [4] Kargar, S., Ansari-Moghaddam, A., & Ansari, H. (2023). The prevalence of seat belt use among drivers and passengers: a systematic review and meta-analysis. *Journal of the Egyptian Public Health Association*, 98(1), 14.
- [5] Siviroj, P., Peltzer, K., Pengpid, S., & Morarit, S. (2012). Non-seatbelt use and associated factors among Thai drivers during Songkran festival. *BMC public health*, 12, 1-7.
- [6] Goldzweig, I.A., Levine, R.S., Schlundt, D., Bradley, R., Jones, G.D., Zoorob, R.J., & Ekundayo, O.J. (2013). Improving seat belt use among teen drivers: Findings from a service-learning approach. *Accident Analysis & Prevention* 59, 71-75.
- [7] Demirer, A., Durat, M., & Haşimoğlu, C. (2012). Investigation of seat belt use among the drivers of different education levels. *Safety Science* 50(4), 1005-1008.
- [8] Al-Madani, H.M., Al-Janahi, A., & Al-Sada, E. (2002). Drivers Characteristics with Respect to Accident Involvement and Seat Belt Utilization. *Journal of King Saud University-Engineering Sciences* 14(1), 1-11.
- [9] Bendak, S. (2005). Seat belt utilization in Saudi Arabia and its impact on road accident injuries. *Accident Analysis & Prevention* 37(2), 367-371.
- [10] Sunshine, J., Dwyer-Lindgren, L., Chen, A., & Mokdad, A.H. (2017). Seat-belt use in US counties: limited progress toward Healthy People 2020 Objectives. *Health Affairs* 36(4), 636-639.
- [11] Head, E. (2016). Assessing seatbelt usage among teenagers in rural settings: The drive alive program, Masters thesis, Public Health Department, Georgia State University.
- [12] Neill, J.M., Hurwitz, D.S., & Olsen, M.J. (2015). Alternative information signs: evaluation of driver comprehension and visual attention. *Journal of Transportation Engineering* 142(1), 1-12.
- [13] Nichols, J.L., Tippetts, A.S., Fell, J.C., Eichelberger, A.H., & Haseltine, P.W. (2014). The effects of primary enforcement laws and fine levels on seat belt usage in the United States. *Traffic Injury Prevention* 15(6), 640-644.
- [14] Rohrer, W. M., Al-Surimi, K., & Lobo, C. P. (2021). Road Traffic Crashes in the Arab World: From Evidence to Public Policy and Action. In *Handbook of Healthcare in the Arab World* (pp. 2419-2452). Cham: Springer International Publishing.
- [15] Hamza, A.Y., Al-Mousawi, F.R., & Husel-Pincock, A. (2003). Road traffic accidents in Bahrain. *Bahrain Medical Bulletin* 25(3), 105-110.
- [16] Alsabbagh, M., Siu, Y.L., Guehneemann, A., & Barrett, J. (2016). Integrated approach to the assessment of CO2 e-mitigation measures for the road passenger transport sector in Bahrain. *Renewable and Sustainable Energy Reviews* 71, 203-215.
- [17] Hamadeh, R.R., & Ali, N.M.A. (2013). Fatalities from road traffic accidents among the young in Bahrain. *Eastern Mediterranean Health Journal* 19(10), 854-860.
- [18] Brijs, K., Daniels, S., Brijs, T., & Wets, G. (2011). An experimental approach towards the evaluation of a seat belt campaign with an inside view on the psychology behind seat belt use. *Transportation Research Part F: Traffic Psychology and Behaviour* 14(6), 600-613.
- [19] Walde, J. (2014). Analysis of Variance (ANOVA). *MFRI Special Publication*, 169-170.
- [20] Kulanthayan, S., Law, T.H., Raha, A.R., & Radin, U.R. (2004). Seat belt use among car users in Malaysia. *IATSS Research* 28(1), 19-25.
- [21] Corona Insights. (2011, June 6). Seat belt usage and campaign awareness survey – May-June 2011 Mobilization impact, Report prepared for Minnesota Department of Transportation. Retrieved from <https://dps.mn.gov/divisions/ots/educational-materials/Documents/2011Surveys1-2Report2011-07-22.pdf>
- [22] Yellman, M. A. (2020). Transportation risk behaviors among high school students—Youth risk behavior survey, United States, 2019. *MMWR supplements*, 69.
- [23] Harper, S., Strumpf, E.C., Burris, S., Smith, G.D., & Lynch, J. (2014). The effect of mandatory seat belt laws on seat belt use by socioeconomic position. *Journal of Policy Analysis and Management* 33(1), 141-161.
- [24] Birru, H., Rudisill, T.M., Fabio, A., & Zhu, M. (2016). A comparison of self-reported seat belt usage among the Appalachian and non-Appalachian United States. *Annals of Epidemiology* 26(3), 227-230.
- [25] Blakemore, S. J. (2019). Adolescence and mental health. *The Lancet*, 393(10185), 2030-2031.
- [26] Francis, B., Hasan, I., Park, J.C., & Wu, Q. (2015). Gender differences in financial reporting decision making: Evidence from accounting conservatism. *Contemporary Accounting Research* 32(3), 1285-1318.
- [27] Al-Madani, H. (2000). Influence of drivers' comprehension of posted signs on their safety related characteristics. *Accident Analysis & Prevention*. 32(4), 575-581.



## RESEARCH ARTICLE

# Enhancing Electrical Distribution System Efficiency: A Software Tool Design for Conductor Cross-Section Optimization With TLBO Algorithm

\* Cemil ALTIN

\*Yozgat Bozok University, Faculty of Engineering, Electrical and Electronics Engineering Department, Yozgat, TÜRKİYE  
[cemil.altin@yobu.edu.tr](mailto:cemil.altin@yobu.edu.tr), [Orcid.0000-0001-8892-2795](https://orcid.org/0000-0001-8892-2795)

**Citation:**

Altın, C. (2024). *Enhancing Electrical Distribution System Efficiency: A Software Tool Design for Conductor Cross-Section Optimization With TLBO Algorithm*, Journal of Science, Technology and Engineering Research, 5(1):41-53. DOI: 10.53525/jster.1459185

**HIGHLIGHTS**

- TLBO algorithm used for the first time in cross-section optimization
- For the first time, a cross-section optimization tool was designed with the combination of MATLAB and Excel software
- A new dimension has been introduced to conductor cross-section optimization with the combination of metaheuristic algorithms and different softwares.

**Article Info**

Received : March 26, 2024

Accepted : May 21, 2024

**DOI:**

10.53525/jster.1459185

**\*Corresponding Author:**

Cemil ALTIN

[cemil.altin@yobu.edu.tr](mailto:cemil.altin@yobu.edu.tr)

Phone: +90 539 3763556

**ABSTRACT**

*In radial distribution networks with many separate branches and sections, it is very difficult to calculate the optimum conductor cross-section. This work introduces a new tool for optimizing conductor cross-sectional area in electrical distribution systems by utilizing the Teaching-Learning-Based Optimization (TLBO) algorithm. The tool can optimize the conductor cross-section of the multisection, branching distribution systems. The maximum current carrying capacity constraint is taken into consideration when formulating the objective function to choose the ideal conductor size for each network segment. The optimal conductor sizes are determined by both desired percent voltage drop and current carrying capacity of the conductor. By calculating the currents drawn from the line segments in advance, the search space of the optimization algorithm is narrowed. MATLAB and Excel were used to determine the ideal conductor size. The conductor, which is chosen using the suggested method, will preserve appropriate voltage levels in radial distribution systems while optimizing the overall savings in conducting material and energy loss costs. The outcomes show that the optimal selection of conductor problem can be solved by the TLBO algorithm in a practical and effective manner. Results of testing the suggested tool on a radial distribution system are noteworthy.*

**Keywords:** Distribution Networks, TLBO, Metaheuristics, Conductor Optimization

## I. INTRODUCTION

The best choice of conductor sizes is critical to the effective design and operation of radial distribution systems. To address this important factor, researchers have developed a variety of methodologies and algorithms over time. The purpose of this review of the literature is to give a broad overview of the developments in conductor size selection for radial distribution systems, emphasizing significant contributions and techniques used.

Early studies, such as those by Wang et al. in 2000 [1] and Sivanagaraju et al. in 2002 [2], laid the groundwork for conductor size selection methodologies. These studies concentrated on useful methods and optimization strategies for figuring out the ideal conductor sizes for radial distribution systems while taking load characteristics and system limitations into account.

In a study conducted in 2023 by Gallego Pareja et al. Mixed Integer Linear Programming (MILP) model is suggested for primary distribution systems that simultaneously optimizes the placement of capacitor banks and conductor selection, highlighting the significance of taking reactive power management into account in addition to conductor sizing [3]. Voltage regulation and system efficiency are improved by this integration.

Numerous research works have showcased case studies and practical implementations of ideal conductor selection techniques. In 2017, The benefits and usefulness of choosing the best conductor for distribution system planning were demonstrated by Joshi et al. [4]. A case study conducted in 2010 on the best conductor selection for agricultural distribution systems was presented by Raju et al., emphasizing the value of customized solutions for particular applications [5]. Ranjan et al. in 2006 [6] and Kumari et al. in 2018 [7] examined the application of evolutionary programming methods for the best conductor selection, placing a focus on the accuracy of the solutions and computational efficiency. In addition to addressing financial considerations, Waseem et al. provided an affordable technique for optimal cable sizing to reduce power loss and save energy in 2018 [8]. Methodologies for selecting conductor size have come a long way, but issues with scalability, computational complexity, and integration with new technologies still need to be resolved. Prospective avenues for research could encompass the advancement of hybrid optimization methodologies, integration of renewable energy sources, and contemplation of dynamic operating conditions to augment system resilience. Within the field of electrical engineering, distribution system design optimization is still a vital undertaking to guarantee effectiveness, dependability, and economy. The careful selection of conductor cross-sections, which directly affects system performance and operational integrity, is essential to this optimization. This paper presents a novel approach to conductor cross-section sizing by integrating MATLAB and Excel, utilizing MATLAB's computational power and Excel's intuitive interface to expedite the design process. The software tool uses a metaheuristic optimizer to help engineers make well-informed decisions about the size of conductors, which will ultimately improve the dependability and efficiency of electrical distribution systems. This introduction lays out the purpose, goals, and structure of the suggested software tool and prepares the reader for a thorough examination of its design principles and real-world uses.

For efficiency and dependability, it is essential to optimize electrical distribution systems, which are vital in transporting electricity from generation sources to end users. Utilizing sophisticated computational techniques and tools to tackle intricate problems related to system design and operation characterizes the state of the art in conductor cross-section optimization.

Conductor cross-section optimization has been transformed by recent developments in computational techniques, such as numerical simulation and optimization algorithms. Advanced simulation capabilities are available for analyzing distribution system performance under different operating conditions through software tools such as PSCAD/EMTDC and DiGSILENT. However, not all engineers may have access to these tools and they usually require specific knowledge.

For the optimization of conductor cross-section, the combination of MATLAB and Excel offers a strong substitute. Excel offers a recognizable interface for data input, manipulation, and visualization, while MATLAB offers a robust platform for numerical analysis, optimization, and modeling. By utilizing the advantages of both platforms, this combined method enables engineers to carry out complex analyses quickly and easily.

The suggested software tool offers a thorough approach to conductor cross-section optimization in the MATLAB and Excel environments, improving upon current techniques. Through the integration of sophisticated computational methods with intuitive user interfaces, the approach seeks to enable engineers to more easily access conductor sizing tools and make well-informed decisions about the design and operation of distribution systems.

In conductor cross-section optimization, the application of metaheuristic optimization algorithms has gained popularity, enabling engineers to methodically look for the best solution within a predetermined design space. Specifically, metaheuristic algorithms have demonstrated potential in handling intricate optimization issues involving numerous goals and limitations.

Although there have been significant advances in the literature in conductor cross-section optimization recently, tools that combine computational power and user-friendly interfaces that are both accessible and versatile are still needed. The software tool that was created fills this need by providing a workable and effective way to increase the effectiveness of electrical distribution systems.

Additionally, although previous research has shed light on a variety of approaches and instruments for conductor cross-section optimization, there is a noticeable lack of studies that particularly address the incorporation of metaheuristic algorithms like TLBO into the MATLAB and Excel environments for this purpose. This study aims to close this gap by presenting a brand-new software tool design that optimizes conductor cross-sections using the TLBO metaheuristic algorithm by combining the computational power of MATLAB with the intuitive interface of Excel.

In radial distribution systems, choosing the right conductors is essential to reliable power delivery, reduced losses, and improved system performance. To solve this challenging engineering problem, researchers have investigated a number of metaheuristic optimization strategies over time. This review of the literature attempts to give a thorough overview of how these methods have evolved, with a particular emphasis on how they are used in radial distribution systems to choose the best conductors.

Because metaheuristic optimization algorithms are effective at solving complicated optimization problems, they have attracted a lot of attention. For the best conductor selection in radial distribution systems, these algorithms—which include Evolutionary Strategies (ES), Particle Swarm Optimization (PSO), Genetic Algorithm (GA), Differential Evolution (DE), Imperialism Competitive Algorithm (ICA), Harmony Search Algorithm (HSA), Whale Optimization Algorithm (WOA), and Crow Search Algorithm (CSA) have been used extensively.

Mendoza et al. in the year of 2006 established the use of evolutionary strategies for conductor size selection, which served as the basis for further studies in this field [9]. In 2009 a discrete PSO approach was proposed by Sivanagaraju and Rao, who also showed that it works well for conductor selection [10]. In order to minimize loss, Rao looked into the use of Differential Evolution in radial distribution systems in a study conducted in 2010 [11].

The integration of conductor selection and capacitor placement has been the subject of numerous studies aimed at improving system performance. In 2014 Mozaffari Legha combined PSO with capacitor placement [12], while Samal et al. utilized DE for simultaneous allocation of capacitors and conductor sizing [13].

Some studies have performed comparative analyses in order to assess how well various optimization algorithms perform. Samet and Mozaffari Legha compared the Imperialism Competitive Algorithm with PSO [14], highlighting its competitive edge. The usefulness of Selective PSO for loss reduction in radial distribution systems was evaluated by Khalil and Gorpnich in 2012 [15].

Novel metaheuristic approaches have been investigated recently for the best conductor selection. Abdelaziz and Fathy introduced the Crow Search Algorithm, demonstrating its efficacy in conductor size optimization [16]. A discrete version of the Vortex Search Algorithm for three-phase distribution networks was proposed by Martinez-Gil et al. in 2021 [17].

From the first uses of ES to more recent developments like CSA and the Vortex Search Algorithm, researchers are still looking for novel ways to solve the problems related to conductor size optimization. These initiatives aid in the creation of more dependable and efficient distribution networks, which eventually helps both consumers and the electricity sector.

The literature review concludes by emphasizing the role that conductor cross-section optimization plays in improving the effectiveness of electrical distribution systems and by pointing out the need for tools that are both accessible and adaptable, capable of fusing sophisticated optimization algorithms with user-friendly interfaces. By utilizing the TLBO metaheuristic algorithm in the MATLAB and Excel environments, the suggested software tool seeks to meet this need by providing engineers with a workable and effective way to optimize conductor sizing in distribution system design.



## II. MATERIAL AND METHODS

### A. Conductor Cross-section Sizing Proceure

Sizing electrical conductor cross sections involves determining the appropriate size of wires or cables to carry electrical current safely and efficiently while minimizing losses due to resistance. The cross-sectional calculation of a distribution network given as an example in Figure 1 will be calculated step by step. First, the longest and most loaded side of the network is determined. The longest and most loaded part of our network is the TR-2-15-24 side, which is only indicated by important poles.

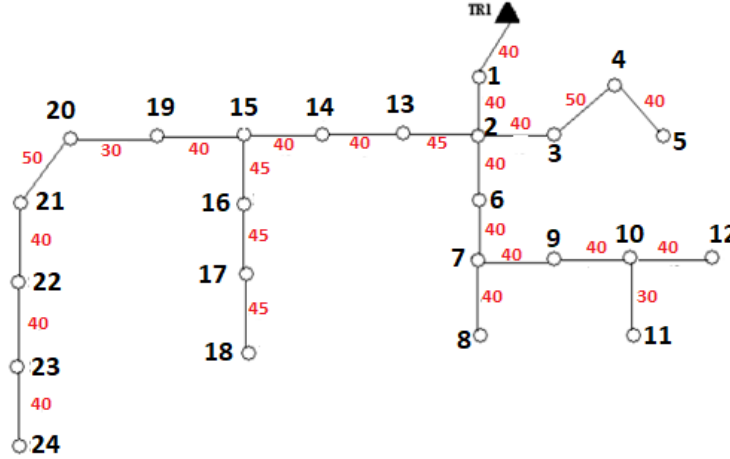


Figure 1. Radial distribution network[18]

In the radiated power method, it is assumed that a certain power is drawn from each unit length of the line. Since the length of the line is certain, the total load between two poles is determined. Since the subscribers are connected to the line through poles, the calculated line loads are reduced to the poles and the pole powers are found. Accordingly, the power drawn from a pole:

$$P_{a-b} = \frac{J * l}{2} \tag{1}$$

Here  $P_{a-b}$ :power of the pole (W),  $l$ :distance between a-b poles (m),  $J$ :Radiated power (W/m) (120 W/m in this study). As seen in Figure 2, the loads drawn from each pole are added up to form the loads that fall on each section of the line following the determination of the pole loads.

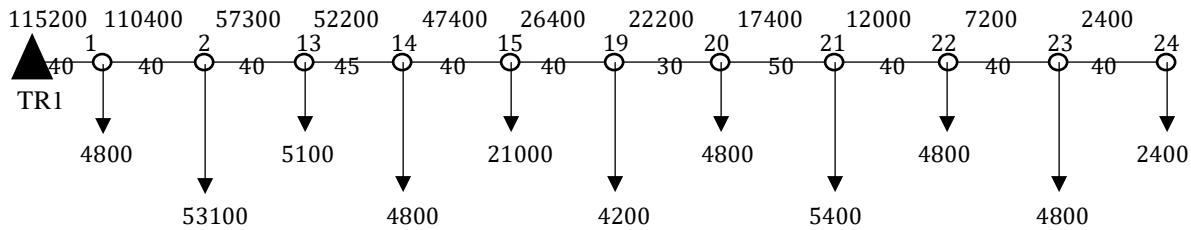


Figure 2. Pole loads and moment diagram

The moment diagram of the power drawn from the system together with the pole powers is shown in Figure 2. The cross-section calculation is done with equation 3. (Voltage drop is chosen 5%)

$$q = \frac{100 * L * P}{3 * k * e \% * V_{PN}^2} \tag{2}$$

Here  $L \cdot P$  is the moment (M) and is calculated by multiplying the line length by the power drawn from the line.  $k$  is the conductivity constant of aluminum and has a value of 35.  $e\%$  is the requested percentage voltage drop.  $V_{PN}$  is the phase neutral voltage.

$$M_1 = 40 * 115200 + 40 * 110400 + 40 * 57300 + 45 * 52200 + 40 * 47400 + 40 * 26400 + 30 * 22200 + 50 * 17400 + 40 * 1200 + 40 * 7200 + 40 * 2400 = 19032562$$

According to the drawn load and the desired voltage drop, the cross-section of the aluminum conductor is  $74.9 \text{ mm}^2$ .

$$74.9 = \frac{100 * 19032562}{3 * 35 * 5 * 220^2}$$

As it is known, the cross sections of aluminum conductors are standard and the calculated value is selected as the closest larger value. Since the cross-section is always selected larger than the calculated cross-section, the cross-section calculation is made again for the parts of the line where relatively less power is drawn. In addition, the cross-sectional calculation here is an end-to-end cross-sectional calculation for the longest and most loaded side of the network. Therefore, it is suitable for the most loaded part of the line, between TR1 and pole number 2, and it must be recalculated for less loaded parts, taking into account the current carrying capacity, without exceeding the percentage voltage drop. Otherwise, a large cross-section network will be designed. Less loaded sections are the sections after the branch poles. In this example, 15-19 carries less load than 2-15 and 2-15 carries less load than TR1-2. This means that between 15-19 should have the thinnest cross-section and between TR1-2 should have the thickest cross-section. However, in the calculation made, the cross-section of the whole line was found to be  $74.9 \text{ mm}^2$  and the conductor named Philox with a cross-section of  $84.99 \text{ mm}^2$ , which is an upper cross-section, will be used. Recalculation is made for thin sections. For this reason, the cross-sectional calculation in radial networks cannot be done in one attempt and calculations are performed repeatedly from the thickest part to the thinnest part according to the complexity of the network. Aluminum conductors used in energy distribution and their properties are given in Table 1.

**Table I.** Aluminum conductors used in energy distribution networks and their properties.

Name	Cross-section ( $\text{mm}^2$ )	Current capacity (A)	K value
Rose	21.14	138	9.308
Lily	26.66	149	7.380
Pansy	42.37	214	4.644
Poppy	53.49	247	3.678
Aster	67.45	286	2.917
Philox	84.99	331	2.315
Oxlip	107.3	393	1.833
Daisy	135.2	443	1.455
Peony	152.1	478	1.293
Tulip	170.6	513	1.153

The K value of the conductor is a parameter used for convenience in voltage drop calculation and is calculated as given in equation 3.

$$K = \frac{100}{3 * k * e\% * V_{PN}^2} \tag{3}$$

Percentage voltage drop using the K value is calculated by Equation 4.

$$e\% = 10^{-7} * K * M \tag{4}$$

Since the cross-section calculation cannot be done in one attempt and requires repetitive operations, a metaheuristic optimization algorithm is proposed to make these tasks easier and in a shorter time.

B. Excel Part of the Study

As mentioned before, the Excel program acts as an interface in this study. The user enters the information about the network into the designed excel program. The Excel sheet has features that can be expanded as much as desired. For complex networks, it allows more information to be entered thanks to the creep feature. The Excel interface design is seen in Figure 3.

B	C	D	E	F	G	H	I	J	K
			Source	Line ---	Branch<:::	Line ---	Branch<:::	Line ---	Branch<:::
Pole numbers			Transforme	-----	0	-----	0	-----	0
Line lengths(L)				0		0		0	
N.of intermediate poles				0		0		0	
Branch Lengths					0		0		0
Industrial Load									
Line power d.(w/m)				0		0		0	
Branch power d.(w/m)					0		0		0
Total line loads(P)				0		0		0	
Line currents				0		0		0	
K values				0		0		0	
Moments				0		0		0	
$\%e_s=10^{-7}$ .K.L.P delta V=		0		0		0		0	
		0		0		0		0	

Figure. 3. Designed Excel Sheet

In the excel sheet displayed in Figure 3, the green cells are filled with the characteristics of the radial network to be designed by the user. This information includes line segment lengths, branch lengths, power densities of the line and branches and the number of poles between the important poles to be used in the moment calculation. The blue cells, i.e. the loads and line currents falling on the line segments, are automatically calculated by excel after the green cells are entered. Line loads are the sums of the loads on the line segments themselves and the loads on the segments after them.

$$P_i = L_{Li} * J_{Li} + L_{Bi} * J_{Bi} + L_{L(i+1)} * J_{L(i+1)} + L_{B(i+1)} * J_{B(i+1)} + \dots + \dots L_{L(i+n)} * J_{L(i+n)} + L_{B(i+n)} * J_{B(i+n)} \quad (5)$$

Where  $P_i$  is the sum of the loads on the  $i$  th line segment,  $L_L$  is the line segment lengths,  $J_L$  is the line segment power densities,  $L_B$  is the branch lengths and  $J_B$  is the branch power densities. After the loads falling on different line segments are found, the currents drawn from the line segments are found with the help of equation 6. Because the conductors must be suitable in terms of current carrying capacity. The currents found here are used to determine the minima of the search space of the metaheuristic algorithm. In other words, the minimum cross sections are determined by the current carrying capacity. The actual cross sections are found by calculating both current carrying capacity and voltage drop. Both the current carrying capacity and a voltage drop below the desired voltage drop ratio must be ensured.

$$I_i = \frac{P_i}{\sqrt{3} * V_i * \cos(\phi)} \quad (6)$$

The blue cells calculated by Excel, i.e. line loads and currents, are read by the MATLAB software with the "xlsread" function. Then, moment calculation is made with the number of intermediate poles and average spans between poles as in Figure 2. After the transfer process from Excel and moment calculation, conductor optimization is performed by the TLBO algorithm running in MATLAB for each segment of the line. The TLBO algorithm

determines the minimum cross-sections by selecting various combinations of K values for the conductors. The TLBO algorithm is only allowed to select K values from the K values of standard conductors. After the optimum conductors are found, MATLAB software sends the K values of these conductors and the moments of the relevant line segments to Excel with the help of the "xlswrite" function. These values are written in yellow cells in the Excel document. The aim is to enable the user to see the voltage drop in terms of voltage and percentage and to validate the suitability of the determined cross-sections. The red cells of the excel file are where the user can see the results and validate the effectiveness of the results. Figure 4 lists every procedure that has been described.

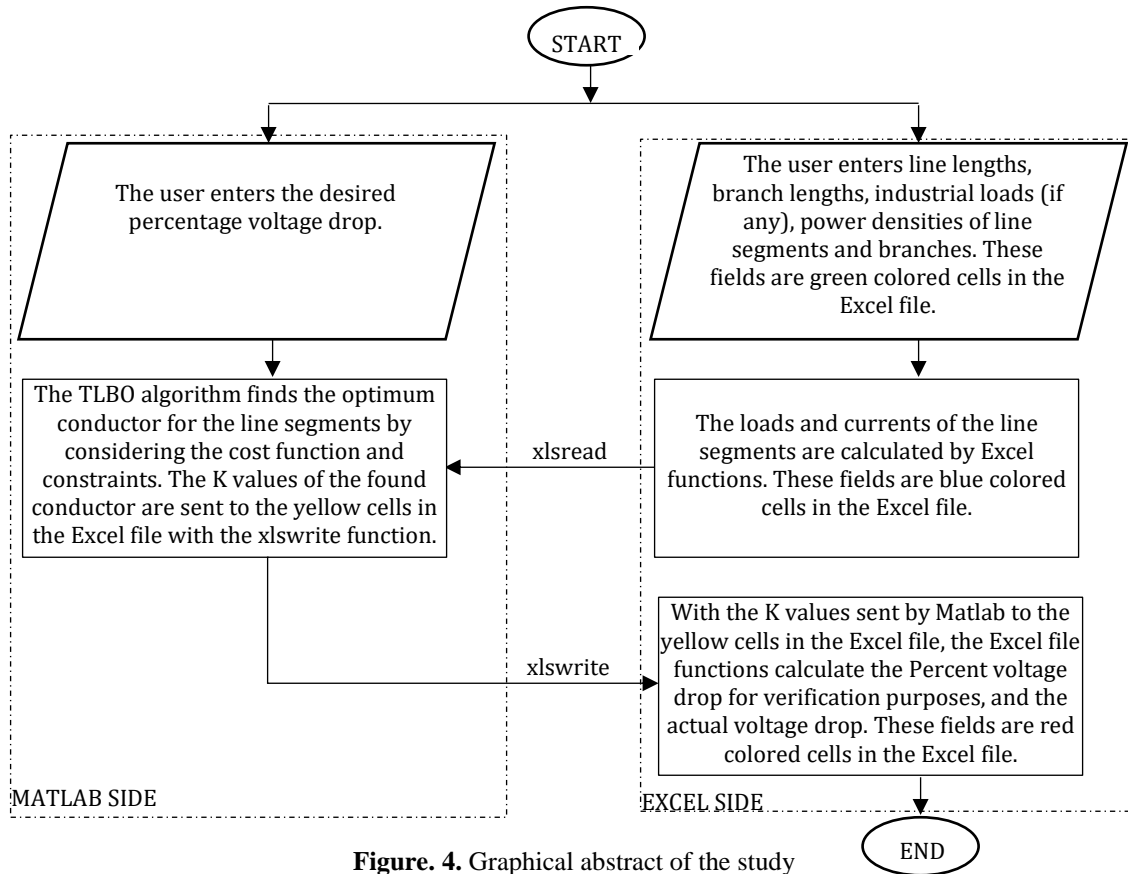


Figure 4. Graphical abstract of the study

### C. Teaching Learning Based Optimization (TLBO)

Population-based optimization algorithm known as Teaching-Learning-Based Optimization (TLBO) was developed with inspiration from the teaching-learning process seen in a classroom. In 2011, Rao et al. presented it [19]. TLBO imitates the way that knowledge is imparted to students by teachers and how students pick up knowledge from one another. This is a basic explanation of how TLBO functions:

1. *Initialization:* TLBO begins with a population of possible solutions that is initially generated, usually at random.
2. *Teacher Phase:* In this stage, the population's best solution the teacher is determined. The instructor then disseminates its expertise (optimal resolution) to every member of the populace.
3. *Student Phase:* During this stage, every member of the population gains knowledge from both their teachers and other people. As part of the learning process, students update their solutions in light of the information that their peers and teacher have shared.
4. *Population Updating:* Based on the newly discovered solutions, the population is updated following the learning phase. In this step, the newly learned solutions are usually substituted for the worst ones.
5. *Termination:* When a stopping condition is satisfied, such as reaching a predetermined number of iterations or

arriving at a workable solution, the algorithm comes to an end.

TLBO has been used to solve a variety of optimization issues, such as machine learning, scheduling, and engineering design. Its effectiveness and simplicity make it a desirable option for resolving optimization issues, particularly when the search space is vast or complicated. The secret to TLBO's success is its capacity to strike a balance between exploitation and exploration by promoting knowledge exchange among members of the populace. Using a collaborative learning approach, high-quality solutions are frequently found in a reasonable amount of time. Figure 5 displays the TLBO algorithm's flowchart.

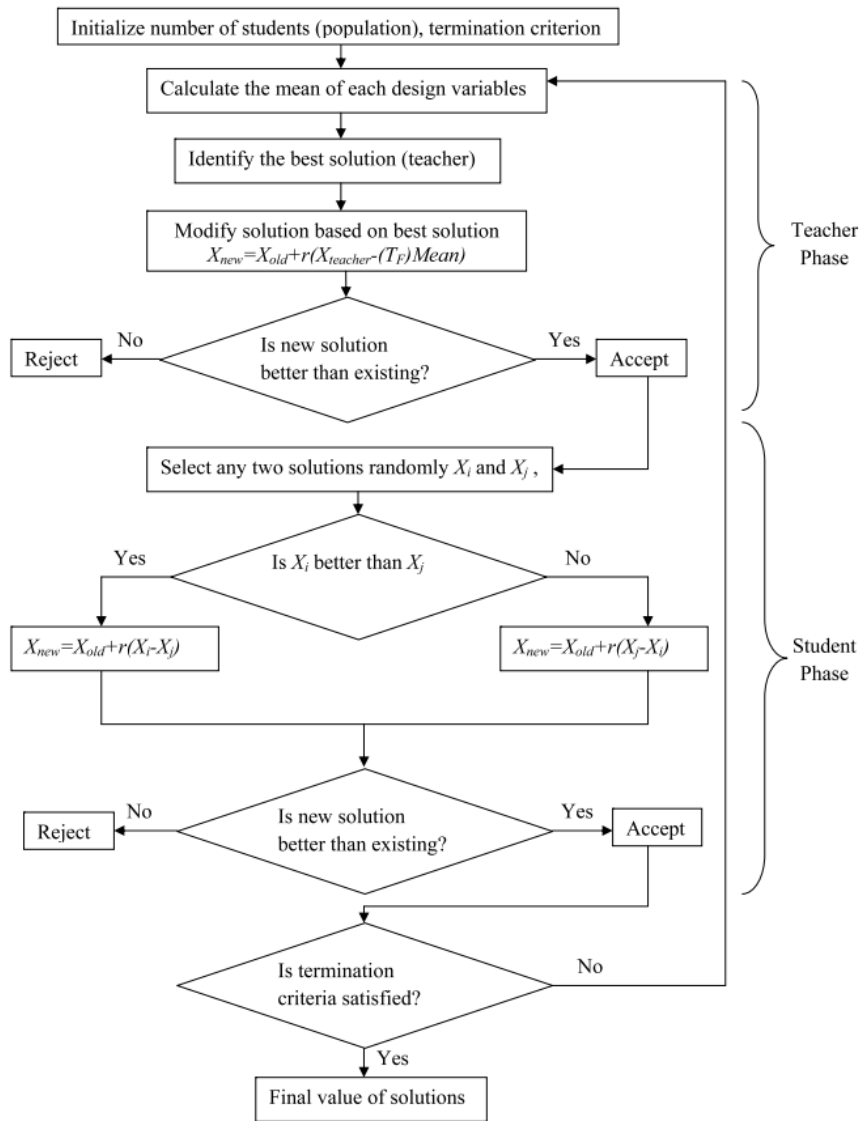


Figure. 5. Flowchart of the TLBO algorithm[19]

Metaheuristic algorithms such as TLBO are often used to minimize objective functions associated with the problem. The objective function used in this study is obtained by subtracting the calculated voltage drop from the desired voltage drop and is given in Equation 7.

$$OF = \min(abs(\%e_{demanded} - \%e_{calculated})) \quad (7)$$



The reason for subtracting the calculated voltage drop from the desired voltage drop is to force the objective function of the TLBO algorithm to converge to zero, in other words, to force the calculated voltage drop to be equal to the desired voltage drop.

There is a constraint when minimizing the objective function. As mentioned before, when determining the conductor cross-section in distribution networks, the current carrying capacity of the conductor must be suitable for the network while ensuring the percentage voltage drop. The minimum objective function is valid if the cross-section of the conductor can meet the current drawn from that part of the line. The optimization constraint is given in equation 8.

$$I_{Line\_Part(i)} \leq I_{Conductor\_Line\_part(i)} \quad i = 1, \dots, N \tag{8}$$

### III. RESULTS

The tool's accuracy and dependability in optimizing conductor cross-sections were evaluated by validating it against established analytical models and empirical data. The outcomes showed good agreement between the software's outputs and those acquired using conventional techniques, demonstrating the TLBO algorithm's efficacy in conductor sizing optimization. The test of the tool designed in this study was performed by optimizing the conductor cross-sections of the sample distribution network in Figure 1. The cross-sections of the distribution network in Figure 1 are designed in such a way that the voltage drop does not exceed 5% at the end users fed from poles 24, 18, 5, 8, 11 and 12. It should be noted that the user should perform the optimization process for the longest and most loaded parts of the line from largest to smallest during optimization. Therefore, the longest and most loaded side, TR-24, was optimized first. Then TR-15, which is fed from the same segment and is relatively shorter and less loaded, was optimized. The other segments were optimized with the same logic. On the Excel screen, the optimization results between TR-24 are displayed in Figure 6.

	B	C	D	E	F	G	H	I	J	K
				Source	Line ---	Branch<:::	Line ---	Branch<:::	Line ---	Branch<:::
Pole numbers				Transforme	-----	2	-----	15	-----	24
Line lengths(L)					80		125		240	
N.of intermediate poles					1		2		5	
Branch Lengths						400		135		0
Industrial Load										
Line power d.(w/m)					120		120		120	
Branch power d.(w/m)						120		120		0
Total line loads(P)					117600		60000		28800	
Line currents					178.6748		91.16061		43.75709	
K values					2,315		2,315		3,678	
Moments					9024000		6562500		3456000	
$\%e_s=10^{-7} \cdot K.L.P$			4,879392		2,089056		1,519219		1,271117	
delta V=			10,73466		4,595923		3,342281		2,796457	

Figure 6. TR – Pole 24 conductor cross section optimization results

Upon closer inspection of Figure 6, it is understood from the K values TR-2(2.315), 2-15(2.315), 15-24(3.678) and help of Table 1 that the conductors optimized by the TLBO algorithm are TR-2(Philox), 2-15(Philox) and 15-24(Poppy). With these conductors, it is seen that the voltage drop is 4.879 %, below 5% and they can easily carry the currents drawn from the relevant line segments when the current carrying capacities are considered in Table 1.

B	C	D	E	F	G	H	I	J	K
			Source	Line ---	Branch<:::	Line ---	Branch<:::	Line ---	Branch<:::
Pole numbers			15	-----	18	-----		-----	
Line lengths(L)				135		0		0	
N.of intermediate poles				2		0		0	
Branch Lengths					0		0		0
Industrial Load									
Line power d.(w/m)				120		0		0	
Branch power d.(w/m)					0		0		0
Total line loads(P)				16200		0		0	
Line currents				24.61337		0		0	
K values				9.308		0		0	
Moments				1093500		0		0	
$\%e_s=10^{-7}$ .K.L.P delta V=		1.01783		1.01783		0		0	
		2.239226		2.239226		0		0	

Figure 7. TR – Pole 18 conductor cross section optimization results

For the section of the line between TR and the last pole numbered 18, the cross-sectional calculation was made only between 15-18. Because TR-15 was determined in the previous step. Therefore, in this step, the voltage drop is taken as (5-voltage drop in the previous section), not 5 %. There is a total voltage drop of 3.608 % between TR-15, 2.089 % between TR-2 and 1.519 % between 2-15. Therefore, there should be a maximum voltage drop of 5-3.608=1.392 % between 15-18. When Figure 7 is analyzed, Rose conductor with a K value of 9.308 was selected by TLBO for the 15-18 range. When Rose conductor is used in this section, both the voltage drop does not exceed 1.392 % and the current drawn from this section of the line can be easily carried.

B	C	D	E	F	G	H	I	J	K
			Source	Line ---	Branch<:::	Line ---	Branch<:::	Line ---	Branch<:::
Pole numbers			2	-----	5	-----		-----	
Line lengths(L)				130		0		0	
N.of intermediate poles				1		0		0	
Branch Lengths					0		0		0
Industrial Load									
Line power d.(w/m)				120		0		0	
Branch power d.(w/m)					0		0		0
Total line loads(P)				15600		0		0	
Line currents				23.70176		0		0	
K values				9.308		0		0	
Moments				1014000		0		0	
$\%e_s=10^{-7}$ .K.L.P delta V=		0.943831		0.943831		0		0	
		2.076429		2.076429		0		0	

Figure 8. TR – Pole 5 conductor cross section optimization results

For the section of the line between TR and the last pole numbered 5, the cross-sectional calculation was made only between 2-5. Because TR-2 was determined in the first step. Therefore, in this step, the voltage drop is taken as (5-voltage drop in the previous section), not 5 %. There is a total voltage drop of 2.089 % between TR-2. Therefore, there should be a maximum voltage drop of 5-2.089=2.911 % between 2-5. When Figure 8 is analyzed, Rose conductor with a K value of 9.308 was selected by TLBO for the 2-5 range. When Rose conductor is used in this section, both the voltage drop does not exceed 2.911 % and the current drawn from this section of the line can be easily carried.

B	C	D	E	F	G	H	I	J	K
			Source	Line ---	Branch<:::	Line ---	Branch<:::	Line ---	Branch<:::
Pole numbers			2	-----	7	-----	10	-----	12
Line lengths(L)				80		80		40	
N.of intermediate poles				1		1		0	
Branch Lengths					40		30		0
Industrial Load									
Line power d.(w/m)				120		120		120	
Branch power d.(w/m)					120		120		0
Total line loads(P)				32400		18000		4800	
Line currents				49.22673		27.34818		7.292849	
K values				7.38		9.308		9.308	
Moments				2208000		1056000		192000	
$\%e_{\Delta V} = 10^{-7} \cdot K.L.P$		2.791142		1.629504		0.982925		0.178714	
delta V=		6.140513		3.584909		2.162435		0.39317	

Figure 9. TR – Pole 12 conductor cross section optimization results

For the section of the line between TR and the last pole numbered 12, the cross-sectional calculation was made only between 2-12. Because TR-2 was determined in the first step. Therefore, in this step, the voltage drop is taken as (5-voltage drop in the previous section), not 5 %. There is a total voltage drop of 2.089 % between TR-2. Therefore, there should be a maximum voltage drop of 5-2.089=2.911 % between 2-12. When Figure 9 is examined, it is understood from the K values 2-7(7.38), 7-10(9.308), 10-12(9.308) and help of Table I that the conductors optimized by the TLBO algorithm are 2-7(Lily), 7-10(Rose) and 10-12(Rose). With these conductors, it is seen that the voltage drop is 2.791 %, below 2.911 % and they can easily carry the currents drawn from the relevant line segments when the current carrying capacities are considered in Table I.

Due to the very short sections, the Excel screens for pole sides 8 and 11 were not included in the study due to repetition. TLBO determined the voltage drop between 7-8 as 0.178 % and the conductor as Rose. TLBO determined the voltage drop between 10-11 as 0.100 % and the conductor as Rose. The results are presented in Table II with all results.

Table II. Overall results of the optimization work

Pole 24 side	Poles →	TR	2	15	24	
	Total %e→	%e=2.089		%e=3.608	%e=4.879<5	
Pole 18 side	Poles →	TR	2	15	18	
	Total %e→	%e=2.089		%e=3.608	%e=4.625<5	
Pole 5 side	Poles →	TR	2	5		
	Total %e→	%e=2.089		%e=3.032<5		
Pole 12 side	Poles →	TR	2	7	10	12
	Total %e→	%e=2.089		%e=3.718	%e=4,700	%e=4,878<5
Pole 11 side	Poles →	TR	2	7	10	11
	Total %e→	%e=2.089		%e=3.718	%e=4,700	%e=4.800<5
Pole 8 side	Poles →	TR	2	7	8	
	Total %e→	%e=2.089		%e=3.718	%e=3,896<5	

Table II shows that the TLBO algorithm has successfully selected conductors for all parts of the sample distribution network without exceeding the desired voltage drop, taking into account the current carrying capacity of the conductors.

Tool's practical utility in optimizing conductor cross-sections for electrical distribution systems show valuable performance in terms of computational efficiency, accuracy, and ease of use. All things considered, the findings in this section show how the software tool can be used to optimize conductor cross-section using the TLBO algorithm, thereby increasing the efficiency of electrical distribution systems.

#### IV. DISCUSSION

Although conductor cross-section optimization has advanced significantly with the tool, there is still room for improvement and new uses. In distribution networks, the TLBO algorithm has shown to be a reliable technique for conductor size optimization. The capacity of TLBO to manage the complex structure of distribution networks with multiple branches and sections is demonstrated by this study. The findings suggest that by utilizing its teaching and learning phases, which emulate the educational process, TLBO can effectively traverse the vast and intricate search space. This enables the algorithm to efficiently converge to an optimal or nearly optimal solution, even within a problem space with a high dimension. The inclusion of constraints on percent voltage drop and maximum current carrying capacity in the optimization process is a crucial component of this research. These limitations guarantee that the chosen conductor sizes satisfy the network's operational requirements while also optimizing material and energy costs. Through strict adherence to these limitations, the methodology guarantees the electrical distribution system's dependability and safety by preserving voltage levels within reasonable bounds and averting conductor overloading or overheating.

The optimization algorithm's search space is greatly reduced by pre-calculating currents derived from line segments. This preprocessing step is essential because it lowers the computational load on the TLBO algorithm and concentrates the search on workable solutions, which improves algorithm efficiency. This novel method makes evident how crucial domain-specific expertise is to enhancing algorithmic performance and offers a direct route for real-world application. The suggested tool's usefulness and accessibility are demonstrated by the way it manages the optimization process and applies the TLBO algorithm using MATLAB and Excel. The data handling prowess of Excel and the computational capabilities of MATLAB come together to produce a potent tool that practitioners can use with ease. Because of its hybrid design, the tool is guaranteed to be both powerful and easy to use, which makes it appropriate for practical uses in electrical distribution system design and optimization. Future developments might include expanding the software's functionality to handle other aspects of distribution system design and operation, integrating more computational tools and algorithms, and incorporating sophisticated modeling techniques for transient analysis and dynamic simulations.

#### V. CONCLUSION

This study presents a new tool that maximizes electrical distribution system efficiency by selecting the right conductor cross-section. The tool gives engineers a strong yet intuitive platform for performing cross-section analysis, facilitating educated decision-making and ultimately enhancing system performance and reliability. It does this by combining the strengths of MATLAB and Excel. To sum up, the instrument signifies a noteworthy progression in the domain of electrical distribution system design, providing engineers with an invaluable tool for enhancing conductor cross-sections and augmenting system dependability and efficiency. Collaboration, innovation, and adoption are encouraged by this approach, which has the potential to accelerate the development of a more resilient and sustainable energy infrastructure.

#### STATEMENT OF CONTRIBUTION RATE

1st author contributed 100%

#### CONFLICTS OF INTEREST

They reported that there was no conflict of interest between the authors and their respective institutions.

#### RESEARCH AND PUBLICATION ETHICS

In the studies carried out within the scope of this article, the rules of research and publication ethics were followed.

#### REFERENCES

- [1] Z. Wang, H. Liu, D. C. Yu, X. Wang, and H. Song, "A practical approach to the conductor size selection in planning radial distribution systems," *IEEE Trans. Power Deliv.*, vol. 15, no. 1, pp. 350–354, 2000, doi: 10.1109/61.847272.
- [2] S. Sivanagaraju, N. Sreenivasulu, M. Vijayakumar, and T. Ramana, "Optimal conductor selection for radial distribution systems," *Electr. Power Syst. Res.*, vol. 63, no. 2, pp. 95–103, 2002, doi: 10.1016/S0378-7796(02)00081-0.

- 
- [3] L. A. Gallego Pareja, J. M. López-Lezama, and O. Gómez Carmona, "A MILP Model for Optimal Conductor Selection and Capacitor Banks Placement in Primary Distribution Systems," *Energies*, vol. 16, no. 11, pp. 1–21, 2023, doi: 10.3390/en16114340.
- [4] D. Joshi, S. Burada, and K. D. Mistry, "Distribution system planning with optimal conductor selection," *2017 Recent Dev. Control. Autom. Power Eng. RDCAPE 2017*, vol. 3, pp. 263–268, 2018, doi: 10.1109/RDCAPE.2017.8358279.
- [5] M. Ramalinga Raju, K. V. S. Ramachandra Murthy, K. Ravindra, and R. Srinivasa Rao, "Optimal conductor selection for agricultural distribution system - A case study," *2010 Int. Conf. Intell. Adv. Syst. ICIAS 2010*, pp. 1–6, 2010, doi: 10.1109/ICIAS.2010.5716178.
- [6] R. Ranjan, B. Venkatesh, and D. Das, "Optimal conductor selection of radial distribution networks using fuzzy adaptation of evolutionary programming," *Int. J. Power Energy Syst.*, vol. 26, no. 3, pp. 226–232, 2006, doi: 10.2316/journal.203.2006.3.203-3444.
- [7] M. Kumari, V. R. Singh, and R. Ranjan, "Optimal selection of conductor in RDS considering weather condition," *2018 Int. Conf. Comput. Power Commun. Technol. GUCON 2018*, pp. 647–651, 2019, doi: 10.1109/GUCON.2018.8675051.
- [8] M. Waseem, R. Khan, M. Zakria, S. Jamal, and S. Perveen, "Optimized Cable Sizing-An Economical Approach to Energy Saving with Reduced Power Loss," *4th Int. Conf. Power Gener. Syst. Renew. Energy Technol. PGSRET 2018*, no. September, pp. 1–4, 2019, doi: 10.1109/PGSRET.2018.8685987.
- [9] F. Mendoza, D. Requena, J. L. Bemal-Agustín, and J. A. Domínguez-Navarro, "Optimal conductor size selection in radial power distribution systems using evolutionary strategies," *2006 IEEE PES Transm. Distrib. Conf. Expo. Lat. Am. TDC'06*, 2006, doi: 10.1109/TDCLA.2006.311451.
- [10] S. Sivanagaraju and J. V. Rao, "Optimal conductor selection in radial distribution system using discrete Particle Swarm Optimization," *UK World J. Model. Simul.*, vol. 1, no. 3, pp. 183–191, 2009.
- [11] R. Srinivasa Rao, "Optimal Conductor Selection For Loss Reduction In Radial Distribution Systems Using Differential Evolution," *Int. J. Eng. Sci. Technol.*, vol. 2, no. 7, pp. 2829–2838, 2010.
- [12] M. M. Legha, F. Ostovar, and M. M. Legha, "Combination of Optimal Conductor Selection and Capacitor Placement in Radial Distribution Systems Using PSO Method," *Iraq J. Electr. Electron. Eng.*, vol. 10, no. 1, pp. 33–41, 2014, doi: 10.33762/EEEJ.2014.93016.
- [13] P. Samal, S. Mohanty, and S. Ganguly, "Simultaneous capacitor allocation and conductor sizing in unbalanced radial distribution systems using differential evolution algorithm," *2016 Natl. Power Syst. Conf. NPSC 2016*, Feb. 2017, doi: 10.1109/NPSC.2016.7858853.
- [14] H. Samet and M. M. Legha, "Optimal Conductor Selection in radial Distribution Using Imperialism Competitive Algorithm and Comparison with PSO," *6th Int. Conf. from "Scientific to Comput. Eng.*, no. July, pp. 1–9, 2014.
- [15] T. M. Khalil and A. V. Gorpnich, "Optimal conductor selection and capacitor placement for loss reduction of radial distribution systems by selective particle swarm optimization," *Proc. - ICCES 2012 2012 Int. Conf. Comput. Eng. Syst.*, pp. 215–220, 2012, doi: 10.1109/ICCES.2012.6408516.
- [16] A. Y. Abdelaziz and A. Fathy, "A novel approach based on crow search algorithm for optimal selection of conductor size in radial distribution networks," *Eng. Sci. Technol. an Int. J.*, vol. 20, no. 2, pp. 391–402, 2017, doi: 10.1016/j.jestch.2017.02.004.
- [17] J. F. Martínez-Gil, N. A. Moyano-García, O. D. Montoya, and J. A. Alarcon-Villamil, "Optimal selection of conductors in three-phase distribution networks using a discrete version of the vortex search algorithm," *Computation*, vol. 9, no. 7, 2021, doi: 10.3390/computation9070080.
- [18] G. Bayrak, "Elektrik Tesis Projesi Ders Notları." Accessed: Mar. 18, 2024. [Online]. Available: <https://docplayer.biz.tr/4552727-Elektrik-tesis-projesi.html>
- [19] R. V. Rao, V. J. Savsani, and D. P. Vakharia, "Teaching-learning-based optimization: A novel method for constrained mechanical design optimization problems," *CAD Comput. Aided Des.*, vol. 43, no. 3, pp. 303–315, 2011, doi: 10.1016/j.cad.2010.12.015.





## RESEARCH ARTICLE

# Impedance Controller Design and Dynamic Solution of The Manipulandum

\*<sup>1</sup>Yaşar Yıldırım, <sup>1</sup>Babek Naseri, <sup>2</sup>Amir Nobahar and <sup>3</sup>Reşat Özgür Doruk

\*Atılım University, Graduate School of Natural and Applied Sciences, Department of MODES, Ankara, Türkiye  
[yasaryildiran@gmail.com](mailto:yasaryildiran@gmail.com), [Orcid.0009-0003-2963-9203](https://orcid.org/0009-0003-2963-9203)

<sup>1</sup>Atılım University, School of Engineering, Mechatronics Engineering Department, Ankara, Türkiye  
[babek.naseri@atilim.edu.tr](mailto:babek.naseri@atilim.edu.tr), [Orcid.0000-0001-6007-3875](https://orcid.org/0000-0001-6007-3875)

<sup>2</sup>Atılım University, School of Engineering, Mechatronics Engineering Department, Ankara, Türkiye  
[amir.nsnam@atilim.edu.tr](mailto:amir.nsnam@atilim.edu.tr), [Orcid.0000-0002-8248-4963](https://orcid.org/0000-0002-8248-4963)

<sup>3</sup>Atılım University, School of Engineering, Electrical-Electronics Engineering Department, Ankara, Türkiye  
[resat.doruk@atilim.edu.tr](mailto:resat.doruk@atilim.edu.tr), [Orcid.0000-0002-9217-0845](https://orcid.org/0000-0002-9217-0845)

**Citation:**

Yıldırım, Y., Naseri, B., Nobahar, A., Doruk, R.Ö. (2024). *Impedance Controller Design and Dynamic Solution of The Manipulandum*, Journal of Science, Technology and Engineering Research, 5(1):54-67. DOI: 10.53525/jster.1475764

**Article Info**

Received : 30 April 2024

Accepted : 28 May 2024

**DOI:**

10.53525/jster.1475764

**\*Corresponding Author:**

Yaşar Yıldırım  
[yasaryildiran@gmail.com](mailto:yasaryildiran@gmail.com)  
 Phone: +90 533 634 0330

**ABSTRACT**

*This article explains the dynamic solution of the manipulandum that interact with the human upper arm, controller design, model simulation and simulation results. Manipulandum design are used in human-machine interaction experiments to understand human motor learning skills. Experimental design is the subject of the field of medicine, appropriate manipulandum design is the subject of the engineering field. In this article, the engineering qualities of the device were evaluated, its mathematical model obtained, dynamic model simulation made and control elements were examined, but the experimental use of this device, which is serve medical science were not discussed in this context. Most manipulandum in the literature have a 2-dof, 5-link closed chain structure that moves in the horizontal plane, their movement is provided by 2 actuators, their interaction with the human upper arm is made with a fixed joystick (end-effector) on the 2nd link, and their dimensions are smooth and compatible with the human upper arm. It is understood that the manipulandum must be of a size that can safely interact with the human arm. In this study a conceptual design was made for the manipulandum and the movement parameters of the manipulandum were obtained by creating a kinematic model accordingly. While creating the dynamic model of the system; It is accepted that the manipulandum moves in the horizontal plane, therefore there is no effect of gravity, there is no spring, damper or similar potential energy source in the system, and there is heat loss due to friction. The dynamic model obtained with the Euler Lagrange Method (ELM) was compared with the system model obtained with the Simulink Simscape Multibody (SSM) tool in the Simulink environment; The consistency of model parameters (friction coefficients, moment of inertia, etc.) was mutually checked. Since human-manipulandum interaction requires force control, an impedance controller has been designed for the system dynamics, instead of classical controllers. The success of the controller on both the ELM dynamic model and the SSM dynamic model were examined and the results were evaluated. As a result of the simulations; It is understood that in order to achieve meaningful position and force control, there must be a proportional magnitude relationship between the torques applied to the model by the actuators and the force applied to the end-effector.*

**Keywords:** Manipulandum, Haptic Device, System Dynamics, Impedance Controller

## I. INTRODUCTION

Motor behavior examines the ability to perform the movement at the optimum level. Motor learning is defined as the acquisition of motor skills and permanent improvement in performance. To master or adapt to a motor skill, a behavior must be repeated over and over. Today, robotic manipulandum's are frequently used in applied experiments to understand motor learning. Robotic manipulandum's are in a structure that moves in a planar surface, in a close chain structure, interacting with the subject via a joystick at the end-effector.

Manipulandum produce physical feedback to user. Their interface has to be ensured with physical interaction. With this properties manipulandum, they are preferable as robotic training devices for upper limb training for stroke rehabilitation. Compared to conventional therapies, these training devices have the advantage that they allow a self-controlled increase in training intensity and frequency as well as the opportunity to train independently [1].

In the literature Howard et al. used the vBOT planar robotic manipulandum to investigate whether the actions performed are independent of the last state in motor memory [2]. Again Howard et al.; used vBOT to investigate the effects of lead-in movement on motor memory formation. In their experiments, they observed that the active lead-in movement provided by vBOT reduced motor adaptation [3]. In their article Gomi and Kawato discussed a method aimed at measuring upper arm stiffness during movement. For this purpose, they developed a manipulandum in parallel link structure that can test both arms at the same time [4]. Kinarm End-Point is a commercial manipulandum used by clinical researchers to understand the effects of various neurological injuries and diseases. The Kinarm End-Point manipulandum is a stiff, graspable robot that can create highly complex mechanical environments [5]. With these features, it allows researchers to collect large amounts of valuable data in understanding brain functions and nervous system in studies conducted with healthy individuals. More than 200 publications have been made in this field using Kinarm End-Point [5]. Klein et al. described the 3-dof redundant motor control interface, its design features and the experimental results on a subject in their publications. Manipulandum also has an unusual wrist motor [6]. In the publications of Kostic and Popovic; a manipulandum without an actuator that moved freely in the horizontal plane was used. During the experiment, data was collected through the trace of the magnetic mouse attached to the End-effector on the Wacom Intuos4 plane. The subject's point to point movement was evaluated [7]. In their publication, Fong et al. designed a manipulandum with transparency and gravity compensation features to be used in upper-limb rehabilitation [8]. In their publications, Ueyama and Miyashita used a manipulandum called RANARM to estimate the limp stiffness of the monkey they chose as a subject [9]. In their publication, Cai and colleagues shared the features and first experiment of the dual-arm manipulandum they developed for use in the physical therapy of stroke patients. Dual-Arm Rehabilitation Robot (DARR) is designed to work synchronously with two 3-dof robotic arms attached to the subject's arm, one on the upper arm and the other on the lower arm [10]. Khanh Tran Nguyen and Hoang Dung Nguyen shared the features of the 1 dof dual manipulandum, which they designed to be used in the physical therapy of post-stroke patients, in their publications [11]. In their publications, Asgari and Crouch created a simulation model to estimate human upper arm impedance. The success of the study is the physical interaction with both the manipulandum model and the human model created through OpenSim in the simulation environment [12]. Vlugt et al. studied the mechanical properties of the human arm, which acts in harmony with a haptic device. Their 2003 article describe the design and application of the haptic device. They predicted that the deviation in position could be recorded as a result of the irregularity in the force, thus estimating the human endpoint admittance [13].

Literature shows that engineering and medical sciences are in a solid relationship in the design and use of manipulandum. Manipulandum have two main uses. The first is to investigate motor learning skills on healthy individuals, and the other is to use it as an auxiliary tool in the physical therapy of disabled individuals. With this study, it is aimed to complete the engineering design of a concept manipulandum that will serve to investigate motor learning skills on healthy individuals. First, a concept model of a manipulandum that will interact with the human upper arm is designed in the scope of the article. The study also includes obtaining the mathematical model (kinematic and dynamic model) for the two-axis five-bar

manipulandum, selecting and designing the controller, simulating the success of the controllers, and evaluating the simulation results.

## II. MATERIALS AND METHODS

### II.1. KINEMATIC MODEL

First of all, the notations of the two DOF five-bar planar manipulandum mechanism should be defined. Figure-1 shows the kinematic parameters on the manipulandum concept design. Manipulandum consists of five links, one fixed frame and four movable links, and five revolute joints connecting these links.  $L_i$  moving link lengths (in meters) as  $i=1,2,3,4,5$ ,  $\theta_i$  represent the angles (in radians) of the links counterclockwise with the X-axis. Links  $L_1$  and  $L_2$  are connected to the fixed frame by two overlapping revolute joints at  $X_0, Y_0$  coordinates. The angular changes in  $L_1$  and  $L_2$  are both measured counterclockwise with respect to the X-axis and are defined by  $\theta_1$  and  $\theta_2$ , respectively. These two revolute joints are the active revolute joints of the system.  $L_3$ - $L_1$  and  $L_4$ - $L_2$  links are connected to each other by passive revolute joints and the angular change in these two passive revolute joints are defined by  $\theta_3$  and  $\theta_4$ , respectively. The closed chain structure of the manipulandum, the overlap of the  $L_1$  and  $L_2$  links at the  $X_0, Y_0$  point, the selection of the  $L_1$ - $L_4$  and  $L_2$ - $L_3$  links of equal length, allows the structure to turn into a parallelogram, which provides an easy solution of the mathematical model. The  $L_5$  link is fixedly connected to the  $L_4$  link in the same direction, and it is connected to the  $L_3$  link with a passive revolute joint. The kinematic model of the system drive according to these parameters.

Manipulandum motion states (position, velocity, acceleration) are obtained by constructing the kinematic model. Kinematic model must accurately represent every position and movement within the working area of the manipulandum. The expectation from the Manipulandum kinematic model is that it provides the relationship between  $\theta_1$  and  $\theta_2$  entry angles and the end-effector cartesian coordinates.

$L_1$  and  $L_2$  are active links and their motions are independent. Therefore, the end-effector position equations from both branches should be written separately. However, due to choosing  $L_3$  and  $L_4$  link lengths as  $L_3=L_2$  and  $L_4=L_1$ ,  $\theta_3$  angle is equal  $\theta_2$  (in radians) and  $\theta_4$  angle is equal  $\theta_1$  angle (in radians), respectively. In future formulations, the equivalents of  $L_3, L_4, \theta_3$  and  $\theta_4$  will be used instead.

$$x = (L_1 + L_5). \cos\theta_1 + L_2. \cos\theta_2 \quad (1)$$

$$y = (L_1 + L_5). \sin\theta_1 + L_2. \sin\theta_2 \quad (2)$$

For real-time control of the manipulandum, it is also necessary to obtain the inverse kinematics equations. Craig gives some inverse kinematic solutions in chapter 4 of Introduction to Robotics Mechanics and Control book [14]. The sum of the squares of equations (1) and (2) is the equation (3).

$$x. \cos\theta_2 + y. \sin\theta_2 = \frac{(x^2+y^2)+L_2^2-(L_1+L_5)^2}{2.L_2} \quad (3)$$

Craig suggested that at appendix C that, if equation (3) is transcendental form and right-hand side is constant, inverse kinematic solution for  $\theta_2$  will be equation (4).

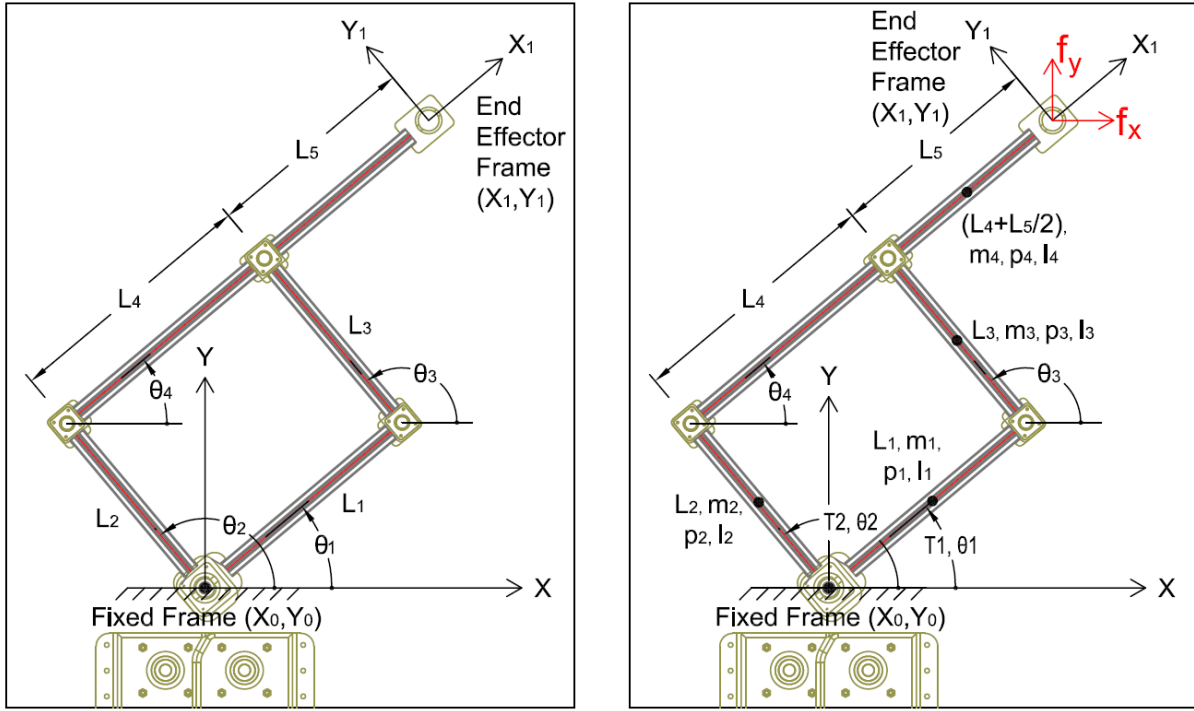


**Figure. 1.(a)** Two-DOF Five-bar Planar Manipulandum Kinematic Parameters, **Figure. 1.(b)** Two-DOF Five-bar Planar Manipulandum Dynamic Parameters.

$$\theta_2 = \arctan \frac{y}{x} \pm \arctan \left( \frac{\sqrt{x^2 + y^2 - \frac{(x^2 + y^2) + L_2^2 - (L_1 + L_5)^2}{2 \cdot L_2}}}{\frac{(x^2 + y^2) + L_2^2 - (L_1 + L_5)^2}{2 \cdot L_2}} \right) \quad (4)$$

Similarly, if  $\cos \theta_1$  is let alone from equation (1), inverse kinematic solution for  $\theta_1$  will be equation (5).

$$\theta_1 = \arctan \left( \pm \frac{\frac{x - L_2 \cdot \cos \theta_2}{(L_1 + L_5)}}{\sqrt{1 - \left( \frac{x - L_2 \cdot \cos \theta_2}{(L_1 + L_5)} \right)^2}} \right) \quad (5)$$

So, system forward and inverse kinematics models are defined mathematically. With this way end-effector XY position can be describe according to  $\theta_2$  and  $\theta_1$ . Jacobian Matrix provides the relation between joint velocities & end-effector velocities of manipulandum. It can be obtained from equations (1) and (2).

$$\begin{bmatrix} x' \\ y' \end{bmatrix} = \begin{bmatrix} -(L_1 + L_5) \cdot \sin(\theta_1) & -L_2 \cdot \sin(\theta_2) \\ (L_1 + L_5) \cdot \cos(\theta_1) & L_2 \cdot \cos(\theta_2) \end{bmatrix} \begin{bmatrix} \theta_1' \\ \theta_2' \end{bmatrix} = J \cdot \theta' \quad (6)$$

## II.2. DYNAMICAL MODEL

The joint space dynamics of the human interacting manipulandum is defined by equation (7).

$$M(\theta) \cdot \theta'' + V(\theta, \theta') + g(\theta) = \tau + J(\theta)^T f \quad (7)$$

Here,  $M(\theta) \cdot \theta''$ ,  $V(\theta, \theta')$  and  $g(\theta)$  are the inertial matrix, centrifugal and coriolis forces, and the gravitational component, respectively. The position of the manipulandum in the joint space is defined by  $\theta = [\theta_1; \theta_2]$ , the actuator torque (N.m) vector is defined by  $\tau = [\tau_1; \tau_2]$ , the manipulandum Jacobian is defined by  $J(\theta)$ , and the force vector is defined by  $f = [f_x; f_y]$ , which is applied force (N) externally to the

end-effector. Since the manipulandum working area is a two-dimensional horizontal plane, the effect of gravity is neglected. Here  $f$  is the force, so modeling of the interacting human upper arm was not required, as it was measured by sensors in the joystick-shaped end-effector [15],[16],[17].

While creating the dynamic model of Manipulandum, the Euler-Lagrange method (ELM) was used. Energy components of the system; Kinetic energy  $T$ , dissipating energy  $D$  and potential energy  $U$  must be known. Since the Manipulandum has no movement on the vertical axis and there is no spring or similar element in the system to store energy, potential energy change in the system is assumed to be zero. It is accepted that the source of dissipating energy is the friction occurring at the joints and end-effector. For each link, the energy lost in the joints was calculated as  $(D_i = \frac{1}{2} \cdot C_i \cdot (\theta'_i - \theta'_{i-1})^2)$ , thus the total dissipating energy "D" was obtained. The derivative of the dissipating energy affecting the system is calculated for the joints, where "C<sub>i</sub>" is the friction coefficient it is given by equations (8) and (9).

$$\frac{\partial D}{\partial \theta'_1} = (C_1 + C_3 + C_4) \cdot \theta'_1 + (C_4 - C_3) \cdot \theta'_2 \quad (8)$$

$$\frac{\partial D}{\partial \theta'_2} = (C_2 + C_3 + C_4) \cdot \theta'_2 + (C_4 - C_3) \cdot \theta'_1 \quad (9)$$

The parameters used when calculating the kinetic energy "T<sub>i</sub>" of the system are; "L<sub>i</sub>" as the link length, "m<sub>i</sub>" as the link mass, "v<sub>i</sub>" as the center of mass linear velocity component, "p<sub>i</sub>" as the center of mass position, and "I<sub>i</sub>" as the link moment of inertia. Here "p<sub>4</sub>" is the center of mass that is assumed as the center of mass of the total mass of the "L<sub>1</sub>", "L<sub>5</sub>" links and the end-effector. The kinetic energy equation for each component are given by (10), (11), (12), and (13).

$$T_1 = \frac{1}{2} \cdot m_1 \cdot v_1^2 + \frac{1}{2} \cdot I_1 \cdot \theta_1'^2 \quad (10) \quad T_2 = \frac{1}{2} \cdot m_2 \cdot v_2^2 + \frac{1}{2} \cdot I_2 \cdot \theta_2'^2 \quad (11)$$

$$T_3 = \frac{1}{2} \cdot m_3 \cdot v_3^2 + \frac{1}{2} \cdot I_3 \cdot (\theta_2' - \theta_1')^2 \quad (12) \quad T_4 = \frac{1}{2} \cdot m_4 \cdot v_4^2 + \frac{1}{2} \cdot I_4 \cdot (\theta_2' + \theta_1')^2 \quad (13)$$

The Lagrangian of the system is calculated by taking  $L = T_{sum}(\theta, \theta') - U(\theta)$  and  $U(\theta) = 0$ . The Lagrangian of the system is given in equation (14).

$$L = \frac{1}{8} \cdot \zeta \cdot \theta_1'^2 + \frac{1}{8} \cdot \eta \cdot \theta_2'^2 + \frac{1}{8} \cdot \varepsilon \cdot \cos(\theta_2 - \theta_1) \cdot \theta_1' \cdot \theta_2' + (I_4 - I_3) \cdot \theta_1' \cdot \theta_2' \quad (14)$$

In the resulting Lagrangian, 3 parts consisting of constants are expressed as the parameters  $\zeta$ ,  $\eta$ ,  $\varepsilon$ , respectively and are given in equations (15), (16), (17).

$$\zeta = 2 \cdot (m_1 \cdot L_1^2 + 4 \cdot I_1) + 4 \cdot (m_3 \cdot L_1^2 + I_3) + 4 \cdot (m_4 \cdot (L_1 + L_5/2) + I_4) \quad (15)$$

$$\eta = (m_2 \cdot L_2^2 + 4 \cdot I_2) + (m_3 \cdot L_2^2 + 4 \cdot I_3) + 4 \cdot (m_4 \cdot L_2^2 + I_4) \quad (16)$$

$$\varepsilon = 4 \cdot m_3 \cdot L_1 \cdot L_2 + 8 \cdot m_4 \cdot L_2 \cdot (L_1 + L_5/2) \quad (17)$$

In conservative systems, Lagrange's equation of motion is given by (18) [Marion 1965].

$$\frac{d}{dt} \frac{\partial L}{\partial (\theta'_1, \theta'_2)} - \frac{\partial L}{\partial (\theta_1, \theta_2)} + \frac{\partial D}{\partial (\theta'_1, \theta'_2)} = (\tau_1, \tau_2) \quad (18)$$

$\theta_1$  and  $\theta_2$  are the joint angles (rad.).  $\tau_1$ ,  $\tau_2$  are torque (N.m) corresponding to the joint angles and D is dissipating energy (joules). We use Lagrange's equation to drive manipulandum dynamics.

$$\frac{d}{dt} \left( \frac{\partial L}{\partial \theta'_1} \right) = \frac{1}{4} \cdot \zeta \cdot \theta_1'' - \frac{1}{8} \cdot \varepsilon \cdot \sin(\theta_2 - \theta_1) \cdot (\theta_2' - \theta_1') \cdot \theta_2' + \left( \frac{1}{8} \cdot \varepsilon \cdot \cos(\theta_2 - \theta_1) + (I_4 - I_3) \right) \cdot \theta_2'' \quad (19)$$

$$\frac{\partial L}{\partial \theta_1} = \frac{1}{8} \cdot \varepsilon \cdot \sin(\theta_1 - \theta_2) \cdot \theta_1' \cdot \theta_2' \quad (20)$$



$$\frac{d}{dt} \left( \frac{\partial L}{\partial \theta'_2} \right) = \frac{1}{4} \cdot \eta \cdot \theta''_2 - \frac{1}{8} \cdot \varepsilon \cdot \sin(\theta_2 - \theta_1) \cdot (\theta'_2 - \theta'_1) \cdot \theta'_1 + \left( \frac{1}{8} \cdot \varepsilon \cdot \cos(\theta_2 - \theta_1) + (I_4 - I_3) \right) \cdot \theta''_1 \quad (21)$$

$$\frac{\partial L}{\partial \theta_2} = -\frac{1}{8} \cdot \varepsilon \cdot \sin(\theta_1 - \theta_2) \cdot \theta'_1 \cdot \theta'_2 \quad (22)$$

$$\tau = M(\theta) \cdot \theta'' + V(\theta, \theta') \quad (23)$$

$M(\theta)$  and  $V(\theta, \theta')$  are written in matrix form as in (24) and (25).

$$M(\theta) = \begin{bmatrix} \frac{1}{4} \cdot \zeta & \frac{1}{8} \cdot \varepsilon \cdot \cos(\theta_2 - \theta_1) + (I_4 - I_3) \\ \frac{1}{8} \cdot \varepsilon \cdot \cos(\theta_2 - \theta_1) + (I_4 - I_3) & \frac{1}{4} \cdot \eta \end{bmatrix} \cdot \begin{bmatrix} \theta''_1 \\ \theta''_2 \end{bmatrix} \quad (24)$$

$$V(\theta, \theta') = \begin{bmatrix} \frac{1}{8} \cdot \varepsilon \cdot \sin(\theta_2 - \theta_1) \cdot (2 \cdot \theta'_1 - \theta'_2) \cdot \theta'_2 + (C_1 + C_3 + C_4) \cdot \theta'_1 + (C_4 - C_3) \cdot \theta'_2 \\ \frac{1}{8} \cdot \varepsilon \cdot \sin(\theta_2 - \theta_1) \cdot (\theta'_1 - 2 \cdot \theta'_2) \cdot \theta'_1 + (C_2 + C_3 + C_4) \cdot \theta'_2 + (C_4 - C_3) \cdot \theta'_1 \end{bmatrix} \quad (25)$$

If we leave the  $\theta''$  expression alone in equation (7), we obtain the dynamic equation of the system depending on the torque and external force variables.

$$\theta'' = M(\theta)^{-1} (\tau - V(\theta, \theta') - J(\theta)^T f) \quad (26)$$

Before presenting the details of controller, the manipulandum 3D dynamic model created in Simulink Simscape Multibody (SSM) should also be mentioned. SSM allow the representation of all links, revolute joints, rotational and translational rigid transformations. Internal mechanic properties (stiffness, damping coefficient) are adjustable. Also, physical shape and material density of the links can be adjustable. Close chain structure, fixed frame relations, inputs and outputs of the platform can be seen on Figure-1.

### II.3. IMPEDANCE CONTROLLER

When it comes to human interaction, in addition to position control, the force applied to the end-effector should also be controlled. Impedance control; aims at the control of position and force by adjusting the mechanical impedance due to the external force applied by the person to the end-effector.

Mechanical impedance is related to the moving forces acting on a mechanical system. Mechanical impedance is defined by the rate of change of force acting on a body to the velocity generated by the same force [17],[18],[19].

In impedance control the operator motion is an input and the reaction force is fed back to the operator based on this input measurement. We also assume that the desired impedance of the body to the external force is expressed by,

$$m_d \cdot \theta'' + D_d \cdot (\theta' - \theta'_d) + K_d \cdot (\theta - \theta_d) = K_{fd} \cdot f \quad (27)$$

where  $m_d$ ,  $D_d$ ,  $K_d$  and  $K_{fd}$  are the desired inertia matrix, damping, stiffness and external force coefficient respectively, and  $\theta'_d = [\theta'_{d1}; \theta'_{d2}]$  (rad/s) and  $\theta_d = [\theta_{d1}; \theta_{d2}]$  (rad) are the desired velocity and position trajectories.

When  $\theta$ ,  $\theta'$  and  $\theta''$  are measurable, the control rule is that the torque is obtained by drawing it from the dynamic equation (7) and substituting it in the impedance equation (27). However, when the external force  $f$  is measurable, the control rule is obtained by drawing  $\theta''$  from the dynamic equation and substituting it in the impedance equation (27). Since no mass change is foreseen in the system, the original mass  $M(\theta)$  is considered equal to the desired inertia matrix  $m_d$ . Thus, simplified position and velocity feedback control rule is achieved:

$$\tau = \frac{M(\theta)}{m_d} \cdot D_d \cdot (\theta'_d - \theta') + \frac{M(\theta)}{m_d} \cdot K_p \cdot (\theta_d - \theta) + V(\theta, \theta') + J(\theta)^T f + \frac{M(\theta)}{m_d} \cdot K_{fd} \cdot f \quad (28)$$

### III. SIMULATION INFORMATION

The manipulandum, whose parameters are shown in Figure-1(a) and (b), was simulated in the Matlab/Simulink environment. First of all, the compatibility of the dynamic model obtained with ELM and the SSM dynamic model described in Section II.2 was examined. The parameter set for both models is given in Table-1. The parameters chosen for both models are different. Damping coefficient was given to the revolute joints to represent the frictions in the SSM dynamic model. On the other hand, in the ELM dynamic model, frictions are represented by the calculation of dissipating energy.

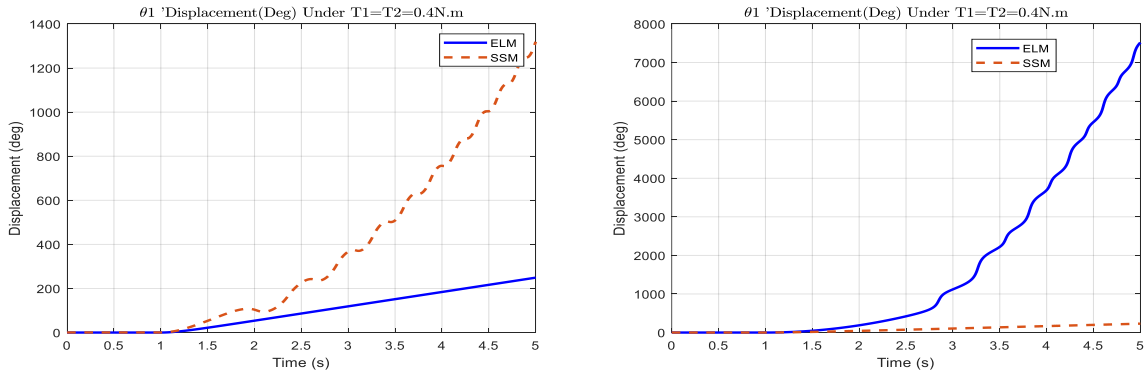
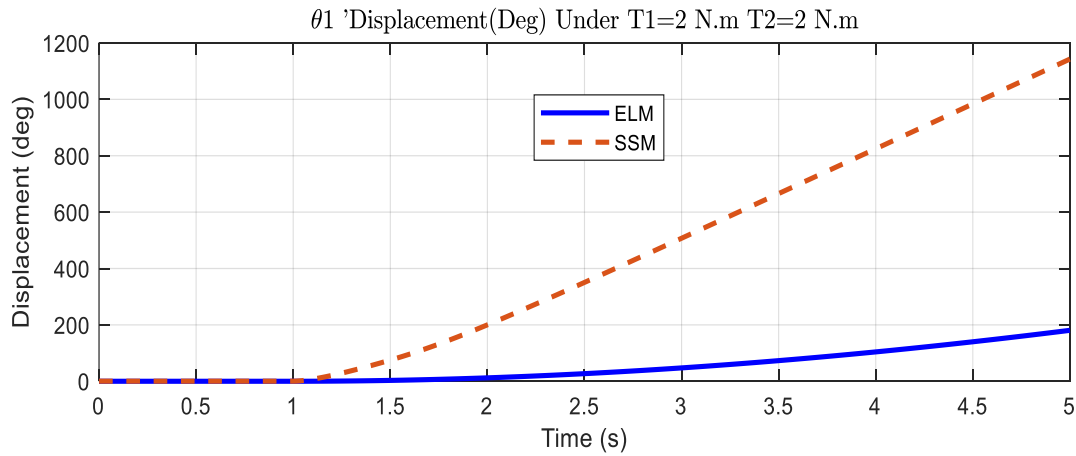


Figure. 2.(a, b)  $[\theta_1; \theta_2]$  displacement response under  $[\tau_1; \tau_2] = [0.4; 0.4]$  step input.

In Figure.2.(a), in the SSM dynamic model, the damping ratio value entered for the joints is taken as zero. In Figure.2.(b), in the ELM dynamic model, the friction coefficients “ $C_i$ ” used in the calculation of dissipating energy are taken as zero. Both dynamic models show similar behavior in the absence of coefficients chosen to represent friction.

In the SSM dynamic model, mass moment of inertia is automatically calculated from link dimensions and link weights. However, there were difficulties in calculating the mass moment of inertia in the ELM dynamic model, especially for the end-effector. Aluminum material was chosen for the links for both models. Accordingly, density=1475 kg/m<sup>3</sup> for half-hollow sigma profile. The center of gravity selected for L4+L5+End Effector in the ELM model may not be compatible with the SSM dynamic model. When the mass moment of inertia values used in the SSM dynamic model are applied to the ELM dynamic model, no meaningful results can be obtained (Figure.3).



**Figure 3.**  $\theta_1$  displacement response under  $[\tau_1; \tau_2] = [2; 2]$  step input.

**Table I.** Parameters for both dynamic model

Symbol	Description	ELM Dynamic Model Value SI	SSM Dynamic Model Value SI
$L_1=L_3$	Link Length	0.20 m	0.20 m
$L_2=L_4$	Link Length	0.40 m	0.40 m
$L_5$	Link Length	0.15 m	0.15 m
$m_1$	Link Weight	0.118 Kg	0.118 Kg
$m_2$	Link Weight	0.236 Kg	0.236 Kg
$m_3$	Link Weight	0.236 Kg	0.236 Kg
$m_4$	Link + End-effector Weight	0.506 Kg	0.506 Kg
$p_{1,2,3,4}$	Center of Mass point	Undefined	Undefined
$I_1$	Mass Moment of inertia of $L_1$	0.1 Kg.m <sup>2</sup>	$0.8 \cdot 10^{-5}$ Kg.m <sup>2</sup>
$I_2$	Mass Moment of inertia of $L_2$	0.5 Kg.m <sup>2</sup>	$1.6 \cdot 10^{-5}$ Kg.m <sup>2</sup>
$I_3$	Mass Moment of inertia of $L_3$	0.5 Kg.m <sup>2</sup>	$1.6 \cdot 10^{-5}$ Kg.m <sup>2</sup>
$I_4$	Mass Moment of inertia of $L_4 + L_5 + \text{End-effector}$	8 Kg.m <sup>2</sup>	$8.4 \cdot 10^{-5}$ Kg.m <sup>2</sup>
$C_1$	Friction Coefficient $L_1$	0.09 N.s/m	Undefined
$C_2$	Friction Coefficient $L_2$	0.09 N.s/m	Undefined
$C_3$	Friction Coefficient $L_3$	0.09 N.s/m	Undefined
$C_4$	Friction Coefficient $L_4 + L_5 + \text{End-effector}$	0.13 N.s/m	Undefined
$\zeta_1$	Damping ratio for $L_1$	Undefined	0.36 N.m/(rad/s)
$\zeta_2$	Damping ratio for $L_2$	Undefined	0.36 N.m/(rad/s)
$\zeta_3$	Damping ratio for $L_3$	Undefined	0.036 N.m/(rad/s)
$\zeta_4$	Damping ratio for $L_4 + L_5 + \text{End-effector}$	Undefined	0.036 N.m/(rad/s)

Both dynamic models are compared under two basic cases. In the first case, the torque step input value was entered at  $t=1s$  to represent the actuators connected to the manipulandum  $L_1$  and  $L_2$  active links, and the outputs are evaluated below.

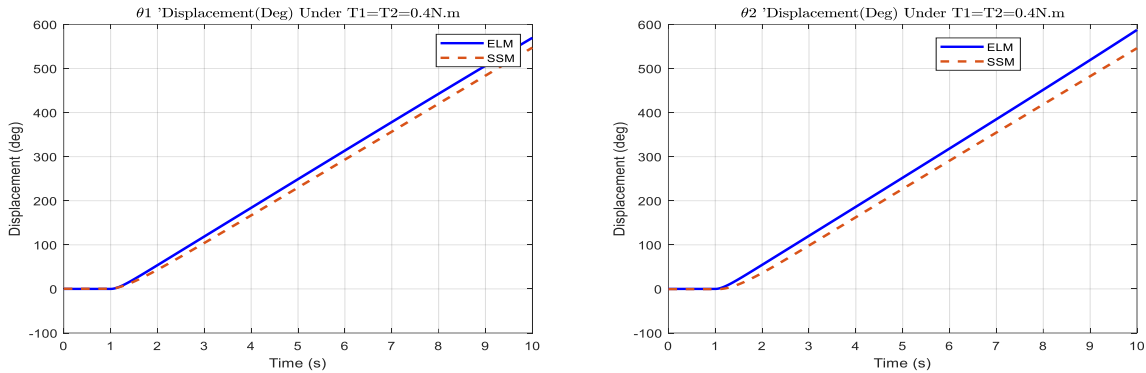


Figure. 4.(a, b)  $[\theta_1; \theta_2]$  displacement response under  $[\tau_1; \tau_2] = [0.4; 0.4]$  step input.

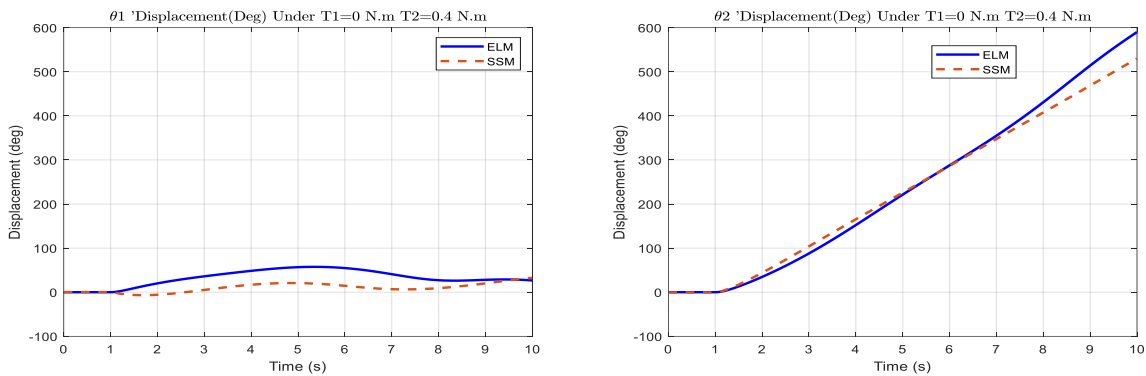


Figure. 5.(a, b)  $[\theta_1; \theta_2]$  displacement response under  $[\tau_1; \tau_2] = [0; 0.4]$  step input.

In accordance with the entered  $\tau_1$  and  $\tau_2$  torque input values, it is seen that  $\theta_1$  and  $\theta_2$  values increase in the same direction for both dynamic models during the simulation period (Figure.4. a, b). If the torque step input value entered for relevant actuator is zero, the connected link is not expected to move. However, as seen in figure.5.a, although the torque value entered for  $L_1$  is zero, movement is observed in  $\theta_1$ . These movements can be explained by the effect of the friction defined in the joints on other motionless links. In the second case, the force  $(f_x, f_y)$  step input value was entered at  $t=1s$  to represent the effect of the person's hand on the manipulandum end-effector, and the outputs are displayed below.

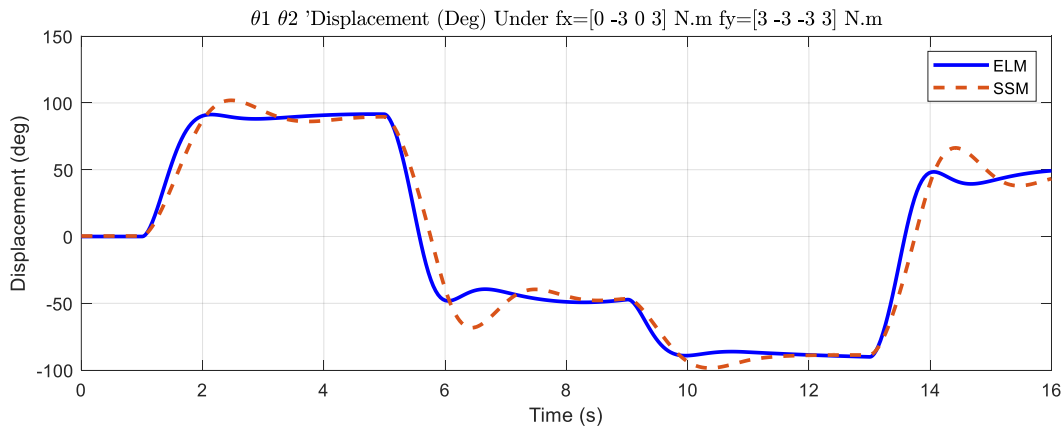
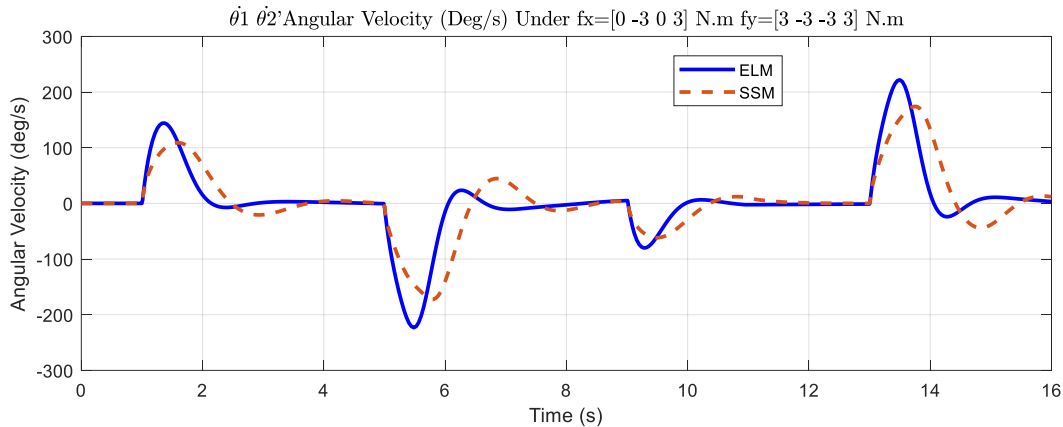


Figure. 6.  $[\theta_1; \theta_2]$  displacement response under  $[f_x] = [0 - 3 0 3]$ ,  $[f_y] = [3 - 3 - 3 3]$  step input.



**Figure 7.**  $[\theta'_1; \theta'_2]$  angular velocity response under  $[f_x] = [0 - 3 0 3]$ ,  $[f_y] = [3 - 3 - 3 3]$  step input.

In order to understand the effect of the step input force entered into the end-effector, a force of 3 Nm. was applied in different directions at different times  $t$ . The expectation is that the end-effector will position itself with the longest reach in the direction in which the force is entered. The system shows acceptable overshoot but behaves as expected.

After this evaluation of the dynamic model, controller simulation was started. The impedance controller explained in Section II.3 was tried to be applied to both dynamic models under the same conditions and with the same control coefficients.  $K_d$ ,  $D_d$  and  $K_{fd}$  coefficients were determined by trial-and-error method.

First, the relationship between actuator torque input and end-effector force input was examined with the simulation. The expectation is that the extremely high selected input value will dominate the other (Figure.8.a.b).



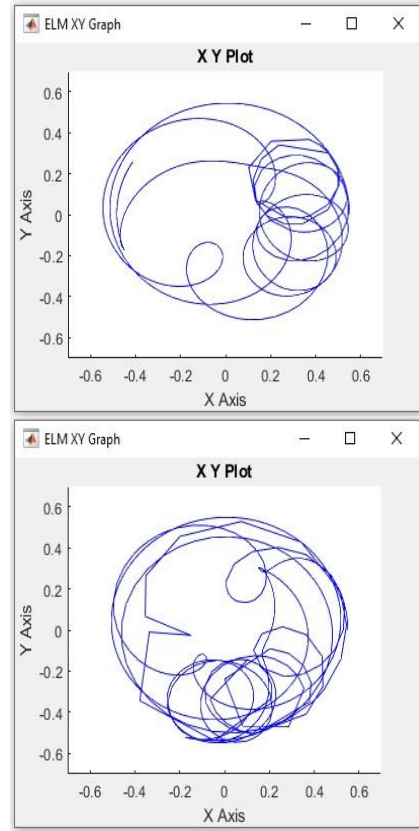
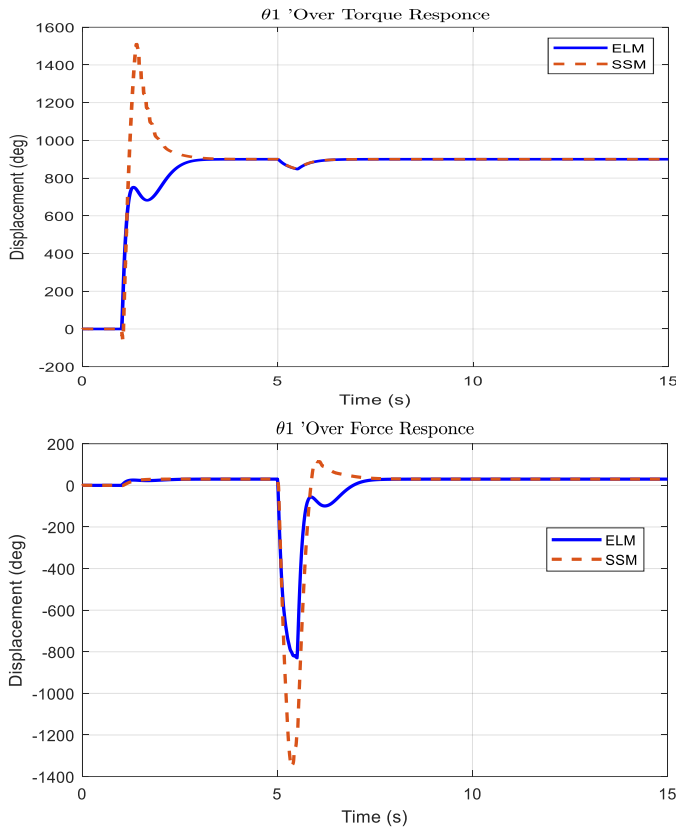


Figure. 8.(a) Over torque and over force responses.

Figure. 8.(b) XY Graphs for left site

As expected, a small  $D_d$  damping coefficient caused the system to be under-damped, while a high  $D_d$  damping coefficient caused the system to be over-damped (Figure.9).

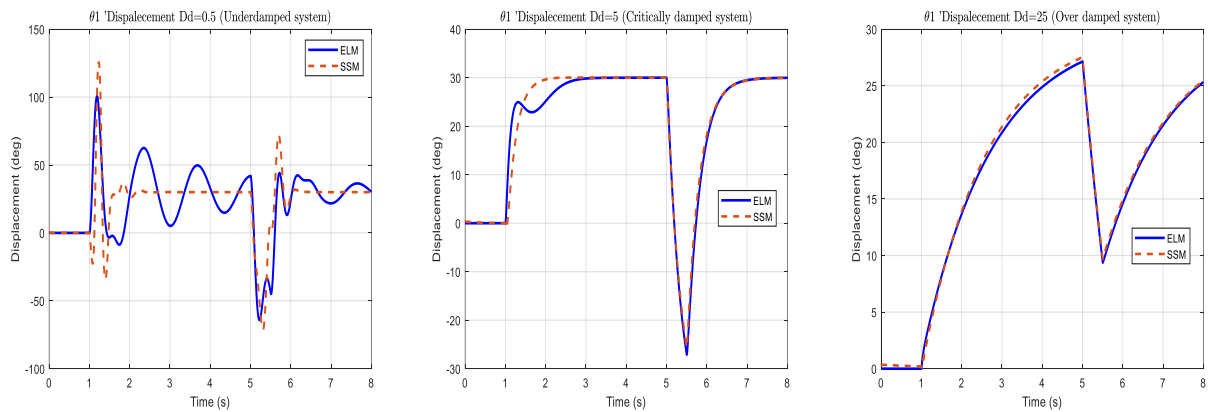
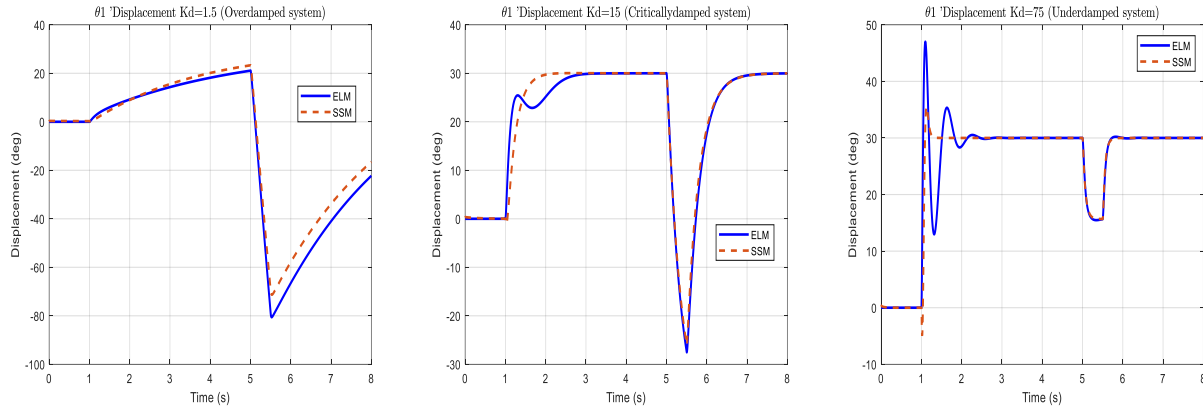


Figure. 9  $\theta_1 = 30^\circ$  displacement response under damping coefficient  $D_d=0.5$ ,  $D_d=5$ ,  $D_d=25$

Again, while a small  $K_d$  stiffness coefficient caused the system to be over-damped, a high  $K_d$  stiffness coefficient caused the system to be under-damped (Figure.10).



**Figure. 10**  $\theta_1 = 30^\circ$  displacement response under stiffness coefficient  $K_d=1.5$ ,  $K_d=15$ ,  $K_d=75$

Then, external force coefficients were tested with  $K_{fd} = (0.7, 7, 70)$  while the coefficients  $D_d = 4.89$  and  $K_d = 14.92$  were kept constant at their ideal values. It was observed that the force changed scalar in direct proportion to the change in the  $K_{fd}$  coefficient, but there was no deformation in the movement profile. Here  $F_{xy}$  force value and is accepted as the value read by the force sensors located in the manipulandum end-effector.  $[\theta_1; \theta_2] = [30^\circ; 140^\circ]$  step input was applied to the system at time  $t = [5; 7.5; 10; 12.5]$  (s), during  $Dt=0.5$  s, in  $\pm X$  and  $\pm Y$  directions, and the results are shared in figure.11.

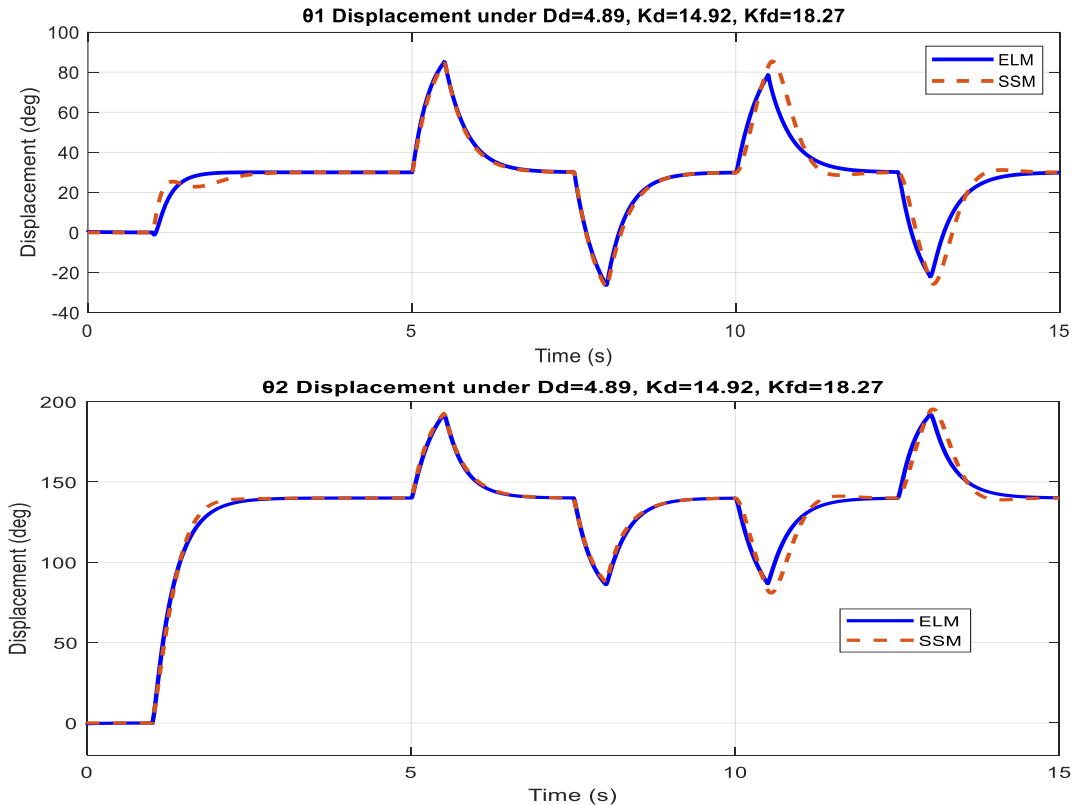


**Figure. 11**  $[\theta_1; \theta_2] = [30^\circ; 140^\circ]$  displacement during applied external force on  $\pm X$  and  $\pm Y$  directions

#### IV. DISCUSSION AND CONCLUSION

This study explains the dynamic solution of the manipulandum that interact with the human upper arm, controller design, model simulation and simulation results. Manipulandum design in this field are used in human-machine interaction experiments to understand human motor learning skills. While the subject of experiments is handled in the field of medicine, appropriate manipulandum design is the subject of the engineering field. In this study, the engineering qualities of the device were evaluated, its mathematical model obtained, dynamic model simulation done and control elements were examined. The manipulandum have a 2-dof, 5-link closed chain structure that moves in the horizontal plane, their movement is provided by 2 actuators, their interaction with the human upper arm is made with a fixed joystick (end-effector) on the 2nd link, their dimensions are smooth and compatible with the human upper arm. It is understood that the manipulandum must be of a size that can safely interact with the human arm. A conceptual design was made for the manipulandum and the movement parameters of the manipulandum were obtained by creating a kinematic model accordingly. While creating the dynamic model of the system; It is accepted that the manipulandum moves in the horizontal plane, therefore there is no effect of gravity, there is no spring, damper or similar potential energy source in the system, and there is heat loss due to friction. The dynamic model obtained with the ELM was compared with the system model obtained with the SSM tool in the Simulink environment; The consistency of model parameters (friction coefficients, moment of inertia, etc.) was mutually checked. Since human-manipulandum interaction requires force control, an impedance controller has been designed for the system dynamics, instead of classical controllers. The success of the controller on both the ELM dynamic model and the model created in SSM was examined and the results were evaluated.

Result of the simulations suggests that in order to achieve meaningful position and force control, there must be a proportional magnitude relationship between the torques applied to the model by the actuators and the force applied to the end-effector. If the actuator torques or end-effector forces are excessively greater than the other, the simulation results in two ways. In cases where the force is dominant, the manipulandum moves in unpredictable / unexpected trajectories around the origin. In the case where the torque is dominant, the manipulandum rotates around the origin until the end of the simulation period and its rotation is in the direction where the torque is dominant. This is an expected situation. Human-machine interaction safety and effectiveness are also mention in similar articles reviewed.

**Future work:** In this study, no working condition or working area restrictions were defined for the manipulandum. However, in a Manipulandum prototype it should be ensured that the links do not pass over each other (up & down link relationship). Links should be prevented from falling into cross positions. System workspace (boundary) must be defined. The system must be prevented from making a full rotation (360-degree rotation). This study was supported by Kafka Mechatronics Co. With this support, the manipulandum prototype was completed and the electronic components and software infrastructure for the actuators, drivers and controller were prepared. The results obtained from the experimental setup will also be shared in an article, and the entire study will be converted into a doctoral thesis and shared.

#### STATEMENT OF CONTRIBUTION RATE

Authors' contribution rates to the study are equal.

#### CONFLICTS OF INTEREST

They reported that there was no conflict of interest between the authors and their respective institutions.

#### RESEARCH AND PUBLICATION ETHICS

In the studies carried out within the scope of this article, the rules of research and publication ethics were followed.

**REFERENCES**

- [1] A. (Lex) E. Q. vanDelden, C. (Lieke) E. Peper, Gert Kwakkel, and Peter J. Beek, "A Systematic Review of Bilateral Upper Limb Training Devices for Poststroke Rehabilitation", Hindawi Publishing Corporation Stroke Research and Treatment, Volume 2012, Article ID 972069, 17 pages doi:10.1155/2012/972069
- [2] Ian S. Howard, James N. Ingram, David W. Franklin, \* and Daniel M. Wolpert\*, "Gone in 0.6 Seconds: The Encoding of Motor Memories Depends on Recent Sensorimotor States", The Journal of Neuroscience, September 12, 2012, 32(37):12756–12768
- [3] Ian S. Howard, Christopher Ford, Angelo Cangelosi & David W. Franklin, "Active lead-in variability affects motor memory formation and slows motor learning", <http://www.nature.com/scientificreports>, August 10, 2017
- [4] Hiroaki Gomi, Mitsuo Kawato, "Human arm stiffness and equilibrium-point trajectory during multi-joint movement", Biological Cybernetics, Biol. Cybern.76, 163-171 (1997)
- [5] BKIN Technologies Ltd. dba Kinarm., "Kinarm Tech End Point Lab", PN14332-1-Nov-21, [www.kinarm.com](http://www.kinarm.com) (accessed 24<sup>th</sup> May 2024)
- [6] Klein J., Roach N., and Burdet E., "3DOM: A 3 Degree of Freedom Manipulandum to Investigate Redundant Motor Control", IEEE Transactions On Haptics, Vol.7 No.2 April-June 2014
- [7] Kostic M. D., Popovic M. B., "Influence of Planar Manipulandum to the Hand Trajectory During Point to Point Movement", IEEE International Conference on Rehabilitation Robotics, ETH Zurich City, Switzerland, 2011
- [8] Fong J., Crocher V., Tan Y., Oetomo D., and Mareels I., "EMU: A Transparent 3D Robotic Manipulandum for Upper-limb Rehabilitation", International Conference on Rehabilitation Robotics (ICORR), QEII Centre, London, UK, July 17-20, 2017
- [9] Ueyama Y., and Miyashita E., "Optimal Feedback Control for Predicting Dynamic Stiffness During Arm Movement", IEEE Transactions on Industrial Electronics, Vol. 61, No.2, February 2014
- [10] Cai S., Wu W., and Xie L., "Dual-Arm Limb Rehabilitation Robot: Mechanism Design and Preliminary Experiments", 6<sup>th</sup> International Conference on Control, Automation and Robotics, 2020
- [11] Nguyen K. T., and Nguyen H. D., "Designing the Robot Arms for Upper Limb Recovery Movements of Post-Stroke Patients", 6<sup>th</sup> International Conference on Green Technology and Sustainable Development (GTSD), 2022
- [12] Asgari M., and Crouch D. L., "Estimating Human Upper Limb Impedance Parameters From a State-of-the-Art Computational Neuromusculoskeletal Model", 43<sup>rd</sup> Annual International Conference of the IEEE Engineering in Medicine & Biology Society (EMBC), Virtual Conference, Oct. 21 – Nov. 4, 2021
- [13] Erwin de Vlugt, Alfred C. Schouten, Frans C.T. van der Helm, Piet C. Teerhuis, Guido G. Brouwn, "A force-controlled planar haptic device for movement control analysis of the human arm", Journal of Neuroscience Methods 129 (2003) 151-168
- [14] John J. Craig, "Introduction to Robotics Mechanics and Control", Pearson Education 2018, Fourth Edition, Global Edition, ISBN 978-0-13-348979-8
- [15] F. C. Park and K. M. Lynch, "Introduction to Robotics Mechanics, Planning, and Control", Park and Lynch 16:36 September 20, 2016
- [16] Mark W. Spong, Seth Hutchinson, and M. Vidyasagar, "Robot Dynamics and Control" Second Edition, January 28, 2004
- [17] Frank L. Lewis, Darren M. Dawson, Chaouki T. Abdallah, "Robot Manipulator Control Theory and Practice", Second Edition, Revised and Expanded Copyright © 2004 by Marcel Dekker, Inc.
- [18] Bruno Siciliano, Lorenzo Sciavicco, Luigi Villani, Giuseppe Oriolo, "Robotics Modelling, Planning and Control", Springer-Verlag London Limited, 2009, DOI 10.1007/978-1-84628-642-1
- [19] Asif SŠabanovic, Kouhei Ohnishi., "Motion Control Systems", First Edition, Published 2011 by John Wiley & Sons (Asia) Pte Ltd. ISBN: 978-0-470-82573-0



## RESEARCH ARTICLE

## 2D Millimeter-Wave SAR Imaging with Automotive Radar

\*<sup>1</sup> Bengisu Yalcinkaya Gokdogan, <sup>1</sup> Remziye Busra Coruk, <sup>2</sup> Elif Aydin, and <sup>3</sup> Ali Kara\*Atilim University, Faculty of Engineering, Electrical and Electronics Engineering Department, Ankara, Turkey  
[bengisu.yalcinkaya@atilim.edu.tr](mailto:bengisu.yalcinkaya@atilim.edu.tr), [Orcid.0000-0003-3644-0692](https://orcid.org/0000-0003-3644-0692)<sup>1</sup>Atilim University, Faculty of Engineering, Electrical and Electronics Engineering Department, Ankara, Turkey  
[rbusratezel@gmail.com](mailto:rbusratezel@gmail.com), [Orcid.0000-0002-9466-3862](https://orcid.org/0000-0002-9466-3862)<sup>2</sup>Cankaya University, Faculty of Engineering, Electrical and Electronics Engineering Department, Ankara, Turkey  
[elif.aydin@cankaya.edu.tr](mailto:elif.aydin@cankaya.edu.tr), [Orcid.0000-0001-6878-1796](https://orcid.org/0000-0001-6878-1796)<sup>3</sup>Gazi University, Faculty of Engineering, Electrical and Electronics Engineering Department, Ankara, Turkey  
[akara@gazi.edu.tr](mailto:akara@gazi.edu.tr), [Orcid.0000-0002-9739-7619](https://orcid.org/0000-0002-9739-7619)**Citation:**Gokdogan, B.Y., Çoruk, R. B., Aydin, E., Kara, A. (2024) 2D Millimeter-Wave SAR Imaging with Automotive Radar, *Journal of Science, Technology and Engineering Research*, 5(1):68-77. DOI: 10.53525/jster.1456610**HIGHLIGHTS**

- Development of low-cost, low-complexity, and easy-to-implement 2D mmWave SAR imaging system
- By employing single transceiver pair and taking sparse samples SAR imaging of UAVs is achieved.
- mmWave FMCW SAR imaging applications have the potential to be an innovative approach to UAV detection.

**Article Info**

Received : March 21, 2024

Accepted : May 27, 2024

**DOI:**

10.53525/jster.1456610

**\*Corresponding Author:**Bengisu Yalcinkaya  
Gokdogan  
[bengisu.yalcinkaya@atilim.edu.tr](mailto:bengisu.yalcinkaya@atilim.edu.tr)

Phone: +90 312 5868374

**ABSTRACT**

In recent years, millimeter wave (mmWave) frequency modulated continuous wave (FMCW) radars have gained popularity in radar imaging applications, coinciding with the advancement of mmWave technology. However, high cost and integration complexity still remain as issues in cases where the target aperture is large. This work introduces a low-cost, low-complexity, and easy-to-implement two-dimensional (2D) mmWave synthetic aperture radar (SAR) system. A commercial-off-the-shelf (COTS) mmWave FMCW radar sensor operating in the frequency range of 77-81 GHz is employed. A large mechanical scanning system which can move in both vertical and horizontal directions is constructed and integrated with the radar sensor. Developing a graphical user interface (GUI), an automatic movement of the scanner is achieved. Experimental measurements are taken in a laboratory environment and the effectiveness of the system is demonstrated. A cross-shaped metal object and a drone are chosen as targets and the SAR images of targets are obtained. For simplicity, by employing a single transceiver pair, sparse samples are taken in a large scanning aperture. It has been shown that the proposed scanning system has great potential in SAR imaging of large objects such as unmanned aerial vehicles (UAVs).

**Keywords:** mmWave, Frequency modulated continuous wave radar, Synthetic aperture radar, Sar imaging, Drone, Unmanned aerial vehicle



## I. INTRODUCTION

In recent years, radar imaging has been in demand since having the ability to successfully operate in different weather conditions, distances, and surroundings [1]. Studies concerning imaging using mmWave sensors ranging from 30 GHz to 300 GHz have increased distinctively in many civilian, commercial, and military applications [2-4]. Specifically, millimeter-wave (mmWave) imaging has emerged as one of the most significant technologies of near-field imaging applications [5]. Custom-built systems are proposed in the initial studies including concealed item detection [6], three-dimensional (3D) imaging [7], and multistatic structures [8]. Along with the advantages such as health-wise nonhazardous frequency band and diffusion capability to a variety of materials, mmWave frequencies can bring some disadvantages such as demand for a large number of antennas to obtain a high-resolution image, relatedly high cost and integration complexity.

Lately, commercial-off-the-shelf (COTS) mmWave frequency-modulated-continuous-wave (FMCW) radar systems have gained popularity in synthetic aperture radar (SAR) imaging applications due to their advantages such as low cost, easy access and simple implementation [9]. Consequently, COTS mmWave FMCW radar sensors have begun to be employed in a variety of fields including automotive [10], medical [11], and defense [12] industries and the studies regarding achieving high-resolution imaging have gained diversity. To obtain high resolution, multiple-input multiple-output (MIMO) SAR systems take the lead in the literature. A novel algorithm is introduced in [13] for near-field MIMO-SAR imaging with irregular scanning geometries. An algorithm for mmWave MIMO-SAR imaging for automotive applications presented in [14]. [15,16] employ the MIMO-SAR imaging of small objects in near-field. Additionally, mmWave radar sensors have begun to take part in sensor fusion applications. Employing optical and mmWave SAR image fusion, indoor object recognition is proposed in [17]. Employing 68-92 GHz FMCW radar, 2-D multi-object indoor environment mapping is implemented. Using the combination of SAR and optical images, the recognition of the objects in the indoor environment is carried out. Yet, above-mentioned applications may bring also cost and complexity issues along in cases where the target aperture is large.

Recent advancements in mmWave FMCW radar applications offer great potential in the detection of hostile agents such as unmanned aerial vehicles (UAV). UAV detection and ranging are achieved by employing FMCW radar operating at 77-81 GHz in [18] and at 35 GHz in [19]. For the detection of nano-drones, a K-band FMCW radar is designed and the micro-doppler signatures are obtained in [20]. mmWave FMCW SAR imaging applications also have the potential to be an innovative approach to UAV detection due to advantages such as low cost, low complexity, and ease of implementation, however, the literature has remained largely insufficient.

In this study, a low-cost two-dimensional (2D) mmWave SAR imaging system is proposed. Contrary to many existing studies, SAR measurements are taken by using a low-cost COTS radar and scanning system in a laboratory environment instead of high-cost, high-complexity, and difficult-to-access radars and scanners, and an anechoic chamber. To reduce the cost and complexity, monostatic SAR measurements are taken instead of employing MIMO topology. A SAR imaging system is created by employing a COTS mmWave FMCW radar sensor and mounting it on a scanning platform. A 1 meter by 1 meter scanner is constructed. Constructing a scanner with an extended aperture enables SAR imaging of large objects. While the scanning platform moves in both vertical and horizontal directions, the radar sensor collects measurements. By this means, a virtual antenna array is obtained in a desired scanning aperture. By considering the Nyquist sampling criterion along with the cross-range resolution of the image, SAR measurements are taken. After the image reconstruction process, the 2D SAR image of the target is obtained. The applicability of the scanner is confirmed by experimental measurements. A large cross-shaped metal object and a drone are used as targets. By employing the SAR scanning system of reduced cost and complexity and taking sparse samples, the imaging of the targets is achieved.

The remaining of the paper is organized as follows; Section II proposes the related literature in the field. In Section

III, the radar signal model, SAR system design specifications, and the employed image reconstruction method are mentioned. The construction of the scanning system and the experimental system configuration are presented in Section IV. The results are given in Section V. Section VI draws conclusions.

## II. RELATED WORK

A low-cost, high-resolution mmWave FMCW SAR imaging system is proposed in [21]. The 77 GHz radar sensor is combined with a two-axis scanner. The maximum scanning range of the system in both directions is 40 cm which limits the size of the target to be scanned. Since the scanning aperture is small, SAR imaging of small targets is studied at close range.

In [9], a near-field MIMO-SAR mmWave imaging of small objects is achieved by taking sparse samples. A 77 GHz FMCW radar is mounted on the 40 cm scanner. High resolution images of small objects are obtained. However, employing MIMO array topology brings complexity issues.

A near-field mmWave FMCW-SAR based static hand gesture recognition application is presented in [22]. SAR images of different hand gestures are obtained with 77 GHz MIMO radar sensor and a two-axis scanner. The maximum distance between the radar and the scanner is set to 40 cm.

When the related works are examined, it can be concluded that mmWave FMCW SAR imaging applications are studied especially for near-field scenarios and small objects. To obtain high resolution, MIMO array topology is employed at the cost of computational complexity.

## III. METHOD

### A. FMCW Signal Model

An FMCW radar generates a frequency modulated signal which is also known as a chirp signal. The transmitted chirp signal can be expressed as in eq.(1)

$$m(t) = \cos(2\pi f_i t + S\pi t^2) \quad (1)$$

where  $f_i$  is the instantaneous carrier frequency and  $S$  is the frequency slope which can be derived from the bandwidth  $B$  and the chirp duration  $T$

$$S = \frac{B}{T} \quad (2)$$

The transmit signal hits the target and is received back with a round trip delay  $\tau$

$$m(t - \tau) = \cos(2\pi(f_i\tau + S\tau t) - S\pi\tau^2) \quad (3)$$

$S\tau$  indicates the beat frequency  $f_b$  and it provides the range of the target.  $S\pi\tau^2$  is known as the residual video phase (RVP) and can be neglected. Thus, the received signal in eq.(3) can be rewritten as

$$r(t) = \cos(2\pi(f_i\tau + f_b t)) \quad (4)$$

### B. SAR System Design

A cost-effective 2D SAR imaging system is designed by integrating a radar sensor with a mobilizing scanner as shown in Fig.1. This method yields a sampling of the target aperture vertically and horizontally. The sampling distance is indicated in the horizontal direction as  $a_x$ , and the vertical direction as  $a_y$ . By employing one transmit and one receive antenna, an array of virtual antennas is created. The radar scans the total area of  $A_x \times A_y$  with a sampling steps of  $a_x$  and  $a_y$ . After the image reconstruction process, a 2D image of the target at the distance  $z$  is created.

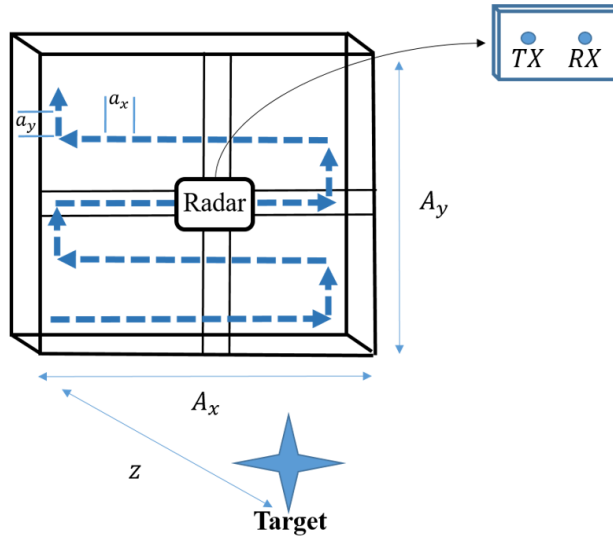


**Figure 1.** SAR system motion demonstration.

By taking measurements at each  $xy$  measurement point, a data cube  $r(x, y, t)$  is obtained based on the received signal in the eq.(4). The SAR image of the target is reconstructed by obtaining the reflectivity function  $s(x, y)$  from the received data cube  $r(x, y, t)$ .

### C. SAR System Specifications

The well-known range resolution  $z_{res}$  can be calculated from the bandwidth  $B$  and the speed light constant  $c$  as follows

$$z_{res} = \frac{c}{2B} \quad (5)$$

For 2D SAR imaging, the cross-range resolutions in horizontal and vertical directions represents the image resolution [23]

$$z_{x,y} = \frac{z\lambda}{2A_x A_y} \quad (6)$$

where  $\lambda$  is the wavelength,  $A_x$  and  $A_y$  are the total scanning apertures in horizontal and vertical directions respectively as shown in Fig.1.

Additionally, to prevent aliasing and consequently ghost images, the Nyquist spatial sampling criterion should be met while taking measurements. The sampling intervals  $a_x$  and  $a_x$  shown in Fig.1 should be specified accordingly

[7]. For the worst case, spatial sampling distances should satisfy  $a_{x,y} < \lambda/4$ .

Considering the above-mentioned criteria, spatial sampling intervals, SAR aperture size, and target distance from the radar are determined.

#### D. SAR Image Reconstruction

In SAR imaging applications, to reconstruct the target image, the reflectivity function should be recovered from the collected radar data. For this purpose, image reconstruction algorithms are employed. This paper uses a matched filter-based image reconstruction [24] to create a SAR image of the target from the collected data set by the constructed SAR system. Since the method is based on the distance of the target, SAR imagery of multiple targets at different distances on the same alignment can be achieved. The system's impulse response can be determined as follows

$$h(x, y) = \exp(-jk\sqrt{x^2 + y^2 + z^2}) \quad (6)$$

where  $k$  is the wavenumber,  $z$  is the distance between the radar and the target,  $x$  and  $y$  denotes the measurement points at horizontal and vertical directions respectively. The reflected signal can be determined by the following convolution operation

$$r(x, y) = s(x, y) * h(x, y) \quad (7)$$

Thus, taking the 2D Fourier transform ( $F_{2D}$ ) of both the received signal and the filter, multiplying them in the spatial frequency domain, and subsequently taking the inverse Fourier transform ( $F_{2D}^{-1}$ ) to return back to the spatial domain gives the reflectivity function

$$s(x, y) = F_{2D}^{-1}[F_{2D}(r(x, y))F_{2D}(h(x, y))^*] \quad (8)$$

The data cube creation and image reconstruction processes are conducted in the Matlab environment.

## IV. EXPERIMENTAL SYSTEM CONFIGURATION

A low-cost SAR system is constructed by integrating an mmWave radar sensor and a two-axis scanner.

#### A. Radar Sensor

A COTS mmWave FMCW radar sensor AWR1642 developed by Texas Instruments (TI) is employed for experimental measurements. For data acquisition, TI's DCA1000 evaluation module is integrated with AWR1642. The radar system is shown in Fig.2. AWR1642 offers a maximum bandwidth of 4 GHz between the operating frequencies 77-81 GHz. It allows MIMO measurements with two transmit and four receive antennas. DCA1000 captures the data and transfers it to the host computer. At the host computer, mmWave Studio Suite environment is used to display and process the captured data. Using this environment, board control, setting the parameters of a chirp signal, post-processing of ADC data, and visualization of processed data operations can be conducted. From the mmWave Studio, the received signal can be extracted in the form of complex in-phase/quadrature (I/Q) at intermediate frequency (IF).

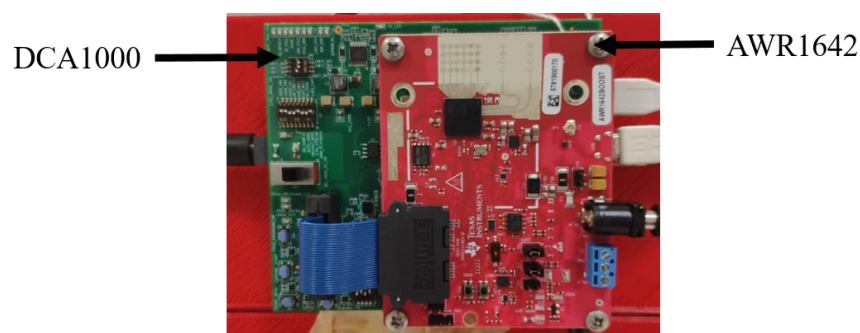


**Figure. 2.** Radar system.

### *B. SAR Scanner*

A 2D mechanical scanning system that can move in horizontal and vertical directions is designed and the radar module is mounted on the system as shown in Fig.3. The scanning aperture of the system is 1 meter in both vertical and horizontal directions. The large aperture of the scanner provides the flexibility to obtain high-quality SAR images of small targets along with sparse sampled SAR imagery of large targets. The system takes stationary measurements between the sampling distances and the minimum sampling distance is achieved as 1 mm. The motion of the scanner is enabled with four stepper motors. The measurements are taken in a laboratory environment without an anechoic chamber.

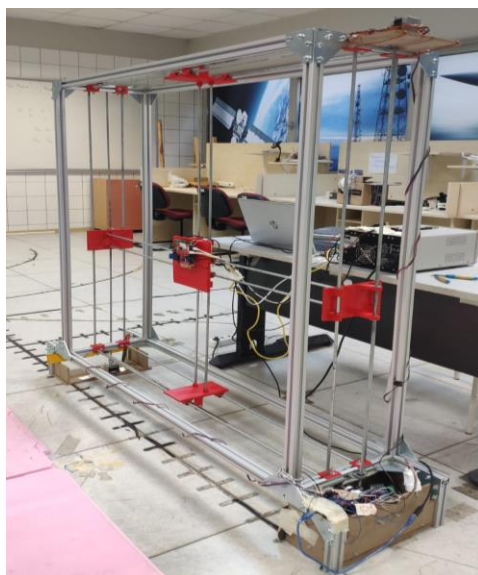


**Figure. 3.** SAR scanner.

### *C. SAR System*

The SAR scanning system is constructed by combining the mechanical scanner and the mmWave radar sensor. Both the radar sensor and the microcontroller are linked to the host computer. As a microcontroller, Arduino UNO is employed. The radar sensor is controlled by the mmWave Studio. A graphical user interface (GUI) is designed to control both the mmWave Studio and the motion of the system as demonstrated in Fig.4. The system is designed so that the elapsed time between successive samples is 5 seconds.



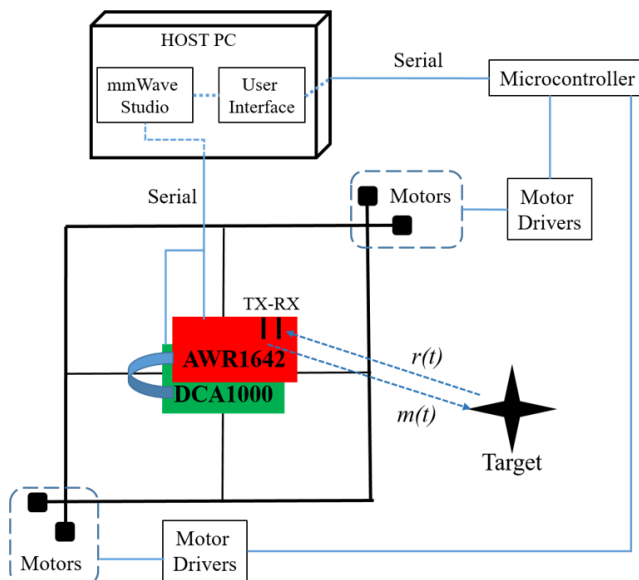


Figure. 4. Structural diagram of the SAR system.

Using the interface, users can specify sampling distances, total scan apertures, and motion repetition in both the vertical and horizontal axis. The designed user interface is shown in Fig.5.

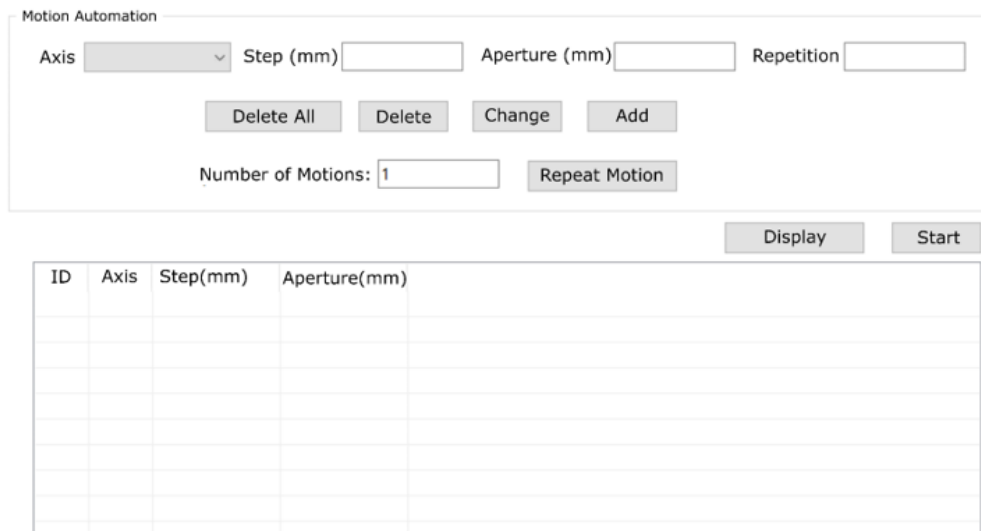


Figure. 5. User interface.

## V. RESULTS

By taking monostatic measurements of different types of objects in a laboratory environment, the constructed SAR imaging system is verified.

A 45x45 cm cross shape metal object is used as target as shown in Fig.6. One transmit and one receive antennas were used. The distance between the scanner and the target was set to 70 cm. The total scanning aperture was 30 cm and the sampling distance was 4 mm which gives the image resolution of 4,3 mm in both vertical and horizontal

directions. A  $256 \times 75 \times 75$  radar data cube is obtained with a total of 5625 measurement points. By taking sparse sampling, a SAR image of a large object is reconstructed successfully.

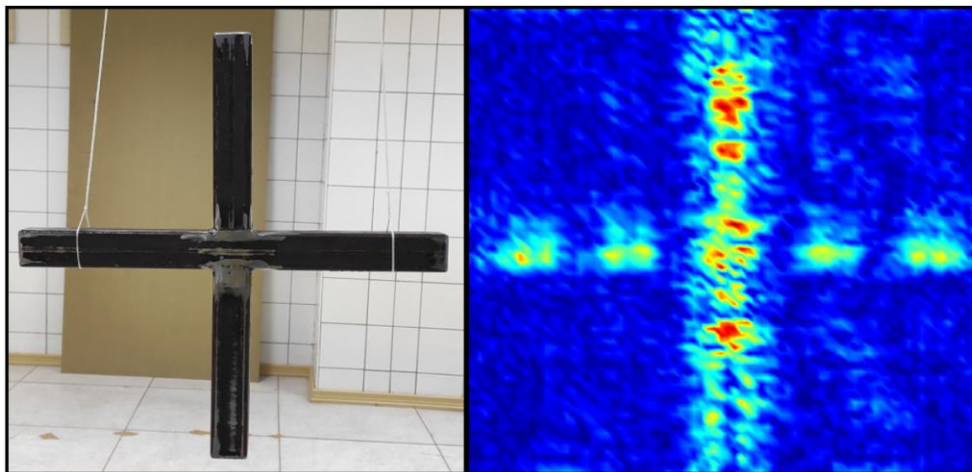


**Figure. 6.** SAR imaging result of cross object at 70 cm distance.

Then, the same object is settled 30 cm before the radar. 10 cm of aperture is scanned with 3 mm sampling distances in both vertical and horizontal axes. The imaging result is given in Fig.7.

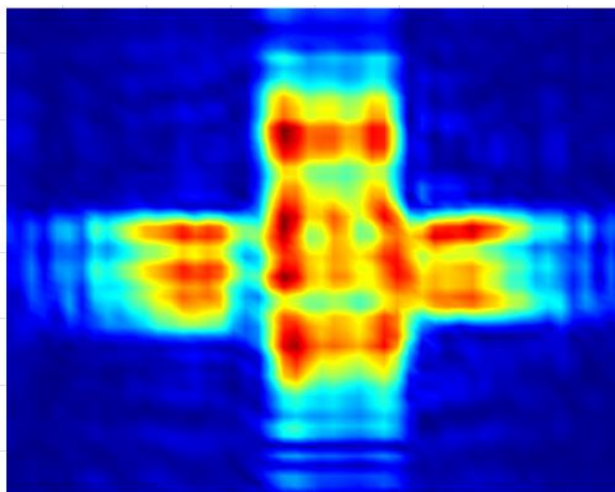


**Figure. 7.** SAR imaging result of cross object at 30 cm distance.

Lastly, the imaging of a  $45 \times 45$  cm drone is achieved. The drone is put at 70 cm distance from the radar. 30 cm aperture is scanned with 4 mm sampling distances. The imaging result is shown in Fig.8.

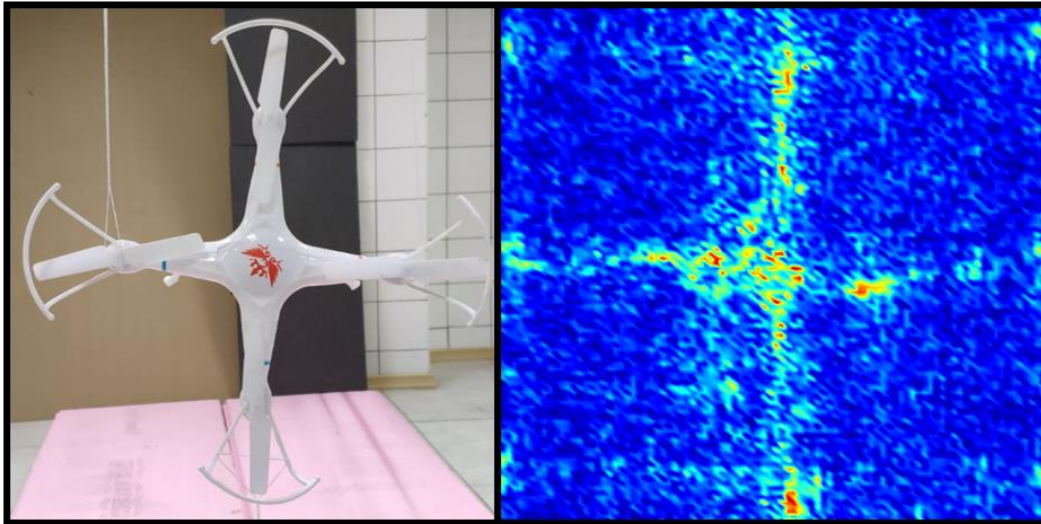


**Figure 8.** SAR imaging result of drone at 30 cm distance.

## VI. CONCLUSION

In this work, as a part of an ongoing study, employing mmWave SAR imaging techniques and using low-cost COTS radar and scanning system, SAR imaging of different types of targets is achieved in a laboratory environment. First, a low-cost radar scanner is built to obtain a SAR imaging system. Then, a radar data cube is created by taking monostatic measurements with mmWave FMCW COTS radar mounted on the scanning system. By taking sparse samples, the SAR imagery of large cross-shaped metal object and a drone is obtained. Promising results have been obtained for future UAV detection studies. In future work, employing deep learning applications, the recognition of SAR images of different types of targets can be employed. The recognition success can be studied in different image resolutions.

## CONFLICTS OF INTEREST

They reported that there was no conflict of interest between the authors and their respective institutions.

## RESEARCH AND PUBLICATION ETHICS

In the studies carried out within the scope of this article, the rules of research and publication ethics were followed.

## ACKNOWLEDGMENT

The authors would like to thank the students of Gazi University Furkan Çetinkaya, Erenca Tezel, Oğuz Yalçın, and Berkan Öksüz for their contribution to the construction of the SAR scanner.

## REFERENCES

- [1] Wellig, P., Speirs, P., Schuepbach, C., Oechslin, R., Renker, M., Boeniger, U., & Pratisto, H. (2018, June). Radar systems and challenges for C-UAV. In *2018 19th International Radar Symposium (IRS)* (pp. 1-8). IEEE.
- [2] Mirbeik-Sabzevari, A., Li, S., Garay, E., Nguyen, H. T., Wang, H., & Tavassolian, N. (2018). Synthetic ultra-high-resolution millimeter-wave imaging for skin cancer detection. *IEEE Transactions on biomedical engineering*, 66(1), 61-71.
- [3] Ghasr, M. T., Kharkovsky, S., Bohnert, R., Hirst, B., & Zoughi, R. (2013). 30 GHz linear high-resolution and rapid millimeter wave imaging system for NDE. *IEEE Transactions on Antennas and Propagation*, 61(9), 4733-4740.
- [4] Liu, T., Zhao, Y., Wei, Y., Zhao, Y., & Wei, S. (2019). Concealed object detection for activate millimeter wave image. *IEEE Transactions on Industrial Electronics*, 66(12), 9909-9917.
- [5] Song, S., Lu, J., Xing, S., Quan, S., Wang, J., Li, Y., & Lian, J. (2022). Near Field 3-D Millimeter-Wave SAR Image Enhancement and Detection with Application of Antenna Pattern Compensation. *Sensors*, 22(12), 4509.

- 
- [6] Zhuge, X., & Yarovoy, A. G. (2010). A sparse aperture MIMO-SAR-based UWB imaging system for concealed weapon detection. *IEEE Transactions on Geoscience and Remote Sensing*, 49(1), 509-518.
- [7] Sheen, D. M., McMakin, D. L., & Hall, T. E. (2001). Three-dimensional millimeter-wave imaging for concealed weapon detection. *IEEE Transactions on microwave theory and techniques*, 49(9), 1581-1592.
- [8] Abbasi, M., Shaye, A., Shabany, M., & Kavehvash, Z. (2018). Fast Fourier-based implementation of synthetic aperture radar algorithm for multistatic imaging system. *IEEE Transactions on Instrumentation and Measurement*, 68(9), 3339-3349.
- [9] Yanik, M. E., & Torlak, M. (2019). Near-field MIMO-SAR millimeter-wave imaging with sparsely sampled aperture data. *Ieee Access*, 7, 31801-31819.
- [10] Venon, A., Dupuis, Y., Vasseur, P., & Merriaux, P. (2022). Millimeter wave FMCW radars for perception, recognition and localization in automotive applications: A survey. *IEEE Transactions on Intelligent Vehicles*, 7(3), 533-555.
- [11] Zhao, Y., Sark, V., Krstic, M., & Grass, E. (2021, October). Multi-Target Vital Signs Remote Monitoring Using mmWave FMCW Radar. In *2021 IEEE Microwave Theory and Techniques in Wireless Communications (MTTW)* (pp. 290-295). IEEE.
- [12] Chen, Y. S., Cheng, K. H., Xu, Y. A., & Juang, T. Y. (2022). Multi-Feature Transformer-Based Learning for Continuous Human Motion Recognition with High Similarity Using mmWave FMCW Radar. *Sensors*, 22(21), 8409.
- [13] Smith, J. W., & Torlak, M. (2022). Efficient 3-D near-field MIMO-SAR imaging for irregular scanning geometries. *IEEE Access*, 10, 10283-10294.
- [14] Zhang, B., Xu, G., Zhou, R., Zhang, H., & Hong, W. (2022). Multi-channel back-projection algorithm for mmwave automotive MIMO SAR imaging with Doppler-division multiplexing. *IEEE Journal of Selected Topics in Signal Processing*.
- [15] Yanik, M. E., Wang, D., & Torlak, M. (2020). Development and demonstration of MIMO-SAR mmWave imaging testbeds. *IEEE Access*, 8, 126019-126038.
- [16] Yanik, M. E., Wang, D., & Torlak, M. (2019, November). 3-D MIMO-SAR imaging using multi-chip cascaded millimeter-wave sensors. In *2019 IEEE global conference on signal and information processing (GlobalSIP)* (pp. 1-5). IEEE.
- [17] Batra, A., Hark, T., Schorlemer, J., Pohl, N., Rolfes, I., Wiemeler, M., ... & Barowski, J. (2022, July). Fusion of optical and millimeter wave sar sensing for object recognition in indoor environment. In *2022 Fifth International Workshop on Mobile Terahertz Systems (IWMTS)* (pp. 1-5). IEEE.
- [18] Doğanay, B., Arslan, M., Demir, E. C., Çoruk, R. B., Gökdoğan, B. Y., & Aydın, E. (2022, May). UAV Detection and Ranging with 77-81 GHz FMCW Radar. In *2022 30th Signal Processing and Communications Applications Conference (SIU)* (pp. 1-4). IEEE.
- [19] Drozdowicz, J., Wielgo, M., Samczynski, P., Kulpa, K., Krzonkalla, J., Mordzonek, M., ... & Jakielaszek, Z. (2016, May). 35 GHz FMCW drone detection system. In *2016 17th International Radar Symposium (IRS)* (pp. 1-4). IEEE.
- [20] Zulkifli, S., & Balleri, A. (2020, September). Design and development of K-band FMCW radar for nano-drone detection. In *2020 IEEE Radar Conference (RadarConf20)* (pp. 1-5). IEEE.
- [21] Yanik, M. E., & Torlak, M. (2018). Millimeter-wave near-field imaging with two-dimensional SAR data. *Proc. SRC Techcon*, (P093929).
- [22] Hao, Z., Wang, R., Peng, J., & Dang, X. (2023). Static Hand Gesture Recognition Based on Millimeter-Wave Near-Field FMCW-SAR Imaging. *Electronics*, 12(19), 4013.
- [23] Zhuge, X., & Yarovoy, A. G. (2012). Three-dimensional near-field MIMO array imaging using range migration techniques. *IEEE Transactions on Image Processing*, 21(6), 3026-3033.
- [24] Patole, S., & Torlak, M. (2013). Two dimensional array imaging with beam steered data. *IEEE transactions on image processing*, 22(12), 5181-5189.



## RESEARCH ARTICLE

# A Supervised Learning Approach With Residual Attention Connections

<sup>1</sup> Hamza Ali, <sup>1</sup> Fazal Muhammad, <sup>2</sup> Talha Ali, <sup>3</sup> Fazal-e-Wahab, <sup>1</sup> Muhammad Ismail,

<sup>1</sup>Department of Electrical Engineering, University of Engineering & Technology, Mardan, KPK (Pakistan)  
[engr.hamarwat@gmail.com](mailto:engr.hamarwat@gmail.com), [fazal.muhammad@uetmardan.edu.pk](mailto:fazal.muhammad@uetmardan.edu.pk), [m.ismail012018@gmail.com](mailto:m.ismail012018@gmail.com)

<sup>2</sup>Department of Electrical Engineering, University of Engineering & Technology, Peshawar, KPK (Pakistan)  
[talhanisar849@gmail.com](mailto:talhanisar849@gmail.com)

<sup>3</sup>National Engineering Laboratory for Speech and Language Information Processing, University of Science and Technology of China, Hefei, 230026 Anhui (China)

**Citation:**

Hamza A., Fazal M., Talha Ali, Fazal-e-W., Muhammad I. (2024). *A supervised learning approach with residual attention connections*, Journal of Science Technology and Engineering Research, 5(1): 78-85. 10.53525/jster.1469477

**HIGHLIGHTS**

- Effect and important of this article in literature
- Exchange between sources in related subjects of this article
- Contribution and strongest impact on the related subject of this article
- Examined study and obtained results why is important

**Article Info**

Received : April 16, 2024

Accepted : May 27, 2024

**DOI:**

10.53525/jster.1469477

**<sup>1</sup>Corresponding Author:**

Hamza Ali

[engr.hamarwat@gmail.com](mailto:engr.hamarwat@gmail.com),

Phone: +92 333 9971656

**ABSTRACT**

*The proposed study aims to improve speech quality despite background noise, which often disrupts clear communication. We focus on developing efficient and effective models that work well on devices with limited resources. We draw inspiration from computational auditory scene analysis techniques to train proposed models to differentiate speech from background noise while keeping computational demands low. We introduce two models: CRN-WRC (Convolutional Recurrent Network without Residual Connections) and CRN-RCAG (Convolutional Recurrent Network with Residual Connections and Attention Gates). Our thorough testing shows that proposed models significantly enhance speech quality and understanding, even in noisy environments with varying background noise levels. Notably, the CRN-RCAG model consistently outperforms the CRN-WRC, particularly in handling untrained noise types. We achieve impressive results by integrating residual connections and attention gates into proposed models while maintaining computational efficiency.*

**Keywords:** Speech enhancement, Convolutional Recurrent Network, supervised learning, Gated Recurrent Unit, Residual-connection



## I. INTRODUCTION

We are constantly surrounded by sound, whether indoors or outside. We are constantly surrounded by many sorts of noise like traffic noise, and street noise however, this noise can occasionally interfere with effective communication. Even automated speech recognition (ASR) [1] technologies face difficulties in understanding us. To fix this, speech enhancement becomes critical. It seeks to improve speech quality by converting noisy input into clearer output. However, typical voice-augmentation algorithms can be computationally intensive, particularly for devices with limited resources. The proposed research focuses on developing lightweight and efficient models designed primarily for low-power devices with limited memory and processing capability. We aim to remove background noise from your voice without draining your device’s resources. To achieve this, we use supervised learning techniques inspired by computational auditory scene analysis (CASA) [2], Supervised methods [3] involve creating separate models for speech and noise signals, with the parameters of these models learned using training examples that include both types of signals. We use masking and mapping [4] targets in the T-F domain to guide proposed models toward achieving optimal results without overwhelming them with complexity. The CRNN identifies critical speech components [5], [6], which analyses the time-frequency bands. As this is going on, the AG serves to let important information through while blocking out unwanted noise. The result: significantly enhanced speech quality, even in challenging acoustic environments. This research has significant implications for various applications. Improved speech quality and intelligibility directly benefit ASR systems, voice communication, and assistive hearing devices. By leveraging the magic of deep learning [7], we are paving the way for a future where clear communication is no longer hindered by noise. This paper contributes to this domain by offering a lightweight yet effective approach to single-channel speech enhancement, promising better speech quality and intelligibility. The proposed work bridges the gap between speech enhancement and resource constraints. By incorporating skip connections and attention gates within the CRNN architecture, we achieve remarkable results while ensuring computational efficiency.

## II. PROPOSED METHOD

In proposed research, we employ two distinct models to tackle the task at hand. The first model, referred to as a conventional convolutional recurrent network without residual connections (CRN-WRC), integrates a recurrent block network for speech enhancement (SE). Meanwhile, the second model incorporates residual connections with (1×1) kernel size and attention gates (CRN-RCAG) within the CRNN architecture to enhance its performance.

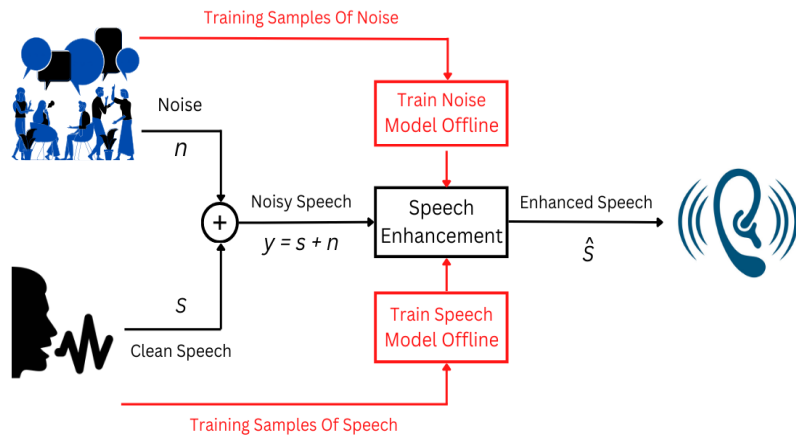


Fig. 1. Supervised Approach to Noise Reduction: Speech and Noise Model Interaction

### A. Conventional CRN-WRC Model

The architecture of proposed Convolutional Recurrent Network is depicted in Fig.2. shows the network architecture, which consists of five layers for the causal encoder and decoder, respectively, that are convolutional (Conv2D) and deconvolutional (Deconv2D) [8], [9]. Exponential linear units are used in all layers but the output layer, which uses soft-plus activation [10]. A Gated Recurrent Unit (GRU) layer models the latent feature sequences after inputs are

first encoded into a high-dimensional latent space [11]. Then the GRU layer’s output sequences are converted back into their original shape by the decoder. This method combines two powerful topologies convolutional neural networks (CNNs) [12] for feature extraction and recurrent neural networks (RNNs) [13] for temporal modelling to produce better outcomes. In proposed study, we leverage residual connections to enhance information flow and address redundancy in speech enhancement. Specifically, we connect the encoder outputs to the decoder inputs using these residual connections as depicted in Fig.3. Additionally, we incorporate attention gates (AGs) [14] within these connections to effectively reduce redundant regions while emphasizing important spectral features. Given the large number of frequency components in the spectra, we recognize that formant frequencies dominate low-frequency areas, while high-frequency regions exhibit a sparse distribution. In speech, certain frequencies are more important than others. For example, low-frequency areas usually have more dominant sounds, while high-frequency areas have fewer sounds. So, it’s crucial to give more attention to the important parts of the speech signal. Therefore, it is crucial to differentiate distinct spectral locations with varying weights.

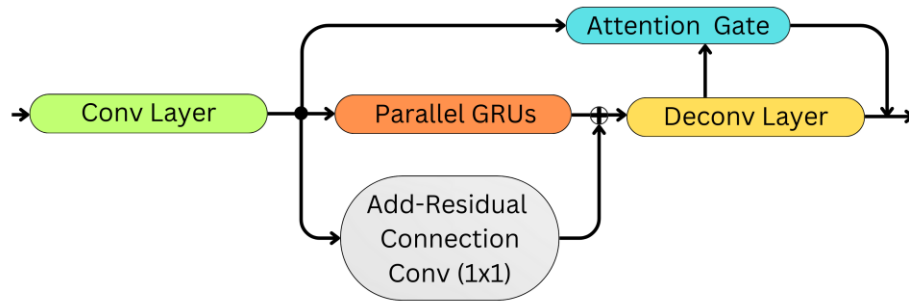


Fig. 3. CRN Architecture for Speech Enhancement with Residual Connections and Attention Gates

*B. Extending the Proposed Model*

The encoder’s job is to take the input features and find the important parts while making the information easier to work with. It does this by passing the input features through five layers that squeeze them down and make them more manageable. Then, special layers called GRU layers help the model understand the order of the information over time, and another layer helps adjust the features even more. AGs help the model focus on the most important parts of the input, ignoring the rest. These AGs work by comparing the features from different parts of the model and deciding what’s important. The decoder’s job is to take the simplified features and turn them back into the original input size. This completes the cycle, making the whole process like a mirror image. By adding Attention Gates, the decoder becomes even better at generating accurate results. Additionally, residual connections (1 x 1) kernel size helps the flow of information by linking the output of one part of the model to the input of another. This ensures that important information isn’t lost as it moves through the network.

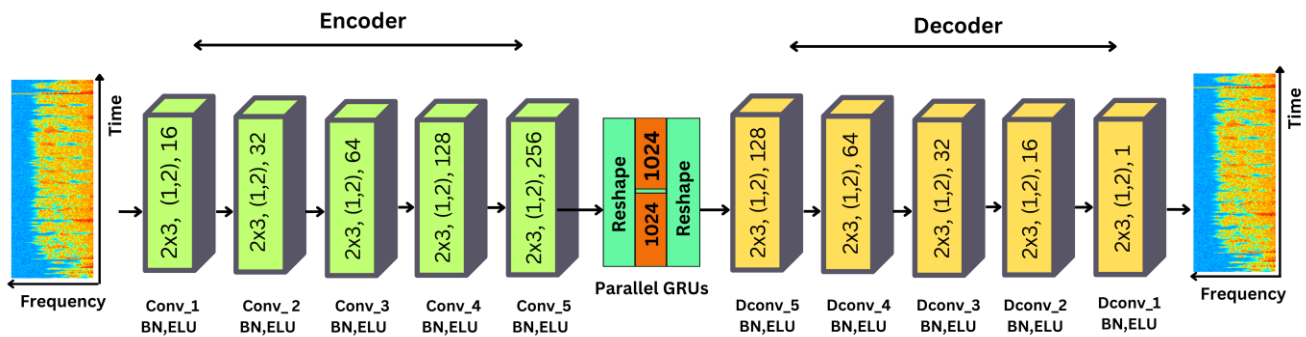


Figure. 2. The architecture of Convolutional Recurrent Network without residual connections

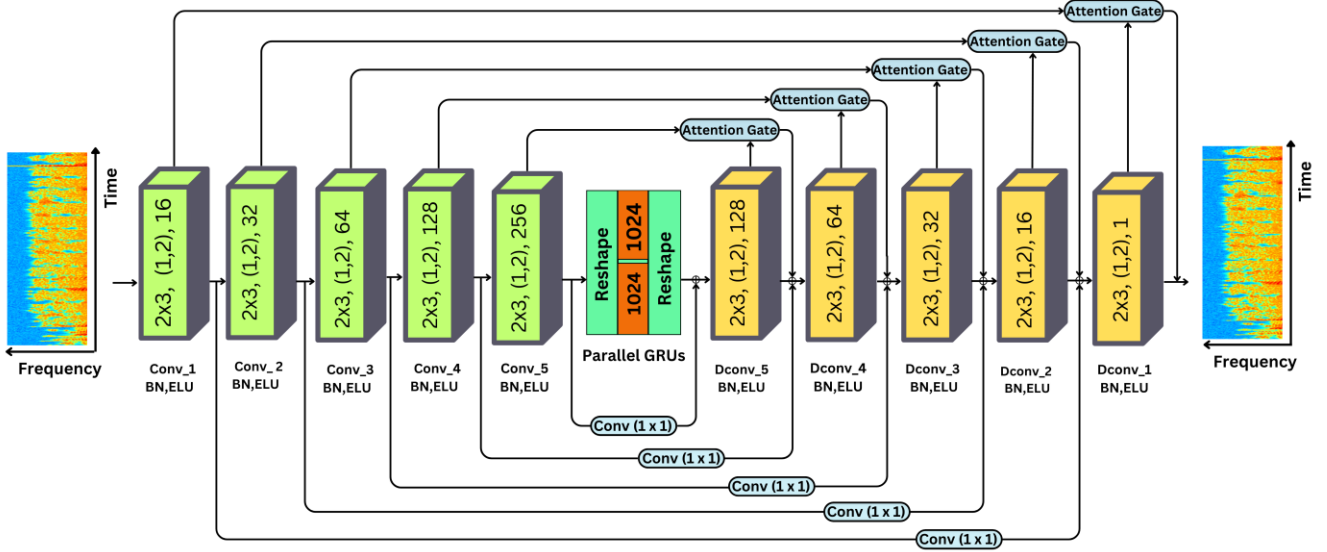


Fig. 4. CRN Architecture for Speech Enhancement with Residual Connections and Attention Gates

### C. Parallel GRUs For Temporal Modelling

In proposed experiments, we use Gated Recurrent Unit (GRU) models to help us predict what a future speech frame might look like based on past frames. We used a window of 11 frames, including 10 past frames and 1 present frame, to make this prediction. We fed a long vector of these 11 frames into the network at each step. GRU is a newer type of recurrent neural network known for its memory cells, which are good at understanding patterns over time. To capture the timing of speech signals, we added a GRU layer between the encoder and decoder parts of proposed model. The equations describe how GRU works, including terms like  $z$ ,  $r$ , and  $h$ , and illustrate the update gate and reset gate, which helps the model learn from the data.

$$z_t = \sigma(W_z[x_t, h_{t-1}] + b_z) \quad (1)$$

$$r_t = \sigma(W_r[x_t, h_{t-1}] + b_r) \quad (2)$$

$$\bar{h}_t = \tanh(W_h[r_t \odot h_{t-1}, x_t] + b_h) \quad (3)$$

$$h_t = (1 - z_t) \odot h_{t-1} + (z_t) \odot \bar{h}_t \quad (4)$$

To handle the input shapes required by GRUs, we used a technique from a previous study to group the large network into smaller, parallel networks. This helps the model process information more efficiently.

## III. EVALUATION METRICS

To evaluate the proposed networks, we used two primary performance metrics: Short-Time Objective Intelligibility (STOI) and Perceptual Evaluation of Speech Quality (PESQ).

### A. STOI (Short-Time Objective Intelligibility)

STOI is a metric used to measure the intelligibility of speech, particularly in noisy conditions. It is designed to predict the intelligibility of processed speech signals by comparing temporal envelopes of the original and degraded signals in short-time windows. Higher STOI values indicate better speech intelligibility. We chose STOI because it is highly correlated with human speech intelligibility scores, making it a reliable measure for our speech enhancement task.

### B. PESQ (Perceptual Evaluation of Speech Quality)

PESQ is a widely used objective measure for assessing the quality of speech signals. It compares an original clean signal with a processed or degraded version, providing a score that reflects perceived speech quality. PESQ takes into account various perceptual aspects of speech quality, making it a comprehensive metric for our evaluation. Higher PESQ scores indicate better speech quality. PESQ was chosen due to its robustness and its high correlation with subjective listening tests, which is crucial for evaluating enhancements in real-world noisy environments.

### C. Speech Dataset and Experimental Setup

In proposed research study, we tested speech enhancement networks using a large dataset called LibriSpeech [15], which includes recordings of people reading audiobooks that contain 0.22 million spoken sentences from 2,000 speakers. We focused on a subset of this dataset called LibriClean, which contains clean recordings, consisting of 104,015 high-quality utterances from 92 speakers. To evaluate proposed networks, we randomly selected 5000 speech samples from 40 speakers. Out of these speakers, we used 2 males and 2 females for testing whom the network hadn't heard before, and the rest were used for training. We also used various types of noise during training to make sure the networks could handle different environments. For testing, we used challenging noise types like multi-talker babble, street noise, and cafeteria noise. We tested proposed models with both trained and untrained speakers to see how well they could handle different voices. The proposed networks were trained using a method called Adam optimizer and optimized to reduce prediction errors.

## IV. FINDINGS AND DISCUSSION

Table 1 compares the performance of two speech enhancement models: CRN-WRC (Convolutional Recurrent Network without Residual Connections) and CRN-RCAG (Convolutional Recurrent Network with Residual Connections and Attention Gates). For each model, the results are presented for different noise conditions: babble noise, street noise, and cafeteria noise, across various signal-to-noise ratio (SNR) levels ranging from -6 dB to 6 dB.

Under each noise condition and SNR level, two sets of results are provided: 1. noisy: Represents the speech signal before enhancement. 2. enh: Represents the speech signal after enhancement using the respective model. Comparing the results between CRN-WRC and CRN-RCAG models, it is observed that the CRN-RCAG model consistently outperforms the CRN-WRC model across all noise conditions and SNR levels, as indicated by higher STOI and PESQ scores. This suggests that CRN-RCAG with residual connections and attention gates provides superior speech enhancement compared to CRN-WRC without residual connections. Both models effectively enhance speech quality, but CRN-RCAG stands out as the stronger performer across different noise conditions and SNR levels as illustrated in Fig. 5.

### A. Speech Enhancement Performance in Familiar Noisy Environments

The table 1 compares the performance of two different speech enhancement models, denoted as CRN-WRC and CRN-RCAG. For each model, two metrics are evaluated: PESQ and STOI. PESQ measures the perceived speech quality, while STOI evaluates the speech intelligibility. Tables 2 and 3 display the results for various signal-to-noise ratios (SNR), ranging from -6 dB to 6 dB.

Under each SNR condition, two scenarios are considered: “noisy,” representing the original speech signal before enhancement, and “enh,” representing the speech signal after enhancement using the respective model. Looking at the results, we observe that both CRN-WRC and CRN-RCAG models significantly improve speech quality and intelligibility compared to the original noisy speech across all SNR levels. For the CRN-WRC model, the PESQ scores range from 1.39 to 2.18 for noisy speech signals, and the STOI percentages range from 53.7% to 78.3%. After enhancement using CRN-WRC, there is a significant improvement in both PESQ scores (ranging from 2.26 to 3.01) and STOI percentages (ranging from 72.6% to 88.9%). Similarly, for the CRN-RCAG model, the PESQ scores range from 2.57 to 3.40 for enhanced speech signals, and the STOI percentages range from 83.7% to 95.3%. The enhancement provided by CRN-RCAG demonstrates superior performance compared to CRN-WRC, particularly evident in higher PESQ and STOI scores across different noise levels.

*B. Speech Enhancement Performance in Unfamiliar Noisy Environments*

In Table 3, The models were tested on two different types of untrained noise environments, airport noise, and factory noise. We compared the performance of proposed models in noisy conditions with no training on those specific noises. We found that proposed models improved speech quality and intelligibility compared to the original noisy speech, especially in untrained noisy environments like factory noise and cafeteria noise. For noisy signal the PESQ scores range from 1.12 to 1.39, and the STOI scores range from 52.4% to 64.2% in the airport noise environment. In the factory noise environment, the PESQ scores range from 1.34 to 1.83, and the STOI scores range from 56.7% to 73.9%. After enhancement using CRN-WRC, the PESQ scores improve significantly to a range of 1.83 to 2.26 in the airport noise environment and 2.13 to 2.26 in the factory noise environment. Similarly, the STOI scores increase to a range of 67.8% to 73.9% in the airport noise environment and 67.5% to 73.9% in the factory noise environment. When using CRN-RCAG, the PESQ scores further improve to a range of 2.19 to 2.48 in the airport noise environment and 2.31 to 2.48 in the factory noise environment. Correspondingly, the STOI scores increase to a range of 72.6% to 78.3% in the airport noise environment and 77.1% to 79.3% in the factory noise environment. However, CRN-RCAG demonstrates better performance, achieving higher PESQ scores and STOI percentages in both noise environments, indicating its effectiveness in enhancing speech signals corrupted by untrained noises. Table 4, illustrates how incorporating residual connections in the CRN-RCAG architecture affects performance. Adding residual connections is better than not adding them at all. While adding these connections improves the PESQ and STOI test scores, the best performance is achieved by including Conv (1 × 1) add-residual and Attention Gate Residual connections.

**TABLE I:** Performance Evaluation of CRN Speech Enhancement Models: A Comparative Analysis with STOI and PESQ Metrics.

Metric	Model	Noise	Babble Noise					Street Noise					Cafeteria Noise				
		SNR	-6	-3	0	3	6	-6	-3	0	3	6	-6	-3	0	3	6
STOI	CRN-WRC	noisy	54	60	68	73	80	58	66	72	73	83	56	62	67	71	77
		enh	72	81	84	86	88	74	80	85	87	91	75	82	85	87	89
	CRN-RCAG	enh	84	87	90	92	94	85	87	91	94	97	80	85	88	93	94
PESQ	CRN-WRC	noisy	1.4	1.4	1.8	1.9	2.1	1.6	1.6	1.7	1.9	2.0	1.5	1.6	1.7	1.9	2.3
		enh	2.2	2.6	2.7	2.8	2.9	2.3	2.6	2.7	2.9	3.0	2.4	2.5	2.7	3.0	3.0
	CRN-RCAG	enh	2.4	2.7	2.9	3.2	3.3	2.6	3.0	3.1	3.3	3.4	2.6	3.0	3.1	3.3	3.4

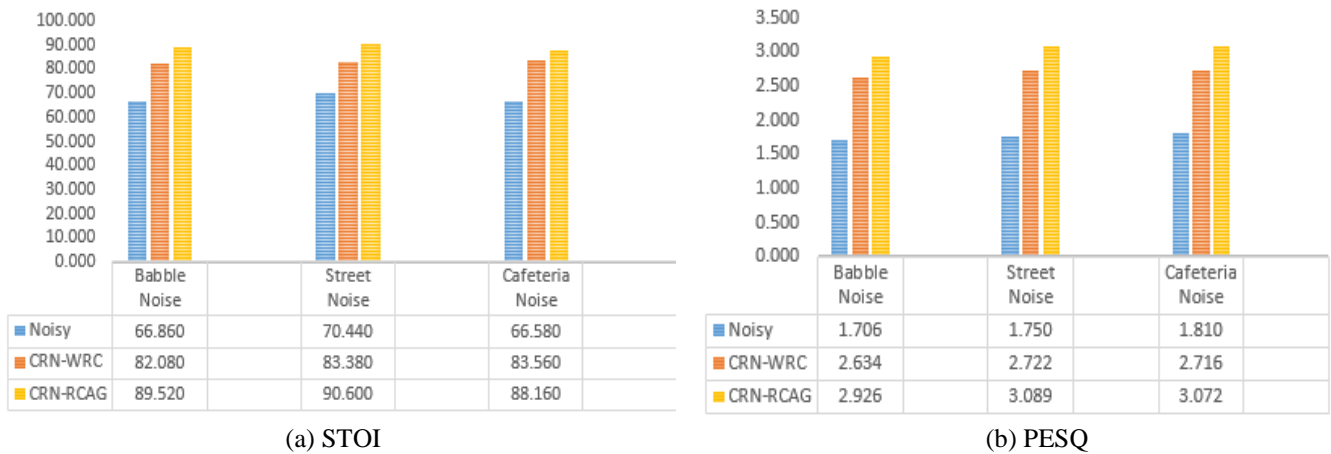


**Fig. 5.** PESQ and STOI Performance of CRN-WRC and CRN-RCAG Models Across Various Noise Conditions

**TABLE II:** Performance of Trained Noise Speech Enhancement under Various Noise Conditions.

Model	Metric	PESQ					STOI (in%)				
	SNR	-6	-3	0	3	6	-6	-3	0	3	6
CRN-WRC	noisy	1.39	1.48	1.63	1.86	2.18	53.7	61.7	66.3	72.1	78.3
	enh	2.26	2.48	2.62	2.88	3.01	72.6	79.3	82.7	87.1	88.9
CRN-RCAG	enh	2.57	2.91	3.17	3.38	3.40	83.7	89.5	92.1	94.6	95.3

**TABLE III:** Performance of Untrained Noise Speech Enhancement under Various Noise Conditions.

Model	Noise	Restaurant				Street			
	Metric	PESQ		STOI		PESQ		STOI	
	SNR	-6	-3	-6	-3	-6	-3	-6	-3
CRN-WRC	noisy	1.12	1.32	52.4	59.7	1.34	1.39	56.7	64.2
	enh	1.83	2.16	67.8	72.1	2.13	2.26	67.5	73.9
CRN-RCAG	enh	2.19	2.47	72.6	78.3	2.31	2.48	77.1	79.3

**TABLE IV:** Analysing the Impact of Residual Connections on Model Performance

Residual Types	STOI	PESQ
No Residual	78	2.34
Add Residual	83	2.49
Conv Residual	87	2.73
Residual-Attn	89	3.01

## V. CONCLUSION

In this paper, we present a novel approach to speech enhancement tailored for resource-constrained devices operating in noisy environments. By leveraging supervised learning techniques and innovative model architectures, we have successfully developed lightweight yet efficient models capable of significantly improving speech quality and intelligibility. Our experiments demonstrate the superiority of the CRN-RCAG model over the CRN-WRC model, emphasizing the importance of incorporating residual connections and attention gates for optimal performance. The results highlight the effectiveness of the proposed models in enhancing speech signals across various noise conditions and signal-to-noise ratio levels. Furthermore, the proposed models exhibit promising performance even when tested with untrained noise types, showcasing their robustness in real-world scenarios. Overall, this research bridges the gap between speech enhancement and resource constraints, offering a practical solution for clear communication in noisy environments.

**Future work** will focus on further optimizing and extending the proposed model architecture to enhance its applicability across a wider range of scenarios and devices. This includes: Exploring advanced techniques for model compression and acceleration to ensure even greater efficiency on resource-limited devices. Expanding the dataset to include a broader range of noise types and languages to enhance the model's generalizability and effectiveness in



different linguistic contexts. Collaborating with industry partners to implement and test the proposed models in practical applications, such as mobile communication systems and hearing aids, to facilitate seamless adoption and impact. By pursuing these future directions, we aim to further advance the state of speech enhancement technology, making high-quality, intelligible speech accessible in various challenging environments and on a wide array of devices.

#### ACKNOWLEDGMENT

First and foremost, I would like to express my heartfelt gratitude and appreciation to my supervisor, Dr. Fazal Muhammad, and my Co-supervisor Dr. Fazal-e-Wahab, for guiding me the academic research, supporting and encouraging me when I encountered difficulties, teaching me the theoretical knowledge and providing me valuable suggestions throughout my entire research. I also would like to extend my deep gratefulness to my friends for their nice help and comforts throughout my life during my master study.

#### REFERENCES

- [1] Kheddar, Hamza, et al. "Deep transfer learning for automatic speech recognition: Towards better generalization." *Knowledge-Based Systems* 277 (2023): 110851.
- [2] Kwak, Chanbeom, and Woojae Han. "Towards size of scene in auditory scene analysis: A systematic review." *Journal of Audiology & Otology* 24.1 (2020): 1.
- [3] Wang, DeLiang, and Jitong Chen. "Supervised speech separation based on deep learning: An overview." *IEEE/ACM transactions on audio, speech, and language processing* 26.10 (2018): 1702-1726.
- [4] Nossier, Soha A., et al. "Mapping and masking targets comparison using different deep learning based speech enhancement architectures." *2020 International Joint Conference on Neural Networks (IJCNN)*. IEEE, 2020.
- [5] Ye, Zhongfu, Nasir Saleem, and Hamza Ali. "Efficient gated convolutional recurrent neural networks for real-time speech enhancement." (2023).
- [6] Hsieh, Tsun-An, et al. "Wavecrn: An efficient convolutional recurrent neural network for end-to-end speech enhancement." *IEEE Signal Processing Letters* 27 (2020): 2149-2153.
- [7] Wang, Kai. *Novel Deep Learning Approaches for Single-Channel Speech Enhancement*. Diss. Concordia University, 2022.
- [8] Haar, Lynn Vonder, Timothy Elvira, and Omar Ochoa. "An analysis of explainability methods for convolutional neural networks." *Engineering Applications of Artificial Intelligence* 117 (2023): 105606.
- [9] Le, Xiaohuai, et al. "DPCRn: Dual-path convolution recurrent network for single channel speech enhancement." *arXiv preprint arXiv:2107.05429* (2021).
- [10] Marcu, David C., and Cristian Grava. "The impact of activation functions on training and performance of a deep neural network." *2021 16th International Conference on Engineering of Modern Electric Systems (EMES)*. IEEE, 2021.
- [11] Ye, Zhongfu, Nasir Saleem, and Hamza Ali. "Efficient gated convolutional recurrent neural networks for real-time speech enhancement." (2023).
- [12] Ketkar, Nikhil, et al. "Convolutional neural networks." *Deep Learning with Python: Learn Best Practices of Deep Learning Models with PyTorch* (2021): 197-242.
- [13] Hewamalage, Hansika, Christoph Bergmeir, and Kasun Bandara. "Recurrent neural networks for time series forecasting: Current status and future directions." *International Journal of Forecasting* 37.1 (2021): 388-427.
- [14] Wahab, Fazal E., et al. "Compact deep neural networks for real-time speech enhancement on resource-limited devices." *Speech Communication* 156 (2024): 103008.
- [15] Galvez, Daniel, et al. "The people's speech: A large-scale diverse english speech recognition dataset for commercial usage." *arXiv preprint arXiv:2111.09344* (2021).



**Hamza Ali** was born in Peshawar City, KPK, Pakistan in 1998. He received B.Sc. degree in Electrical engineering from the University of Engineering and Technology, Peshawar, Pakistan, in 2021. He is currently working toward the M.Sc. degree with University of Engineering and Technology, Mardan. His current research interests are broad areas of mobile networking, signal processing, and Machine learning.



**MUHAMMAD ISMAIL** holds a Bachelor's degree in Electrical Engineering from the University of Engineering and Technology, Peshawar (2021), and a Master's degree from the University of Engineering and Technology, Mardan (2023). He received the "Ihsaas Undergraduate Scholarship" and the "Stori da Pakhtunkhwa," awarded by the HEC Pakistan. His research interests encompass vehicular ad hoc networks, intelligent transportation systems, and machine learning (ML).



## REVIEW ARTICLE

# A Complementary Overview and Challenges in Radar Cross Section Modeling of Phased Array Antennas

\*<sup>1</sup>Ömer Burak Güngördü, <sup>1</sup>Ali Kara, and <sup>2</sup>Sinan Akşimşek

\*Gazi University, Faculty of Engineering, Electrical and Electronics Engineering, Ankara, Turkey  
omerburak.gungordu@gazi.edu.tr, Orcid.0009-0000-1272-4266

<sup>1</sup>Gazi University, Faculty of Engineering, Electrical and Electronics Engineering, Ankara, Turkey  
akara@gazi.edu.tr, Orcid.0000-0002-9739-7619

<sup>2</sup>ASELSAN, Ankara, Turkey  
haksimsek@aselsan.com, Orcid.0000-0002-0807-3824

**Citation:**

Güngördü, Ö. B., Kara, A. & Akşimşek, S. (2024). *A Complementary Overview and Challenges in Radar Cross Section Modeling of Phased Array Antennas*, Journal of Science Technology and Engineering Research, 5(1):86-91. DOI: 10.53525/jster.1493809

**HIGHLIGHTS**

- Review of RCS modelling methods of array antennas
- Challenges of RCS computations
- Current RCS reduction techniques

**Article Info**

Received : June 1, 2024

Accepted : June 19, 2024

**DOI:**

10.53525/jster.1493809

**\*Corresponding Author:**

Ömer Burak Güngördü  
omerburak.gungordu@gazi.edu.tr

Phone: +90 5443032625

**ABSTRACT**

*The radar cross-section (RCS) is a critical factor in the design and performance of modern airborne weapon systems. These systems utilize phased array antennas due to their low profile, advanced beamforming, and angle measurement capabilities. The effect of phased array antennas on platform RCS can be crucial. Addressing the RCS of phased array antennas involves solving both structural and antenna mode scattering. Each component presents different challenges for computation and requires specific RCS reduction techniques. This short review delves into various existing methods for computing antenna and structural mode RCS and offers insights into their application. Simulating the RCS of large array antennas presents significant challenges due to the high demands on computing resources. Additionally, this review highlights existing solutions aimed at reducing the simulation times and memory usage in RCS modeling while maintaining accurate results. However, further advancements are necessary to simulate large scale array antennas more efficiently and accurately.*

**Keywords:** Radar Cross Section, Phased Array, Structural Mode, Antenna Mode RCS, Stealth

## I. INTRODUCTION

Radar Cross-Section (RCS) is an important metric for modern airborne weapon systems that depend on its electromagnetic features. RCS is basically the measure of scattered power when an electromagnetic wave is incident on a target, and is a function of parameters such as orientation of target relative to radar transmitter and receiver, target geometry and material, wavelength of the incident wave, transmitter and receiver polarization, and many more [1].

Today, most stealth aircraft platforms and missile systems have systems that uses phased array antennas such as datalink systems, electronic warfare systems, fire control radar, etc. This preference is due to their low profile compared to other types of antennas and their ability to be installed conformally without disrupting the stealth geometry of the platform. Additionally, their abilities such as electronically steer beams and precise angle measurement makes them ideal for most aircraft systems. Therefore, when designing stealth platforms, it is crucial to analyze and reduce RCS of this type of antennas.

Phased array antennas have two forms of scattering: scattering due their structure and scattering due to their radiation characteristics. These two terms are defined as structural mode and antenna mode scattering respectively [1]. Structural mode scattering is measured when the antenna system is match loaded. Therefore, antenna mode scattering is neutralized and scattering occurs only due to the antenna's geometry, materials and aperture size. Over the years many techniques have been developed to reduce antenna RCS. One of the most investigated methods of reducing the structural mode RCS of antennas involves the integration of metasurfaces (MSs) to antenna. MS usage is appealing because they can be designed to control the amplitude, phase, and polarization of scattered waves. These features are leveraged to achieve scattered field cancellation, and therefore effectively reducing the RCS of the antenna. Some of the MS types used in the RCS reduction are artificial magnetic conductor (AMC) with perfect electric conductor (PEC) [2], FSS [3], or checkerboard polarization conversion metasurface (CPCM) [4]-[7], electromagnetic bandgap (EBG) structure [8], etc. However, implementing MSs introduces additional structural components to the antenna array, which can lead to decrease on bandwidth and gain of the antenna. Another method for reducing structural mode RCS is through the use of the reflection cancellation technique [9]-[11]. This approach involves using different antenna elements designed to produce reflections that are 180 degrees out of phase. By arranging and tuning these different antenna elements, the reflected waves interfere destructively, effectively canceling each other out and thus reducing the overall RCS. The technique depends on precise control of the phase and spatial configuration of the antenna elements to ensure destructive interference occurs effectively within the antenna frequency band. While this method offers effective reduction of structural mode RCS without the bandwidth limitations and it does not introduce any additional structures. It presents challenges such as design complexity, as designing an array with different antenna elements that exhibits similar radiation characteristics can be challenging. Additionally, it is reported that reduction of RCS is only effective under normal incidence, with different incident angles RCS reduction is less efficient [9].

Antenna mode scattering, on the other hand, occurs when antenna load is not matched. In this case, scattering from antenna is the summation of both structural and antenna mode scattering. For phased array antennas, analytically computing RCS is particularly challenging because of their complicated feed networks, mutual coupling between antenna elements, and other complications [1]. All these complications affect the radiation characteristics of the antenna and, therefore, antenna mode scattering component. Figure 1 shows a simplified scenario of antenna scattering where a single antenna element of an array is connected to various circuit elements.

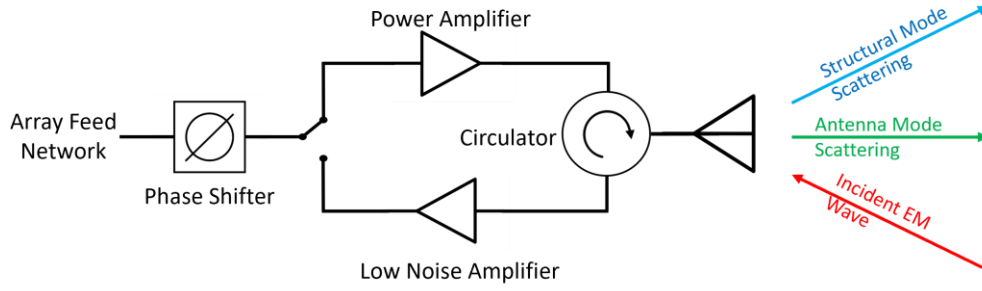


**Figure 1.** Scattering representation of phased array antenna

This study is organized as follows: Section II discusses the current analytical methods for computing antenna mode RCS, detailing their respective advantages and disadvantages. This section provides a comprehensive overview of techniques such as RCS with arbitrary loads, and gain-based reconstruction, among others. Section III addresses the challenges associated with computing the RCS of large phased array antennas. It also explores solutions to mitigate these challenges. Methods like GPU acceleration and the active element mode scattering pattern to enhance processing speeds and reduce memory requirements.

## II. BACKGROUND INFO

There are several methods to compute and/or simulate the RCS of antennas. Solving antenna RCS purely through analytical methods can be impractical due to the numerous assumptions required. Solving RCS with analytical methods is more complex for array antennas, which often feature complex feed networks with devices such as phase shifters and couplers. These components contribute to transmission loss of the array antennas. Solving the antenna mode RCS of array antennas solely through a full-wave electromagnetic (EM) simulator is not possible without additional post-processing steps. Full-wave EM simulators (e.g., HFSS, CST Microwave Studio) are necessary for modeling array antennas and providing data such as far-field patterns and S-parameters. Structural mode RCS can be computed directly through these simulators by terminating the antenna with matched loads, thus ensuring the simulation computes only passive scattering. Antenna mode RCS requires further post processing steps.

### A. Solving Antenna RCS with Arbitrary Loads

Antenna RCS can be expressed in terms of structural and antenna mode for an open circuited load as [12]

$$\sigma = |\sqrt{\sigma_s} + \sqrt{\sigma_{re}}e^{i\phi}|^2 \quad (1)$$

Where  $\sigma_s$  and  $\sigma_{re}$  are structural and antenna mode terms respectively,  $\phi$  is the phase difference between the terms. To solve the unknown phase difference between these terms a model was proposed at [13]. With this model antenna RCS is obtained with full wave simulator by simulating the antenna scattering with open and short circuit loads. Antenna RCS under any arbitrary load can be obtained with

$$\vec{E}^s(Z_1) = \frac{(1-\Gamma_a)\vec{E}^s(\infty)+(1+\Gamma_a)\vec{E}^s(0)}{2} + \frac{\Gamma_l}{1-\Gamma_l\Gamma_a} \frac{1-\Gamma_a^2}{2} [\vec{E}^s(\infty) - \vec{E}^s(0)] \quad (2)$$

$\vec{E}^s(\infty)$  and  $\vec{E}^s(0)$  is the scattered electric field when antenna load is terminated as open circuit and short circuit respectively.  $\Gamma_a$  and  $\Gamma_l$  represent the reflection coefficient of the antenna and the load, respectively. The first term of equation (2) corresponds to the structural mode scattering, while the second term corresponds to the antenna mode scattering field. Using this formulation, the scattered field of antenna RCS can be easily obtained with the aid of a full-wave simulator.

*B. Reconstructed Antenna Mode RCS Based on Antenna Gain*

Another method for solving antenna RCS is by using gain data of the antenna to reconstruct antenna scattering pattern. The relationship between antenna gain and antenna mode RCS has been long recognized. Appel-Hansen at [14] derives the relationship between antenna gain and antenna mode RCS for a hypothetical antenna for which all of the scattering is caused due to mismatch at the antenna load. If an antenna is terminated with a short circuit load there is a perfect reflection at the load [1] therefore total re-radiated power is equal to received power of the antenna.

Therefore, antenna mode RCS can be defined in terms of gain as;

$$\sigma_{re} = \frac{G^2 \lambda^2}{4\pi} \tag{3}$$

This definition only represents the antenna mode scattering portion and completely ignores the structural mode RCS, which occurs due to the physical properties of the antenna. But with this definition antenna mode scattering pattern can be reconstructed using the gain pattern obtained with a full wave simulator. Structural mode RCS portion can be obtained separately with full wave simulations when antenna is terminated with a matched load. In this way, scattering from the antenna is independent of the antenna feed and occurs solely because of the structure of the antenna.

The authors in [15] modifies this definition for array antennas to compute the antenna mode RCS using the scattering pattern multiplication method. Although this method ignores mutual coupling, edge effects, and feed losses, it allows for the estimation of array RCS with reduced simulation time compared to other methods. An improved alternative for this method has been proposed in [16] called the active element mode scattering pattern, which is similar to the active element pattern [17]. The antenna mode RCS is estimated by superposition of the antenna elements active element mode scattering pattern. Simulation time is further reduced by assuming that the inner array elements have similar patterns to the middle element. It is reported that compared with the reference method, proposed method requires 88% less memory usage, while maintaining low relative error.

*C. Antenna Mode RCS Calculation Through Directivity and Impedance of Each Array Segment*

In [18], the authors propose a novel method for analytically estimating the antenna mode RCS. A patch antenna array is divided into sections, directivity and impedance of each segment is computed using a full-wave simulator. These values are then incorporated into the formulation of the antenna mode RCS for N-element linear patch arrays. The scattered field contributions from each component of the array and its feed network are described using reflection and transmission coefficients in the formulation. This method can be useful for RCS computations of more conventional arrays with reduced simulation times.

A summary of the existing studies on RCS computation is presented in Table I. From the results, it is evident that there is a trade-off between simulation time and accuracy. Active Element Mode Scattering Pattern seems to offer the best middle ground for computing RCS of large arrays.

**TABLE I.** Summary of RCS Computation Methods

Method	Advantage(s)	Disadvantages(s)	Reference
<b>Antenna RCS with Arbitrary Loads</b>	Uses full-wave simulator data for accurate RCS results under various loads	Requires computationally intensive simulations with different loads	[13]
<b>Gain-Based Reconstruction</b>	Simplifies antenna mode RCS calculation using the gain data obtained with a simulator	Ignores structural mode RCS	[14]

<b>The Scattering Pattern Multiplication Method</b>	Reduces memory usage and simulation time	Edge and mutual coupling effects are not considered	[15]
<b>Active Element Mode Scattering Pattern</b>	Reduces memory usage and simulation time; edge and mutual coupling effects are considered	Assumes inner array element patterns are the same	[16]
<b>Directivity and Impedance Method</b>	Useful for conventional arrays; reduces simulation time	Requires detailed segment-by-segment analysis of arrays	[18]

### III. RESEARCH CHALLENGES AND DISCUSSION

Computing the RCS of large phased array antennas via full-wave simulators accurately can be very demanding on processing power and memory requirements. Detailed time-domain simulations can take a substantial amount of time. In order to increase processing speed, utilizing Graphical Processing Unit (GPU) acceleration can be very beneficial. Time-domain simulations heavily rely on the Central Processing Unit (CPU), resulting in memory bottlenecks and increased simulation times. The high memory bandwidth and parallel computing abilities of GPUs can significantly reduce simulation times compared to CPU computing alone.

New computational methods for simulating RCS of array antennas will likely focus on further optimizing existing methods to enhance time efficiency and accuracy. Hybrid methods that combine full-wave simulations with analytical approaches could be the key to more efficient and accurate RCS simulations.

### IV. CONCLUSION AND FUTURE DIRECTION

In this study, as part of an ongoing research on the RCS estimation of large array antennas, a literature review was conducted to analyze the current methods of computing antenna RCS. The review goes through existing techniques to discuss their respective advantages and disadvantages. Challenges in computing RCS of large arrays along with proposed solutions are also discussed. The necessity of GPU acceleration in full-wave simulations to improve processing speeds and reduce memory requirements is emphasized and its potential to significantly improve simulation times. Furthermore, methods like the active element mode scattering pattern provide time efficient solutions for estimating RCS with reduced simulation times and memory requirements. Making this method a good option for large-scale phased array RCS analysis. This study aims to find the optimal methods for estimating the RCS of phased arrays by discussing the existing methods.

Our current focus is to apply the aforementioned methods to estimate the RCS of large active electronically scanned array (AESA) type antennas and investigate potential RCS reduction techniques for these systems. Given the popularity of AESA antennas in modern stealth aircraft and missile systems, accurately determining and mitigating their RCS is crucial. We will utilize a combination of full-wave simulators and analytical methods to model the structural and antenna mode scattering.

### CONFLICTS OF INTEREST

They reported that there was no conflict of interest between the authors and their respective institutions.

### RESEARCH AND PUBLICATION ETHICS

In the studies carried out within the scope of this article, the rules of research and publication ethics were followed.

### REFERENCES

[1] Knott, E. F., Schaeffer, J. F., & Tulley, M. T. (2004). Radar cross section. SciTech Publishing.



- [2] Vasaneli, C., Bogelsack, F., & Waldschmidt, C. (2018). Reducing the radar cross section of microstrip arrays using AMC structures for the vehicle integration of automotive radars. *IEEE Transactions on Antennas and Propagation*, 66(3), 1456–1464. <https://doi.org/10.1109/tap.2018.2794410>
- [3] Noorbakhsh, B., Abdolali, A., & Janforooz, M. (2021). In-band radar cross-section reduction of the slot array antennas by RAM-based frequency selective surfaces. *IET Microwaves, Antennas & Propagation*, 15(5), 457–463. <https://doi.org/10.1049/mia2.12070>
- [4] Wang, X., Tong, X., Wang, J., A, S., Wang, J., & Han, X. (2024). A polarization-converting metasurface for reducing radar cross sections and enhancing radiation performance of circularly polarized array antennas. *Optics Communications*, 556, 130269. <https://doi.org/10.1016/j.optcom.2024.130269>.
- [5] Lu, Y., Su, J., Liu, J., Guo, Q., Yin, H., Li, Z., & Song, J. (2019). Ultrawideband monostatic and bistatic RCS reductions for both copolarization and cross polarization based on polarization conversion and destructive interference. *IEEE Transactions on Antennas and Propagation*, 67(7), 4936–4941. <https://doi.org/10.1109/tap.2019.2911185>.
- [6] Li, K., Liu, Y., Jia, Y., & Guo, Y. J. (2017). A circularly polarized High-Gain antenna with low RCS over a wideband using chessboard polarization conversion metasurfaces. *IEEE Transactions on Antennas and Propagation*, 65(8), 4288–4292. <https://doi.org/10.1109/tap.2017.2710231E>.
- [7] Ji, L., Hong, X., Yang, R., Liu, Q., & Zhang, W. (2024). A low radar cross section antenna array based on a liquid metal metasurface. *IET Microwaves, Antennas & Propagation*, 18(3), 173–180. <https://doi.org/10.1049/mia2.12452>
- [8] Chen, W., Balanis, C. A., & Birtcher, C. R. (2015). Checkerboard EBG surfaces for wideband radar cross section reduction. *IEEE Transactions on Antennas and Propagation*, 63(6), 2636–2645. <https://doi.org/10.1109/tap.2015.2414440>
- [9] Gou, Y., Chen, Y., & Yang, S. (2022). Radar cross section reduction of wideband Vivaldi antenna arrays with Array-Level scattering cancellation. *IEEE Transactions on Antennas and Propagation*, 70(8), 6740–6750. <https://doi.org/10.1109/tap.2022.3162082>
- [10] Zhao, C., Jiang, W., Ge, J., Xi, Y., Hong, T., & Gong, S. (2021). A low-radar cross section Vivaldi antenna array based on reflection cancelation. *International Journal of RF and Microwave Computer-aided Engineering*, 32(3). <https://doi.org/10.1002/mmce.23016>
- [11] Fang, S., Qu, S., Yang, S., & Hu, J. (2023). Low-Scattering X-Band Planar Phased Vivaldi Array antenna. *IEEE Transactions on Antennas and Propagation*, 71(3), 2808–2813. <https://doi.org/10.1109/tap.2023.3239137>
- [12] Ruck, G. T., Barrick, D. E., & Stuart, W. (2002). *Radar Cross Section Handbook*. Peninsula Publishing.
- [13] Liu, Y., Fu, D., & Gong, S. (2003). A Novel Model for Analyzing the Radar Cross Section of Microstrip Antenna. *Journal of Electromagnetic Waves and Applications*, 17(9), 1301–1310. <https://doi.org/10.1163/156939303322520043>
- [14] Appel-Hansen, J. (1979). Accurate determination of gain and radiation patterns by radar cross-section measurements. *IRE Transactions on Antennas and Propagation/I.R.E. Transactions on Antennas and Propagation*, 27(5), 640–646. <https://doi.org/10.1109/tap.1979.1142156>
- [15] Liu, Y., & You, L. (2011b). Research on the estimation and reduction measures of antenna mode RCS of airborne phased array. In 2011 4th IEEE International Symposium on Microwave, Antenna, Propagation and EMC Technologies for Wireless Communications. <https://doi.org/10.1109/mape.2011.6156207>.
- [16] J Gan, L., Jiang, W., Chen, Q., Li, X., Zhou, Z., & Gong, S. (2021). Method to estimate antenna mode Radar cross section of Large-Scale array antennas. *IEEE Transactions on Antennas and Propagation*, 69(10), 7029–7034. <https://doi.org/10.1109/tap.2021.3075536>
- [17] Pozar, D. (1994). The active element pattern. *IEEE Transactions on Antennas and Propagation*, 42(8), 1176–1178. <https://doi.org/10.1109/8.310010>
- [18] Singh, A., Sasidharan, D. K., & Singh, H. (2020). Analytical estimation of radiation mode radar cross section (RCS) of phased arrays. *IEEE Transactions on Vehicular Technology*, 69(6), 6415–6421. <https://doi.org/10.1109/tvt>.



## RESEARCH ARTICLE

# Fourier-Based Image Classification Using CNN

\*<sup>1</sup> Göktaş Erdem DAĞI, <sup>1</sup> Erhan GÖKÇAY, <sup>2</sup> Hakan TORA

\*Atılım University, Faculty of Engineering, Electrical and Electronics Engineering Department, Ankara, Türkiye  
[goktugdagi@gmail.com](mailto:goktugdagi@gmail.com), [Orcid.0000-0001-5723-4578](https://orcid.org/0000-0001-5723-4578)

<sup>1</sup>Atılım University, Faculty of Engineering, Software Engineering Department, Ankara, Türkiye  
[erhan.gokcay@atilim.edu.tr](mailto:erhan.gokcay@atilim.edu.tr), [Orcid.0000-0002-4220-199X](https://orcid.org/0000-0002-4220-199X)

<sup>2</sup>Biruni University, Faculty of Engineering and Natural Sciences, Electrical and Electronics Engineering Department, Istanbul, Türkiye  
[tora@biruni.edu.tr](mailto:tora@biruni.edu.tr), [Orcid.0000-0002-0427-483X](https://orcid.org/0000-0002-0427-483X)

**Citation:**

Dağı, G.E., Gökçay, E., Tora H., (2024), Fourier-Based Image Classification Using CNN, *Journal of Science, Technology and Engineering Research*, 5(1):92-101. DOI: 10.53525/jster.1501920

**HIGHLIGHTS**

- *Processing of images in the frequency domain using CNN algorithm*
- *The available data is transformed into the frequency domain and fed to the CNN model.*
- *The proposed CNN model is trained by the spatial convolution.*
- *The high and low frequency components of the data introduces more useful properties than its raw pixels.*

**Article Info**

Received : June 15, 2024

Accepted : June 20, 2024

**DOI:**

10.53525/jster.1501920

**\*Corresponding Author:**

Göktaş Erdem DAĞI,  
[goktugdagi@gmail.com](mailto:goktugdagi@gmail.com)

**ABSTRACT**

Recently, Convolutional Neural Networks (CNNs) have achieved remarkable success in computer vision, image processing and image processing tasks. Traditional CNN models work directly with spatial domain images. On the other hand, images obtained with Fast Fourier Transform (FFT) represent the Frequency domain and provide an advantage in computational cost by reducing potential calculation complexity. This study uses FFT converted images as input to the CNN algorithm to increase image classification and recognition accuracy and investigates the effects of this. The study begins with a comprehensive review of the foundations and features of FFT. It assumes that by converting the input images from the Spatial domain to the Frequency domain, the input image can be learned more efficiently and better results can be achieved in terms of performance by studying the most important features in the Frequency domain. To evaluate the effectiveness of this assumption, CIFAR-10, MNIST-Digits and MNIST-Fashion datasets were used. As a result, it has been shown that FFT-based preprocessing can improve classification accuracy, especially in cases where the datasets contain high-frequency noise, and it has shown different results in different datasets. Therefore, it is thought that the effect of FFT preprocessing varies depending on the datasets.

**Keywords:** *Machine Learning, Image Classification, Frequency Domain, Deep Learning*

## I. INTRODUCTION

Artificial intelligence (AI) has rapidly developed in recent years and has made a significant impact in many industrial and academic fields. AI refers to the simulation of human intelligence and behavior in machines that are programmed to think and mimic human actions [1]. Advances in image processing and analysis have particularly highlighted the power and potential of AI [2]. Extracting meaningful information from image data has found applications in medicine, security, the automotive industry, retail, and many other fields [3]. These machines are designed to perform tasks that typically require human intelligence, such as visual perception, speech recognition, decision-making, and language translation [4]. In this context, the use of AI techniques, especially deep learning models like Convolutional Neural Networks (CNNs), has brought revolutionary advancements in the field of image processing [5]. AI systems can analyze vast amounts of data, recognize patterns, and make predictions or decisions based on this data [6]. Today, AI is one of the fastest-growing and most exciting fields in computer science [7]. AI aims to simulate human-like intelligence and behavior using computers, and it strives to achieve this goal through a series of algorithms and techniques [8]. One of the most important of these techniques includes artificial neural networks, a subfield known as deep learning [9]. Deep learning is achieved through the use of complex artificial neural networks trained on large amounts of data [10]. These networks simulate the process of learning from data and discovering complex patterns, similar to the way the human brain works [11]. One of the most effective and widely used types of deep learning models is known as Convolutional Neural Networks (CNNs) [3]. CNNs are a type of artificial neural network that excels particularly when working with image data [4]. Image processing can be defined as the area that allows a computer to interpret, understand, and process an image [5]. Image processing techniques are widely used in various fields such as object recognition, face recognition, medical imaging, autonomous vehicles, and security systems [6]. When combined with AI techniques, image processing becomes more complex and effective [7]. In this context, deep learning models such as CNNs show superior performance in various tasks in the field of image processing [8]. These advancements in image processing, particularly in overcoming the limitations of traditional pixel-based methods and developing new approaches for performing more complex tasks, have been significant.

There have been many techniques existing in the literature for image classification employing various CNN models. Akwaboah's study involved developing and training three different CNN models in the spatial domain to classify CIFAR-10 images. These models varied in their convolutional filter sizes, pooling layers, and the use of dropout regularization [12]. They achieved a test accuracy of 72.81%, 67.07, and 75.43 for the model 1, model2, and model3, respectively. Adeyinka's research focused on optimizing CIFAR-10 classification by testing various CNN models with different depths and configurations. Advanced architectures like ResNet and DenseNet were utilized, achieving test accuracies exceeding 90%. These models leverage deeper layers and skip connections, significantly enhancing model generalization and robustness [13]. Hengyue Pan proposed a novel approach by training a CNN model, named CEMNet, in the frequency domain. The approach simplifies the convolution operation, making it easier to parallelize by replacing it with element-wise multiplication [14]. CEMNet introduced several enhancements, including a weight fixation mechanism to mitigate overfitting, and adaptations of batch normalization, Leaky ReLU, and dropout layers for the frequency domain. Experimental results demonstrated that CEMNet could achieve over 70% accuracy on the CIFAR-10 dataset [14]. Classification was performed using two types of images: RGB images and Fourier-transformed images. Sophie Tötterström achieved an accuracy of 79.23% for RGB images and 38.78% for frequency domain images on the CIFAR-10 dataset [15]. In another study, learnable frequency filters using Fourier transformation were developed for image classification problems. The main outlines of the study are as follows: Development of Frequency Filters, Cropping Procedure, and Weight Sharing. The developed learnable frequency filters achieved successful results in various computer vision problems. In summary, this study highlighted the significant contributions of frequency-domain approaches and learnable frequency filters in image classification problems. The developed methods demonstrated high performance in various application areas, making an important contribution to the literature [16].

This work presents a new approach that utilizes the frequency domain representation of the data to be classified in a CNN model. Instead of using frequency domain layers in the model, the available data is transformed to the frequency domain. In other words, we propose a convolutional network whose input is represented in the frequency domain. However, the model is trained by performing the spatial convolution.

The paper is organized as follows. In section 2, we describe the proposed approach and the data used for classifying the images. The experimental results and performance of the proposed method are introduced in section 3. Section 4 presents the conclusion.

## II. MATERIAL AND METHOD

In this study, artificial neural networks (ANNs) inspired by the structure and function of the human brain were utilized. Artificial neural networks consist of interconnected nodes called neurons, which are organized in layers. Each neuron receives specific inputs, performs computations, and transmits its output to other neurons in the network. Artificial neural networks are trained using the backpropagation method. This method involves adjusting the internal parameters of the network (weights and biases) based on the error between the model's predictions and the actual target values. This iterative learning process enables neural networks to learn complex patterns and relationships in the data, making them effective for tasks such as classification, regression, and pattern recognition.

In this study, Convolutional Neural Networks (CNNs), a type of deep learning network particularly used for the analysis of visual data, were employed. CNNs are highly effective in tasks such as image recognition and classification. They automatically and adaptively learn spatial hierarchies from the input data.

### Convolutional Neural Networks (CNN) Model

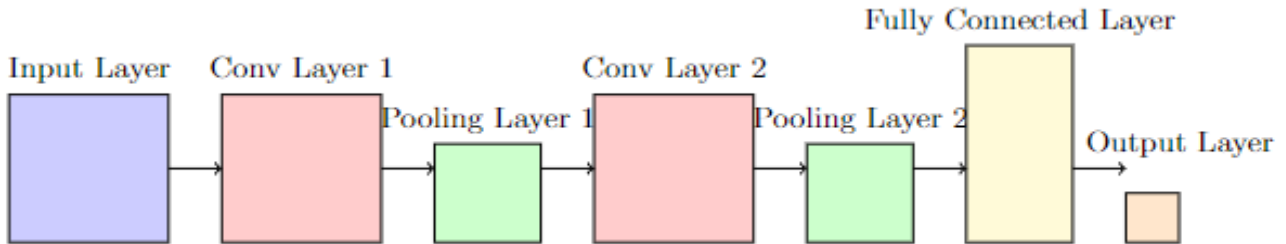


**Figure 1:** A simple representation of a Convolutional Neural Network(CNN) architecture.

The architecture of the CNN model consists of the following components:

- **Input Layer:** In CNNs, the input data typically consist of images or image-like datasets. This data is fed into the first layer of the CNN as matrices or tensors. For example, in RGB images, each pixel has three color channels: red, green, and blue. The input data are represented as matrices with pixel values ranging from 0 to 255.
- **Convolutional Layers:** Convolutional layers apply specific filters (kernels) to the input data to create feature maps. Filters are small matrices used to identify specific patterns or features. The convolution operation is performed by sliding these filters over the input data and calculating the dot product at each position to generate feature maps.
- **Activation Functions:** The outputs of the convolutional layers are usually subjected to a nonlinear activation function. The most commonly used activation function is the ReLU (Rectified Linear Unit) function. ReLU sets negative inputs to zero while keeping positive inputs unchanged, accelerating the learning process and reducing the vanishing gradient problem.
- **Pooling Layers:** Pooling layers are used to reduce the dimensions of the feature maps obtained from the

convolutional layers. This reduces the computational load of the model and mitigates the risk of overfitting. The most commonly used pooling type is max pooling, which selects the highest value in each region, thereby reducing the size of the feature map.

- **Fully Connected Layers:** These layers use the high-level features obtained from the convolutional and pooling layers to perform tasks such as classification or regression. The inputs are flattened and fed into fully connected layers, which use specific weights and biases to produce the final outputs.
- **Output Layer:** This layer produces the final predictions of the model. In classification tasks, the softmax activation function is used to obtain a probability distribution for each class.

## CNN Training

The aim of this study was to investigate whether the image can be used by taking the Fourier Transform of the input images for image classification with convolutional neural networks. Models were created for both RGB images and Fourier spectra. Models trained and evaluated with RGB images were then compared with models trained via Fourier Transform. Additionally, various applications were made on the image while adjusting the data set. Datasets utilized include CIFAR-10, MNIST Fashion, and MNIST Digit. The CIFAR-10 dataset comprises 60,000 images distributed across 10 classes, with images sized at 32x32x3, denoting RGB color channels. Conversely, both MNIST Fashion and MNIST Digit datasets encompass 60,000 grayscale images at a size of 28x28. In the CNN model, preprocessing steps were meticulously applied to each 32x32x3 (RGB) image in the CIFAR-10 dataset with the aim of optimizing processing load and enhancing feature extraction capabilities.

Initially, the dataset was organized as a 70% training set, a 20% test set, and a 10% validation set. Then RGB images underwent a grayscale conversion, reducing them to a manageable 32x32 size to facilitate subsequent processing steps. Following this, each 32x32 image was divided into smaller 2x2 subimages. This subdivision process occurred across the entire row, with a stride value of 1, traversing from the zeroth index to the last index. Upon reaching the end of a row, the process was repeated in the subsequent row. This iterative process was performed across all rows and columns, resulting in a 50 percent overlap due to the stride value of 1. The purpose of this overlapping was to investigate potential correlations between adjacent data points shown in Figure 2.a. Additionally, 2x2 subimages were extracted again, this time with a shift process that left a gap between indexes to prevent overlap shown in Figure 2.b. Padding was applied throughout these operations to prevent loss of information at the leading and trailing indexes. This meticulous approach aimed to capture intricate details and patterns present in the images. Subsequently, a new dataset was generated by subjecting each of these small subimages to the Fourier Transform. This transformation enabled the extraction of frequency-based features from the images. Upon completion of the Fourier Transform, the dimensions of the new dataset were determined. To mitigate potential scaling issues, the data underwent scaling by applying the logarithm to each image. Following these preprocessing steps, the small 2x2 subimages were reassembled to restore them to their original 32x32 dimensions shown in Figure 3. This reconstruction process ensured that the fundamental features extracted from the images remained intact. These comprehensive preprocessing steps played a pivotal role in enhancing the model's capability to extract meaningful features from the CIFAR-10 dataset, thereby contributing to the overall improvement in the classification performance of the CNN model. Furthermore, all operations except grayscale conversion were applied to the MNIST-Digits and MNIST-Fashion datasets, ensuring consistency in preprocessing across different datasets.



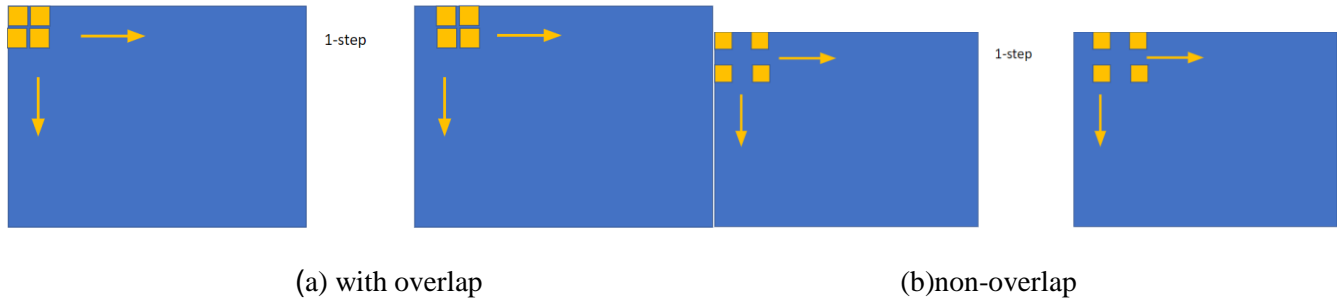


**Figure 2:** (a) refers to the overlapping image and (b) refers to the non-overlapping image.

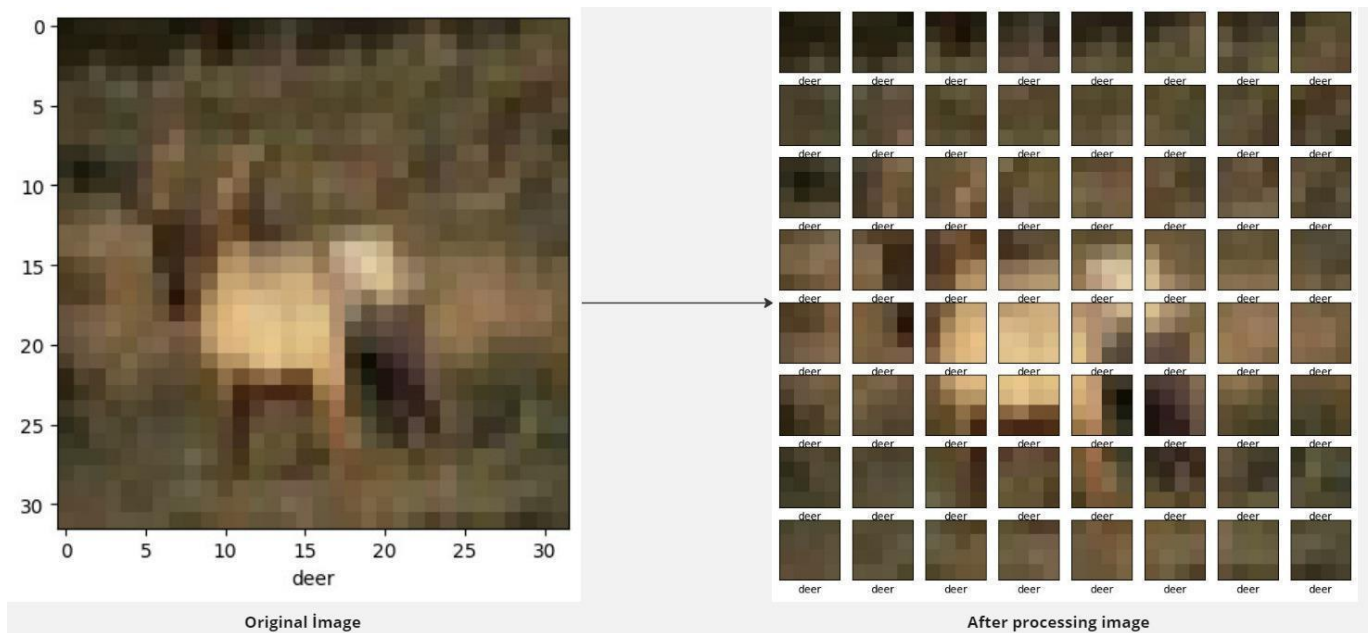


**Figure 3:** Original image and after processing.

### Proposed Model

In this study, the CNN algorithm is used for image classification. The proposed model is illustrated in Figure 4. The algorithm consists of 4 layers. The kernel size is set to 3x3, "same" padding is applied, and "ReLU" activation function is used. Additionally, BatchNormalization, Dropout, and MaxPooling are employed. In the fully connected layer, the "softmax function" is used as the activation function. "Sparse categorical crossentropy" is utilized as the loss function, and "Adam" is chosen as the optimizer.



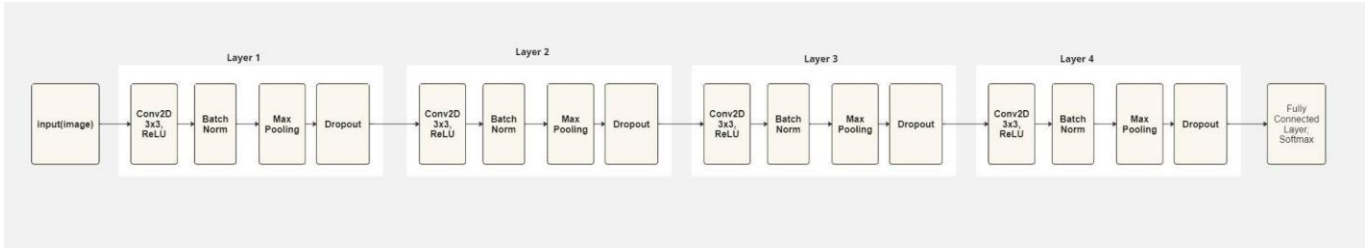


**Figure 4:** Proposed Model

**Application of the Basic Model and Training Process**

Following the application of the basic model, a classification model specific to the application studied was developed based on the same basic model. In this context, four different models were trained for the CIFAR-10, MNIST-Digits, and MNIST-Fashion datasets. For the CIFAR-10 dataset, one of the trained models performed the sliding operation with a standard stride value of 1, while the other models performed the sliding operation with 50% and 0% overlap, respectively. The same processes were repeated for the MNIST-Digits and MNIST-Fashion datasets. The trained models will provide benchmark results for the experiments conducted. Figures 5, 6, and 7 show the Training and Validation Accuracy values and Training and Validation Loss values for the CNN model throughout the training process on the CIFAR-10, MNIST-Digits, and MNIST-Fashion datasets. These figures indicate that both Training and Validation Loss values decreased, suggesting that the model effectively learned the data.

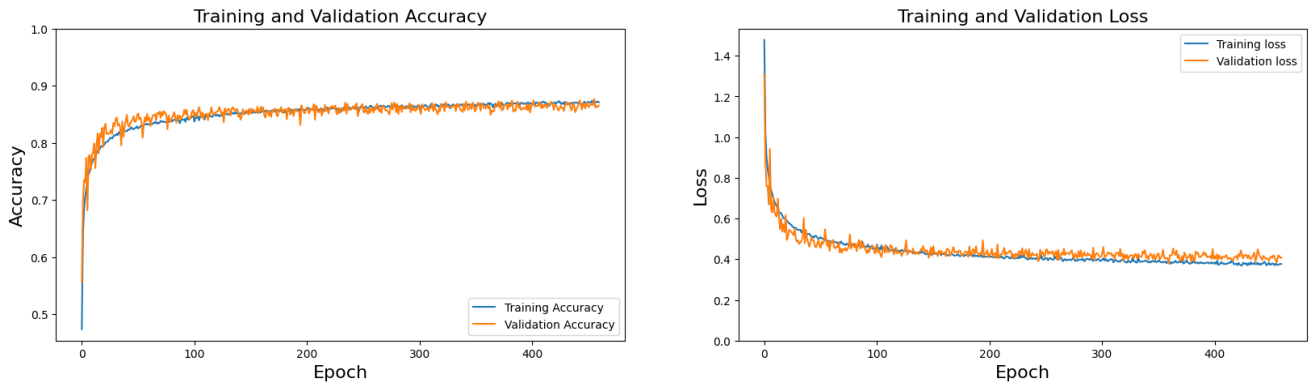


**Figure 5:** Training and Validation results for CIFAR-10 dataset

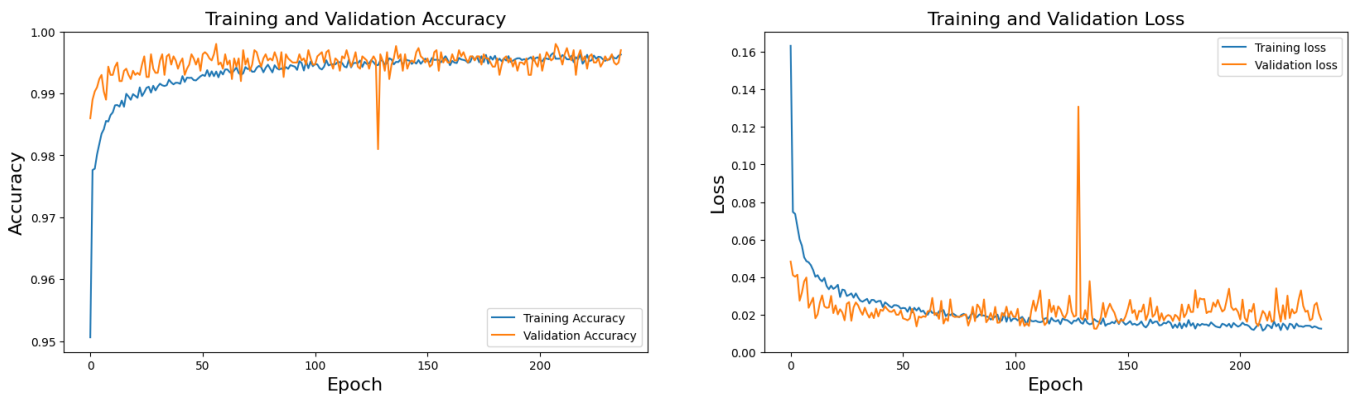


**Figure 6:** Training and Validation results for MNIST-Digits dataset

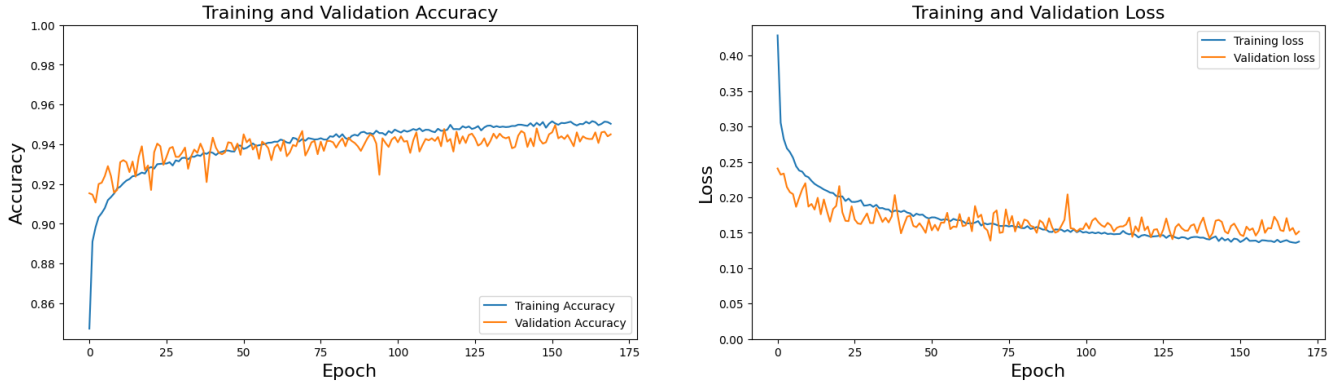


**Figure 7:** Training and Validation results for MNIST-Fashion dataset

Figures 8, 9, and 10 present the results of the Fourier Transform. These figures also show that, despite some occasional spikes, both Training and Validation Loss values generally decreased. Similarly, the Training and Validation Accuracy values were observed to increase. These findings demonstrate that the model effectively learned.

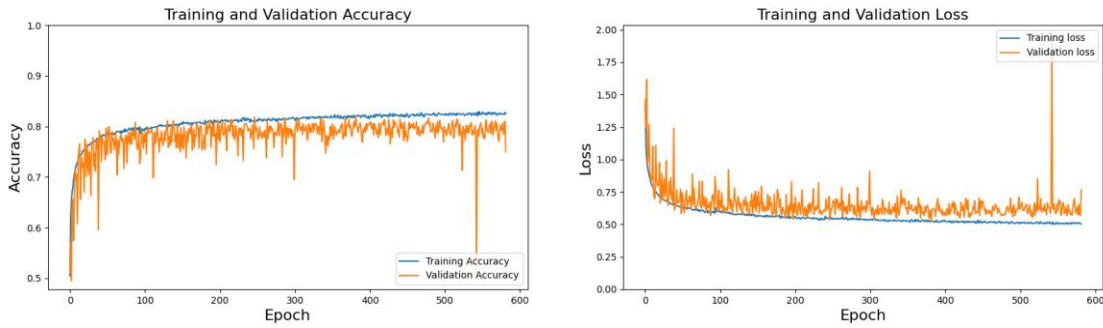


**Figure 8 :** Fourier Transform results for CIFAR-10 dataset

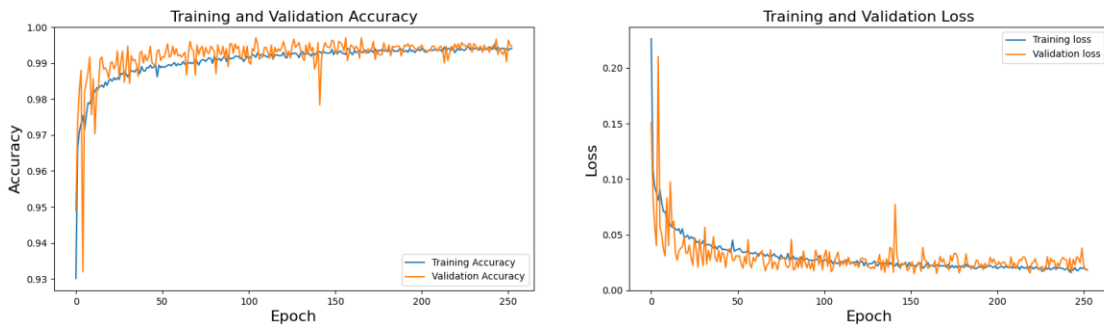


**Figure 9 :** Fourier Transform results for MNIST-Digits dataset

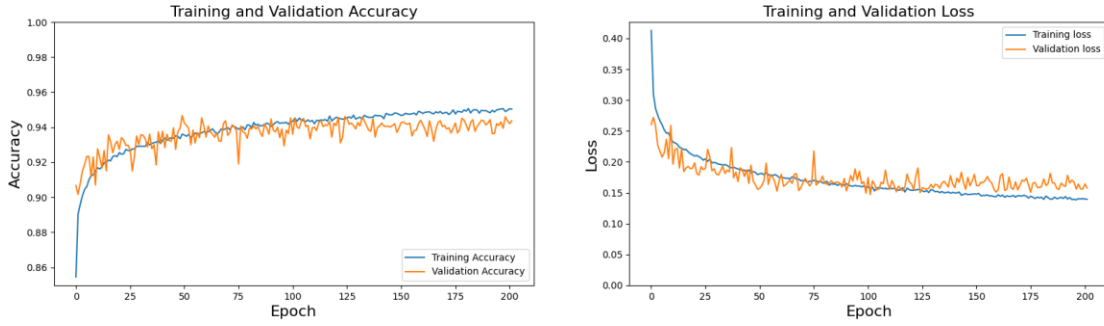


**Figure 10 :** Fourier Transform results for MNIST-Fashion dataset

### III. RESULTS AND ANALYSIS

This study is designed to examine the effectiveness of CNN models in image classification in the frequency domain. Model architectures and training processes were evaluated on various datasets such as CIFAR-10, MNIST-Digits, and MNIST-Fashion. The loss values used during training indicate how reliably the model adapts to the data. The loss values obtained during training in Figures 5, 6, and 7 demonstrate that the selected model adapts more reliably to the data. However, this reliability does not reflect in the classification results on the test data. The accuracy values in Table 1 indicate that the model’s ability to classify test data is weaker than the model discussed in the study. CNNs were observed to be more suitable for image classification in the time domain. This model architecture achieved better performance in image classification in the time domain. It was observed that CNNs were more suitable for image classification in the time domain. The results obtained from classifying input images obtained through Fourier transformation did not outperform those obtained in the time domain classification. However, it was observed that the proposed model was more successful compared to the operations performed on the entire image. The observed results are given in Table 1. This indicates that Fourier transformation may lead to information loss in some cases and adversely affect classification performance. In conclusion, this study evaluated the effectiveness of CNN models in image classification in the time domain. The results demonstrate that image classification in the time domain is more successful compared to frequency domain approaches such as Fourier transformation. However, more comprehensive studies on different datasets and model architectures will contribute to a deeper understanding of these results.

**Table 1 :** Accuracy values for different datasets and domains

Dataset	Spatial Domain	Frequency Domain without subimages	Frequency Domain with subimages
CIFAR-10	0.8593	0.4771	0.7865
MNIST-Digits	0.9946	0.9418	0.9326
MNIST-Fashion	0.9341	0.8362	0.8752

### IV. CONCLUSION

This paper explored the effectiveness of utilizing Fast Fourier Transform (FFT)-transformed images as inputs for Convolutional Neural Networks (CNNs) in image classification tasks. Various CNN architectures and training methodologies were assessed using benchmark datasets, including CIFAR-10, MNIST-Digits, and MNIST-Fashion. Training loss values, as depicted in Figures 6, 7, and 8, showed that the models adapted well to the data. However,

this adaptation did not necessarily result in improved classification accuracy on the test data, as evidenced by the accuracy values presented in Table 1. The research revealed that CNNs performed more effectively in the spatial (time) domain compared to the frequency domain. However, performing operations as in the proposed model instead of all images in the frequency domain gave better results. Models trained on spatial domain images consistently achieved better results than those trained on FFT-transformed images. This suggests that information necessary for accurate classification may be lost during the Fourier transform, negatively affecting the performance of the model. Although the frequency domain approach offered some valuable insights into data representation, it did not surpass the traditional spatial domain approach in terms of results. This underscores the robustness of spatial domain data for CNN-based image classification tasks. The observed performance gap between the two domains indicates that further refinement and the development of hybrid approaches might be required to fully harness frequency domain information. In conclusion, this study demonstrates that image classification with CNNs is more successful in the spatial domain than in the frequency domain. While FFT provides an alternative perspective on image data, it may introduce challenges that can hinder classification performance. Future research should focus on developing hybrid models that incorporate both spatial and frequency domain information, as well as examining the effects of FFT on a broader range of datasets and more advanced CNN architectures. Such efforts will enhance our understanding of the strengths and limitations of frequency domain analysis in deep learning. The findings of this work contribute to the field of computer vision by providing insights into the use of frequency domain techniques in CNN workflows. Future studies are encouraged to validate these findings and explore innovative methodologies to improve image classification performance by effectively combining spatial and frequency domain data.

#### CONFLICTS OF INTEREST

They reported that there was no conflict of interest between the authors and their respective institutions.

#### RESEARCH AND PUBLICATION ETHICS

In the studies carried out within the scope of this article, the rules of research and publication ethics were followed.

#### REFERENCES

- [1] S. Russell and P. Norvig, "Artificial Intelligence: A Modern Approach," 3rd ed., Prentice Hall, Upper Saddle River, NJ, USA, 2020.
- [2] I. Goodfellow, Y. Bengio, and A. Courville, "Deep Learning," MIT Press, Cambridge, MA, USA, 2016.
- [3] A. Krizhevsky, I. Sutskever, and G. E. Hinton, "ImageNet Classification with Deep Convolutional Neural Networks," in *Advances in Neural Information Processing Systems 25*, 2012, pp. 1097-1105.
- [4] K. He, X. Zhang, S. Ren, and J. Sun, "Deep Residual Learning for Image Recognition," in *Proc. IEEE Conf. Computer Vision and Pattern Recognition*, 2015, pp. 770-778.
- [5] C. Szegedy et al., "Going Deeper with Convolutions," in *Proc. IEEE Conf. Computer Vision and Pattern Recognition*, 2015, pp. 1-9.
- [6] K. Simonyan and A. Zisserman, "Very Deep Convolutional Networks for Large-Scale Image Recognition," in *Proc. Int. Conf. Learning Representations*, 2014.
- [7] V. Mnih et al., "Playing Atari with Deep Reinforcement Learning," in *Advances in Neural Information Processing Systems 27*, 2013, pp. 1-9.
- [8] J. Devlin, M.-W. Chang, K. Lee, and K. Toutanova, "BERT: Pre-training of Deep Bidirectional Transformers for Language Understanding," in *Proc. NAACL-HLT*, 2018, pp. 4171-4186.
- [9] I. Goodfellow et al., "Generative Adversarial Nets," in *Advances in Neural Information Processing Systems 27*, 2014, pp. 2672-2680.
- [10] A. Vaswani et al., "Attention is All You Need," in *Advances in Neural Information Processing Systems 30*, 2017, pp. 5998-6008.
- [11] R. Girshick, J. Donahue, T. Darrell, and J. Malik, "R-CNN: Regions with Convolutional Neural Network Features," in *Proc. IEEE Conf. Computer Vision and Pattern Recognition*, 2013, pp. 580-587.
- [12] Akwasi Darkwah Akwaboah, "Implementation of Convolutional Neural Networks for CIFAR-10 Image Classification," 2019.

- [13] Ajala Sunday Adeyinka, "Convolutional Neural Network Implementation for Classification using CIFAR-10," *ResearchGate*, 2023.
- [14] Hengyue Pan, "Learning Convolutional Neural Networks in Frequency Domain," *ResearchGate*, 2023.
- [15] S. Tötterström, "Frequency Domain Image Classification with Convolutional Neural Networks," *Bachelor's Thesis, Tampere University*, 2023.
- [16] Stuchi, J. A., Canto, N. G., de Faissol Attux, R. R., & Boccato, L. (2024). A frequency-domain approach with learnable filters for image classification. *Applied Soft Computing*, 155, 111443.